

# The Complex Multi-Wavelength Morphology of the Peculiar Compact Galaxy Group IC 2431

BEVERLY J. SMITH,<sup>1</sup> ROBERTO SORIA,<sup>2,3</sup> DOUGLAS SWARTZ,<sup>4</sup> MARK L. GIROUX,<sup>1</sup> CURTIS STRUCK,<sup>5</sup> AND RYAN URQUHART<sup>6</sup>

<sup>1</sup>*East Tennessee State University  
Department of Physics and Astronomy, Box 70652  
Johnson City TN 37614, USA*

<sup>2</sup>*INAF-Osservatorio Astrofisico di Torino  
Strada Osservatorio 20, I-10025 Pino Torinese, Italy*

<sup>3</sup>*Sydney Institute for Astronomy,  
School of Physics A28, The University of Sydney,  
Sydney NSW 2006, Australia*

<sup>4</sup>*Science and Technology Institute  
Universities Space Research Association,  
Huntsville, AL 35805, USA*

<sup>5</sup>*Iowa State University  
Department of Physics and Astronomy  
Ames IA 50011, USA*

<sup>6</sup>*Michigan State University  
Department of Physics and Astronomy  
East Lansing MI 48824, USA*

## ABSTRACT

We present new Chandra X-ray imaging spectroscopy of the compact galaxy group IC 2431, and compare with archival ultraviolet, optical, infrared, and radio images. IC 2431 is a starburst system containing three tidally-distorted disk galaxies. All three galaxies may have active nuclei. One galaxy is classified as an AGN based on its optical spectrum, a second is identified as a possible X-ray AGN based on the Chandra data, and the third galaxy may host a radio AGN. In optical images, a prominent dust lane crosses the southern galaxy, while Spitzer infrared images show a dusty bridge connecting the two brightest galaxies. Chandra maps reveal a massive ( $2 \times 10^7 M_\odot$ ) concentration of hot gas between these two galaxies, as well as several other knots of hot gas and non-thermal emission. The unabsorbed X-ray luminosity of the hot gas in IC 2431 is  $\sim 1 \times 10^{42} \text{ erg s}^{-1}$ , which is enhanced by about a factor of four relative to the star formation rate, compared to other star-forming galaxies. In radio maps, a bright jet/ridge of radio continuum emission extends 4 kpc from one nucleus. We compare the properties of IC 2431 with those of other interacting galaxy systems, and discuss two different scenarios that may account for the peculiarities of IC 2431: ram pressure stripping of the interstellar medium during a head-on collision between two galaxies, or an AGN-powered radio jet that has been distorted by an interaction with interstellar gas during a tidal encounter between galaxies.

## 1. INTRODUCTION

Galaxies in compact groups evolve quickly. Tidal distortions and galaxy mergers are frequent in the dense, low velocity-dispersion environment of a compact group (Mendes de Oliveira & Hickson 1994; Mendes de Oliveira et al. 1998; Gallagher et al. 2010; Torres-Flores et al. 2014), triggering bursts of star formation and then rapid quenching (Johnson et al. 2007; Gallagher et al. 2008; Tzanavaris et al. 2010; Walker et al. 2010; Plauchu-Frayn et al. 2012; Lenkić et al. 2016). Tidal stripping of cold interstellar gas is common in compact groups, producing HI deficiencies compared to field galaxies (Verdes-Montenegro et al. 2001; Jones et al. 2019, 2023). Groups that are HI deficient are more likely to be quenched (Walker et al. 2016). Increased interstellar gas turbulence due to shocks driven by

interactions and collisions between galaxies may further suppress star formation by inhibiting gravitational collapse of gas clouds (Alatalo et al. 2015; Lisenfeld et al. 2017). The detection of mid-infrared  $H_2$  emission from some compact groups (Cluver et al. 2010; Appleton et al. 2006; Cluver et al. 2013; Appleton et al. 2017) supports the idea that shock-heating contributes to quenching in compact groups. Morphological evolution also occurs quickly in compact groups (Coziol & Plauchu-Frayn 2007; Montaguth et al. 2023). Within a few billion years, a compact group of spirals may undergo a series of mergers to form an elliptical galaxy (Barnes 1989; Bode et al. 1993; Ponman et al. 1994; Jones et al. 2000). So-called ‘fossil groups’, groups containing a dominant elliptical two magnitudes brighter or more than the rest of the galaxies in the group, tend to have hot gas halos bright in the X-ray (Mulchaey & Zabludoff 1998; Jones et al. 2003).

Feedback from active galactic nuclei (AGN) may heat interstellar/intragroup gas in compact groups and further drive evolution (Eckert et al. 2021, 2024). Although compact group galaxies do not show an excess of optically-selected Seyfert nuclei (Kelm et al. 1998; Sohn et al. 2013; Tzanavaris et al. 2014, but see Kelm et al. 2004), the central dominant elliptical in fossil groups and other groups often host radio-loud AGN (Kraft et al. 2003; Hess et al. 2012; O’Sullivan et al. 2017, 2018; Kolokythas et al. 2018; Pasini et al. 2020). Outflows from radio AGN may disturb and heat the surrounding medium (Boehringer et al. 1993; McNamara et al. 2000; Finoguenov & Jones 2001; Kraft et al. 2003; Fabian et al. 2003; McNamara & Nulsen 2012; Kolokythas et al. 2020), potentially suppressing star formation (Croton et al. 2006; Dubois et al. 2010; Choi et al. 2015; Werner et al. 2019; Comerford et al. 2020; Nesvadba et al. 2021; Drevet Mulard et al. 2023; Ogle et al. 2024). AGN feedback is routinely included in cosmological simulations to reproduce the observed properties of galaxies (Croton et al. 2006; Bower et al. 2006; Choi et al. 2014; Weinberger et al. 2018; Bigwood et al. 2025).

Depending upon evolutionary stage and star formation rate (SFR), X-ray activity may be enhanced in compact groups compared to field galaxies (Bahcall et al. 1984; Desjardins et al. 2013; Fuse & Broming 2013; Tzanavaris et al. 2014, 2016; O’Sullivan et al. 2017). Starburst galaxies tend to have large quantities of hot X-ray-emitting gas (Strickland et al. 2004; Mineo et al. 2012a; Smith et al. 2018, 2019) as well as enhanced populations of high mass X-ray binaries (HMXBs) (Grimm et al. 2003; Mineo et al. 2012b) and ultra-luminous X-ray sources (ULXs) (Swartz et al. 2011; Smith et al. 2012). ULXs are extra-nuclear X-ray point sources with  $L_X > 10^{39}$  erg sec $^{-1}$  which may be HMXBs, intermediate mass black holes (IMBHs), or pulsars (Swartz et al. 2011; Bachetti et al. 2014; Kaaret et al. 2017; Walton et al. 2022). In addition, in compact groups the rapid passage of a galaxy through intragroup gas may lead to shock heating of the gas. The best-known example of an X-ray-bright intergalactic shock front in a compact group is that in Stephan’s Quintet (Pietsch et al. 1997; Sulentic et al. 2001; Trinchieri et al. 2003). In Stephan’s Quintet, a fast-moving intruder galaxy collided with tidal gas stripped out in earlier interactions (Renaud et al. 2010; Hwang et al. 2012), producing a 40 kpc-long shock front with an X-ray luminosity of about  $10^{41}$  erg s $^{-1}$  (Trinchieri et al. 2003). Strong mid-IR  $H_2$  lines confirm the presence of shocks in this region (Cluver et al. 2010; Appleton et al. 2006, 2017). The compact group NGC 4410 is another transitional system, with an extragalactic ridge of X-ray-emitting intragroup hot gas coincident with optical emission-line gas (Smith et al. 2003), an HI tail (Smith 2000), and a radio-loud AGN (Hummel et al. 1986; Smith 2000).

Shocks caused by direct face-on collisions between gas-rich disk galaxies can also produce large quantities of hot gas outside the main bodies of the galaxies. The best-studied example is the Taffy galaxies (UGC 12914/5), a pair of edge-on side-by-side disk galaxies connected by a bridge of radio continuum emission (Condon et al. 1993). This bridge produces  $5 \times 10^{39}$  erg $^{-1}$  in diffuse X-ray light (Appleton et al. 2015). The bridge is also detected in the mid-IR  $H_2$  lines (Peterson et al. 2012), and has optical spectral signatures of shocks (Joshi et al. 2019). Star formation may be suppressed in the bridge (Appleton et al. 2022), perhaps due to enhanced turbulence and shock heating (Yeager & Struck 2020; Vollmer et al. 2021; Yeager et al. 2024). Head-on collisions between disk galaxies may also happen within compact groups, for example, in the compact group HCG 57 (O’Sullivan et al. 2025). Shock heating during such collisions may contribute to the diffuse hot gas seen in compact groups, and may help suppress star formation.

In a survey of nine compact groups, seven were found to have hot diffuse X-ray emitting gas (Desjardins et al. 2013). The hot gas morphology appears to be correlated with interaction/merger stage, suggesting an evolutionary sequence. In early-stage systems, the hot gas is strictly located within the disks of the galaxies; in more evolved systems, hot gas is seen in tidal features, between the galaxies, or in a group halo. In the Desjardins et al. (2013) sample, the diffuse  $L_X$  from hot gas increases as specific star formation rate (sSFR) decreases, and the fraction of galaxies in the group that are elliptical or S0 increases as the ratio of atomic gas mass to dynamical mass decreases. In a set of 19 compact groups, Desjardins et al. (2014) found that  $L_X(\text{gas})$  is anti-correlated with the fraction of the baryons that

are in interstellar atomic hydrogen. These trends suggest that as a compact group ages and the spirals in the group evolve into early-type galaxies, cold gas gets used up in star formation and/or gets heated by shocks, AGN feedback, or other processes, producing an X-ray halo.

In this paper, we present new Chandra observations of the compact group of galaxies known as IC 2431, and compare with archival data at other wavelengths. IC 2431, also known as VV 645, UGC 04756, Mrk 1224, V1CG 340, IRAS 09018+1447, MLCG 776, and CGCG 090-063, was first reported in Javelle’s 1908 catalog of nebulae (Javelle 1908), and was occasionally investigated in surveys of highly star-forming galaxies (e.g., Markarian et al. 1979; Mazzarella & Balzano 1986; Saunders et al. 2000; Ashby et al. 2011; Mahajan et al. 2019; Kouroumpatzakis et al. 2021). However, it received little individual attention until it was ‘rediscovered’ a century after Javelle by the Galaxy Zoo project (Willett et al. 2013) and noted as one of the most dramatic and oddly-shaped merger systems in the Sloan survey (Keel et al. 2022). As discussed below, IC 2431 has some similarities to Stephan’s Quintet, NGC 4410, and the Taffy galaxies. Assuming a Hubble constant of  $72 \text{ km s}^{-1} \text{ Mpc}^{-1}$  and correcting for Virgocentric flow, IC 2431 is at a distance of 207 Mpc.

In Section 2 of this paper, we describe the available data, including archival optical, ultraviolet, infrared, and radio data, as well as the new Chandra X-ray data, and discuss the morphology of the system. A more detailed analysis of these data is provided in Section 3, where we investigate the X-ray spectra and use UV/optical/IR photometry to derive star formation rates (SFRs), stellar masses, stellar population ages, and dust extinctions for various portions of the system. In Section 4, we compare and contrast IC 2431 to other systems. The evolutionary state of IC 2431 is discussed in Section 5. A summary is provided in Section 6.

## 2. DATA

### 2.1. Optical Images and Spectra

IC 2431 was observed by the Advanced Camera for Surveys Wide Field Camera on the Hubble Space Telescope (HST) in the red F606W filter as part of a large HST snapshot survey (proposal ID 15445; Keel et al. 2022). We retrieved the processed HST image from the European HST Science Archive<sup>1</sup>. This image has a reported registration rms of 0.03 based on astrometric stars from the Gaia DR3 catalog<sup>2</sup> (Gaia Collaboration et al. 2016). This is consistent with our custom registration. In the left panel of Figure 1, we display this HST image.

In the Uppsala General Catalogue of Galaxies (UGC) (Nilson 1973), IC 2431 is listed as a quadruple system, and the NASA Extragalactic Database (NED) lists four components, IC 2431 NED01 – NED04. Inspection of the HST image and archival Dark Energy Survey (DES) Legacy grz images<sup>3</sup> (Dey et al. 2019) as well as near-IR images (Section 2.3), however, suggests that IC 2431 only contains three main galaxies, all disk galaxies. We label these galaxies A, B, and C, south to north, as shown in the left panel of Figure 1. Galaxy C is NED01 (SDSS J090434.55+143552.3), galaxy B is NED02, and galaxy A is NED03 and NED04 together.

The two main galaxies in IC 2431, Galaxy A and Galaxy B, appear to be two distorted disks both viewed approximately edge-on, and aligned face-to-face. The two galaxies are separated by about  $8''$  on the sky, which corresponds to 8 kpc at the distance of IC 2431. The probable reason that earlier studies counted more than three galaxies in this group is because of a prominent dust lane that bisects galaxy A. At low spatial resolution in blue images, galaxy A appears to be two galaxies. In the higher resolution HST image (left panel, Figure 1) and in color DES Legacy images (right panel, Figure 1), however, the dust lane is apparent, projected in front of Galaxy A. This dust lane may be a tidal extension of Galaxy C, a distorted spiral arm of Galaxy B projected in front of Galaxy A, or interstellar material pushed out of Galaxy B or Galaxy C by a head-on collision between galaxies. This dust absorption is discussed further in the analysis below.

At least five and maybe six tidal features are present in this system, labeled 1 – 6 in the right panel of Figure 1. These include: 1) a tidal tail extending from C to the northwest, 2) a tail extending from B to the northeast, 3) a curved tail bending to the southeast from the northern end of A, 4) a tidal tail extend to the southwest from the southern end of the disk of B. 5) another structure that runs parallel to feature 4, extending southwest from the southern end of disk A. Feature 5) may connect to disk A, or it may originate in disk B and cross disk A. 6) The dust lane that crosses disk A may be a sixth tidal feature, although that is uncertain.

<sup>1</sup> <https://hst.esac.esa.int>

<sup>2</sup> <https://gea.esac.esa.int/archive/>

<sup>3</sup> <https://www.legacysurvey.org/>



The heliocentric velocities of Galaxies A, B, and C, respectively, are  $14840 \pm 36 \text{ km s}^{-1}$ ,  $14926 \pm 39 \text{ km s}^{-1}$ , and  $14870 \pm 3 \text{ km s}^{-1}$  (Sohn et al. 2016), giving a radial velocity dispersion for the group of only  $31 \text{ km s}^{-1}$ . Given the prominent tidal features visible in this system, this small observed velocity dispersion suggests that most of the relative motion of the galaxies in the group are in the plane of the sky. Galaxy C is classified as an optical AGN by Lee et al. (2017). Galaxy B is classified as an H II region galaxy by Smith et al. (1998) based on optical spectroscopy. A rotation curve for Galaxy B was derived by Smith et al. (1996) from a long slit optical spectrum. This rotation curve rises steeply in the inner  $3''$  radius then flattens, with a total velocity width of  $434 \text{ km s}^{-1}$  and a derived dynamical mass of  $1.0 \times 10^{11} M_{\odot}$ .

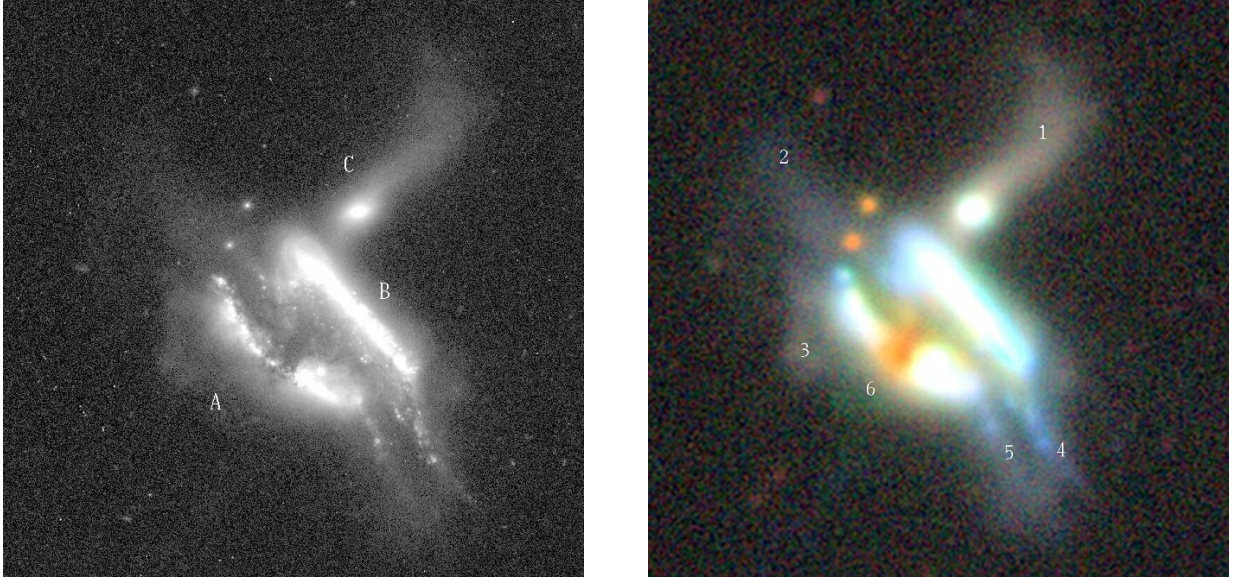


**Figure 1.** Left: the archival HST F606W image of the IC 2431 group. Galaxies A, B, and C are marked. The field of view is  $1'$ . North is up and east to the left. Right: The DES Legacy Survey RGB image of IC 2431. Note the prominent red band crossing galaxy A in the south. The superimposed numbers identify six tidal features in the system.

## 2.2. Atomic Hydrogen Gas

IC 2431 was detected in the 21 cm HI line as part of the ALFALFA Arecibo HI Survey (source AGC 190759) (Haynes et al. 2018). The IC 2431 group is unresolved with the Arecibo beam of  $3'.8 \times 3'.2$ . The HI centroid is offset about  $18''$  north of the group center, close to Galaxy C. The HI flux of  $0.57 \pm 0.07 \text{ Jy km s}^{-1}$  corresponds to an HI mass of  $6 \times 10^9 M_{\odot}$ . The HI heliocentric velocity is  $14,871 \text{ km s}^{-1}$  and the FWHM line width is  $124 \text{ km s}^{-1}$  (Haynes et al. 2018).

## 2.3. UV and IR Images

In Figure 2, we compare the optical HST image of IC 2431 with far-UV and near-UV images from the GALEX All-Sky Survey (Martin et al. 2005), near-infrared J, H, and K images from the 2MASS Atlas<sup>4</sup>, and archival Spitzer Infrared Array Camera (IRAC) (Fazio et al. 2004) images at  $3.6 \mu\text{m}$ ,  $4.5 \mu\text{m}$ ,  $5.8 \mu\text{m}$ , and  $8.0 \mu\text{m}$ . The GALEX FUV and NUV bands have approximate FWHM resolutions of  $4''.0$  and  $5''.6$ , respectively<sup>5</sup>, the effective resolution of 2MASS is about  $4''.0$  in the Atlas images<sup>6</sup>, and Spitzer provided effective resolution of  $1''.66$ ,  $1''.72$ ,  $1''.88$ , and  $1''.98$  at  $3.6$ ,  $4.5$ ,  $5.8$ , and  $8.0 \mu\text{m}$ , respectively<sup>7</sup>. We also utilize co-added images from the WISE Atlas<sup>8</sup> in the mid-infrared W1 ( $3.4 \mu\text{m}$ ), W2 ( $4.6 \mu\text{m}$ ), W3 ( $12 \mu\text{m}$ ), and W4 ( $22 \mu\text{m}$ ) filters. These WISE images have approximate FWHM point spread functions of  $8''.3$ ,  $9''.1$ ,  $9''.5$ , and  $16''.8$  in W1, W2, W3, and W4, respectively<sup>9</sup>, thus the galaxies are not well-resolved with WISE.

<sup>4</sup> <https://irsa.ipac.caltech.edu/data/2MASS/docs/releases/allsky/doc/expsup.html>

<sup>5</sup> <https://asd.gsfc.nasa.gov/archive/galex/Documents/MissionOverview.html>

<sup>6</sup> <https://www.ipac.caltech.edu/2mass/overview/about2mass.html>

<sup>7</sup> <https://irsa.ipac.caltech.edu/data/SPITZER/docs/irac/>

<sup>8</sup> <https://wise2.ipac.caltech.edu/docs/release/allsky/expsup/>

<sup>9</sup> <https://wise2.ipac.caltech.edu/docs/release/allsky/expsup/sec1.4c.html>

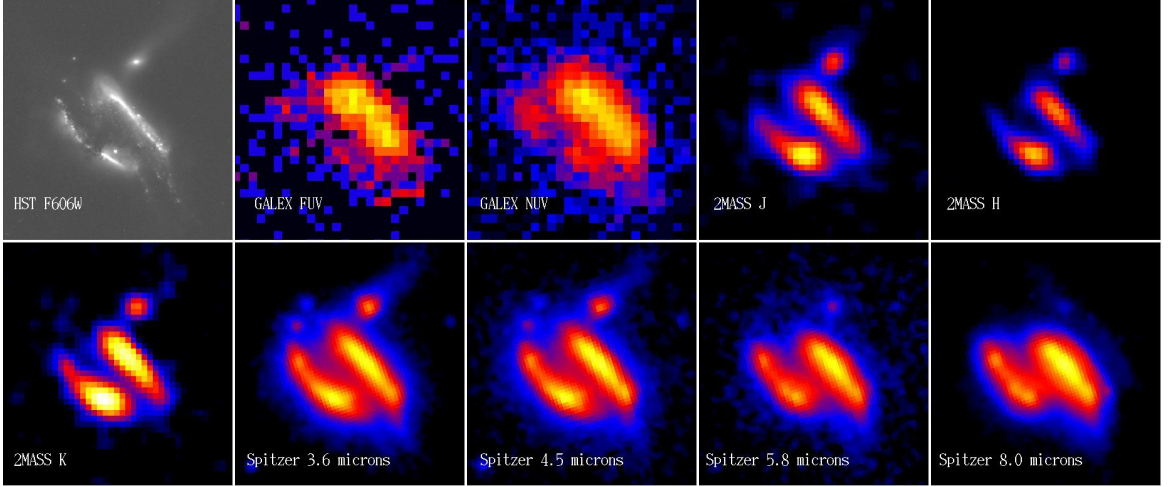


**Figure 2.** Images of IC 2431 at various wavelengths. From left to right, top to bottom: the images are: HST F606W, GALEX FUV, GALEX NUV, 2MASS J, 2MASS H, 2MASS K, Spitzer 3.6  $\mu\text{m}$ , Spitzer 4.5  $\mu\text{m}$ , Spitzer 5.8  $\mu\text{m}$ , and Spitzer 8.0  $\mu\text{m}$ . The field of view is  $0''.7$ , with north up and east to the left.

Figure 2 shows that Galaxy B contributes a large majority of the observed light in the two UV bands. In contrast, in the 2MASS NIR images, Galaxy A is comparable to Galaxy B in brightness. In the 2MASS images the southern portion of Galaxy A is considerably brighter than the northern portion. In the Spitzer 5.8  $\mu\text{m}$  and 8.0  $\mu\text{m}$  images, Galaxy B is clearly brighter than Galaxy A; the two galaxies are more comparable in the 3.6  $\mu\text{m}$  and 4.5  $\mu\text{m}$  images. In the Spitzer images, the relative brightness of Galaxy C decreases with increasing wavelength from 3.6  $\mu\text{m}$  to 8.0  $\mu\text{m}$ .

A zoomed-in comparison of the HST F606W image and the Spitzer 8  $\mu\text{m}$  image is provided in the top two rows of Figure 3. The top two left panels display the HST image, while the top two right panels show the Spitzer image. In the top row, contours from the HST image are superimposed, while in the second row, contours from the Spitzer 8  $\mu\text{m}$  image are overlaid. Galaxy A looks very thin in the red HST image, suggesting an edge-on disk without a large bulge component. The position of the mid-infrared maximum in Galaxy A is coincident within the uncertainties with the hard X-ray peak (see Section 2.4), which we assume is the galactic nucleus. The mid-infrared peak in Galaxy A lies just to the south of the dust lane. From this peak, a ridge of mid-IR emission extends along the disk of Galaxy A to the northeast, to a secondary peak about  $9''$  (9 kpc) away from the nucleus. This ridge of mid-IR emission in the north is slightly offset (about  $0''.6 = 0.6$  kpc) to the northwest of star forming regions visible in the optical. Along the ridge, the mid-IR light is particularly bright where the dust lane crosses the disk of Galaxy A, implying strong star formation in that region. Fainter diffuse 8.0  $\mu\text{m}$  emission is seen extending towards Galaxy B, starting at the location where the dust lane crosses Galaxy A. This morphology suggests a bridge of gas and dust connecting the two galaxies. This mid-IR bridge is especially apparent in the 8  $\mu\text{m}$  contours in Figure 3.

South of the mid-IR peak in Galaxy A, little mid-infrared emission is detected. The mid-IR/optical spatial offsets in Galaxy A and the apparent mid-infrared bridge between the two galaxies suggest star formation triggering caused by ram pressure stripping during a collision between two galactic disks. This possibility is discussed further in Section 5.

In Section 3.1 of this paper, we extract UV/optical/IR photometry from these images. In Sections 3.2 and 3.4, we use this photometry to derive SFRs, stellar masses, population ages, and extinctions for various regions within IC 2431.

#### 2.4. Chandra Observations and Images

A total of eight observations of IC 2431 were made with Chandra (Table 1). All of these data were obtained with the Advanced CCD Imaging Spectrometer (ACIS) S-array. In the following analysis, we only use the data from the S3 chip on ACIS, since IC 2431 was centered on S3 and the entire group of galaxies fits within the  $8'.3 \times 8'.3$  field of view of the ACIS-S3 chip. Basic data reduction was accomplished using the Chandra Interactive Analysis of Observations (CIAO) software. The data were reprocessed using the `chandra_repro` script, and the data were filtered to exclude



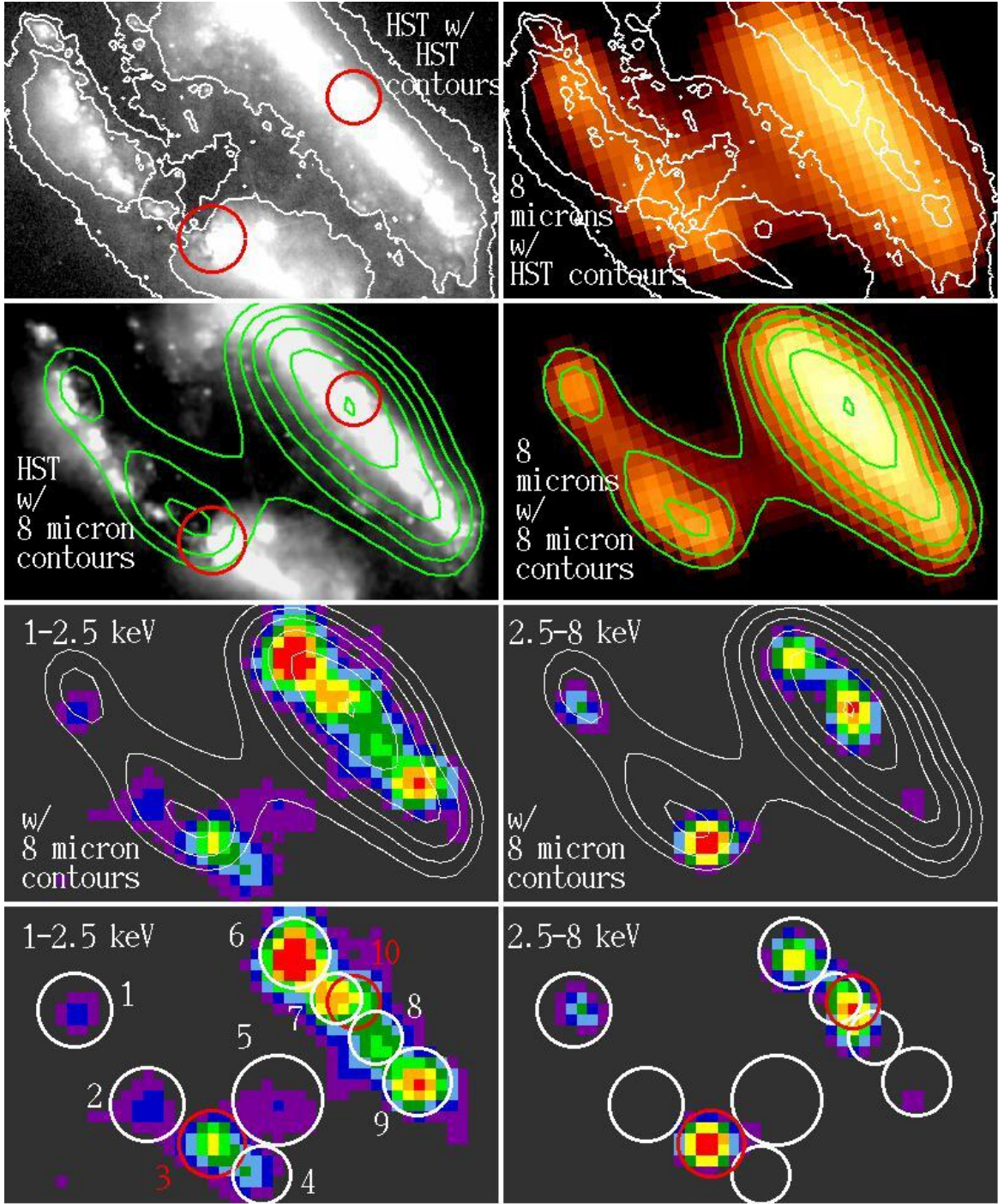


**Figure 3.** Zoomed-in views of Galaxy A and Galaxy B in various bands. The field of view is  $22''.2 \times 13''.3$ , with north up and east to the left. Top left: HST F606W image of IC 2431 with F606W contours of 4, 5, and  $20 \times 10^{-20} \text{ erg s}^{-1} \text{ cm}^{-2} \text{ \AA}^{-1}$  displayed. These contours were selected to outline the dust features and mark the optically-bright areas. The presumed galactic nuclei are marked in red. Top right: Spitzer  $8 \mu\text{m}$  image with HST contours overlaid. Second row left: HST image with contours showing Spitzer  $8 \mu\text{m}$  isophotes at levels of 20, 27, 36, 49, 69, 102, and  $155 \text{ MJy SR}^{-1}$ . Second row right: Spitzer  $8 \mu\text{m}$  map with  $8 \mu\text{m}$  contours. Third row left: medium energy ( $1.0 - 2.5 \text{ keV}$ ) Gaussian-smoothed Chandra map with Spitzer  $8 \mu\text{m}$  contours. Third row right: high energy ( $2.5 - 8 \text{ keV}$ ) Gaussian-smoothed Chandra map with Spitzer  $8 \mu\text{m}$  contours. Bottom left: the smoothed Chandra medium-energy map, with our ten targeted X-ray sources marked and labeled. The assumed galactic nuclei for Galaxy A and Galaxy B, sources #3 and #10, are circled and labeled in red. Bottom right: the smoothed Chandra high energy map with our targeted X-ray sources marked.

**Table 1.** Chandra Observations of IC 2431

Obs ID	Exposure (ksec)	Date
26932	11.92	2024-01-29
27202	11.85	2024-02-13
27203	15.46	2023-01-16
27673	15.73	2023-01-18
29230	11.92	2024-01-29
29231	18.29	2024-01-29
29273	10.93	2024-02-13
29274	9.70	2024-02-16

all but grades 0, 2, 3, 4, and 6. Background regions on the S3 chip were selected to exclude the IC 2431 system and bright background point sources. The data were searched for background flares using the CIAO routine `deflare` with the sigma clipping routine. Only one of the eight datasets showed flare activity, eliminating only 0.07 ksec of data. The final exposure times are provided in Table 1.

Point sources in the field were used to register each individual dataset using Gaia and Dark Energy Survey positions. For display purposes, after registration we combined the datasets using the CIAO routine `reproject_obs`. After Gaussian smoothing using the `ds9` software<sup>10</sup>, the X-ray images are shown in the bottom two rows of Figure 3. The left panels give the medium energy map (1.0 – 2.5 keV), while the right panels display the high energy map (2.5 – 8 keV). Contours from the Spitzer 8  $\mu\text{m}$  image are overlaid on the X-ray maps in the second-to-the-bottom row of Figure 3.

Because of the considerable amount of diffuse X-ray emission in IC 2431, the CIAO point source detection routine `wavedetect` is not able to reliably identify point sources in the system. We therefore selected the brightest X-ray sources by eye for further analysis, using extraction apertures that range from  $1''.2 - 2''.0$  based on the appearance of the source. These ten sources are marked in the bottom panels of Figure 3. Source #1 – #9 were selected as local maxima in the 1.0 – 2.5 keV map, while source #10 was chosen based on a local maximum in the high energy 2.5 – 8.0 keV map. Source #10 does not have a discrete counterpart in the middle-energy map. Note that our region for source #10 overlaps with those of sources #7 and #8.

We assume that the X-ray source labeled #3 in Figure 3 at 9h 4m 34.98s,  $14^\circ 35' 35''.8$  is the galactic nucleus of Galaxy A, as its position agrees with that of the 4.86 GHz radio continuum maximum (see Section 2.5), and it is coincident within the positional uncertainties with the Spitzer mid-IR maximum and the 2MASS near-IR peak in Galaxy A. The hard X-ray source labeled #10 in Figure 3, at 9h 4m 34.54s,  $14^\circ 35' 42''.32$ , is coincident with the mid-IR maximum in Galaxy B, thus we assume it is the nucleus of Galaxy B. In addition to the two galactic nuclei and the overlapping source #7, two other sources, source #1 in the north of Galaxy A and source #6 in the north of Galaxy B, also have  $>10$  net counts in the high energy map.

In the medium-energy Chandra map, four knots of emission are seen along the disk of Galaxy B (regions #6, #7, #8, and #9). As noted earlier, the apparent nucleus of Galaxy B, the hard source #10, lies between two sources visible in the medium-energy maps (sources #7 and #8), but is not detected as a discrete source in the medium-energy map. No photons with energies less than 4 keV are detected from this apparent nuclear source, implying a high extinction. The X-ray spectra of these ten sources are analyzed in Section 3.5. Since the extraction aperture of source #10 overlaps with that of sources #7 and #8, the light from these sources will be blended in the spectral analysis.

Over the lifetime of its mission, Chandra has become less sensitive to low energy X-ray photons (Plucinsky et al. 2022). In the low energy range (0.5 – 1 keV), only a few dozen photons are detected from IC 2431, mostly from X-ray

<sup>10</sup> <https://sites.google.com/cfa.harvard.edu/saoimageds9>

sources #5, #6, and #9, thus we do not display a low energy map. This drop in sensitivity is incorporated into our calibration of the spectral fits (Section 3.5).

None of the X-ray sources in IC 2431 have sufficient counts for a reliable light curve. However, we can test whether these sources are variable by splitting the registered data into two sets and searching for differences. In Figure 4 we plot the count rates in 2024 vs. the count rates in 2023, in the medium energy range 1 – 2.5 keV (left panel), the high energy range 2.5 – 8 keV (middle panel), and the full energy range 0.5 – 8 keV (right panel). Between 2023 and 2024, the count rates of the apparent nuclei of both Galaxy A (source #3) and Galaxy B (source #10) dropped  $1\sigma$  or more in both the high energy range and the full 0.5 – 8 keV band. Source #6 in the northern part of Galaxy B also shows some evidence of variability at medium energies and in the full 0.5 – 8 keV band. In the 1.0 – 2.5 keV range, source #8 shows a  $1\sigma$  increase, and source #5 a  $1\sigma$  decrease.

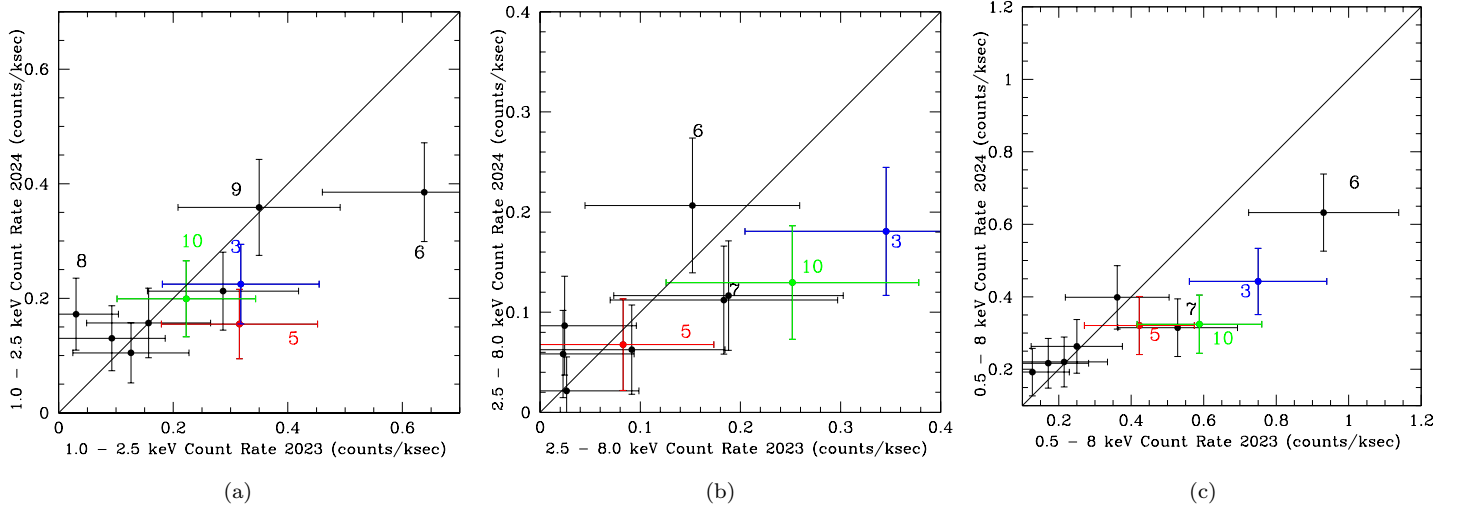


**Figure 4.** The Chandra count rates for the 2024 observations vs. the 2023 dataset, for the ten X-ray sources in IC 2431. These were extracted using the CIAO routine *dmextract*. Left: middle energy range (1.0 – 2.5 keV). Middle: high energy range (2.5 – 8.0 keV). Right: full range (0.5 – 8.0 keV). Source #3 (the apparent nucleus of Galaxy A) is plotted in blue; Source #10 (the apparent nucleus of Galaxy B) is plotted in green. Source #5 (between the two galaxies) is plotted in red. Some additional sources are labeled. The uncertainties on these rates were calculated using Gehrels (1986) statistics, i.e.,  $\sigma = 1 + \sqrt{N + 0.75}$ .

### 2.5. Radio Continuum Maps

IC 2431 was mapped at 4.86 GHz (C band; 6 cm) and 1.49 GHz (L band; 20 cm) by the Karl G. Jansky Very Large Array (VLA) (Stine 1992; Crawford et al. 1996). Two resolved sources are seen in the published VLA maps, associated with Galaxy A and Galaxy B. The quoted positions of the peak radio emission for the two galaxies agree within the uncertainties with the nuclear X-ray positions. According to Crawford et al. (1996), the nuclear radio source in Galaxy A may be variable, making it a possible AGN.

We have retrieved these VLA data from the archives, and re-reduced the data using the Common Astronomy Software Application (CASA; McMullin et al. 2007) version 6.5.4.9. Standard flagging and calibration techniques were followed. Imaging was performed with the *tclean* task, selecting a Briggs weighting at a robust value of one. Additionally, self-calibration was applied to the 4.86 GHz image. The final 4.86 GHz image has a local rms of  $0.06 \text{ mJy beam}^{-1}$ , with a restoring beam of  $0''.61 \times 0''.41$ . There are two 1.49 GHz datasets, from 1987 and 1991. These have local rms noise levels of 0.4 and  $0.3 \text{ mJy beam}^{-1}$ , and restoring beams of  $1''.71 \times 1''.45$  and  $2''.19 \times 1''.40$ , respectively. In the following analysis we use the 1991 dataset since it is deeper.

We compare the VLA maps of Galaxy A and Galaxy B with the HST, Spitzer, and Chandra maps in Figure 5 (Galaxy C is undetected in the VLA maps). The 4.86 GHz and 1.49 GHz images are presented in the left and right columns of panels, respectively, of Figure 5. The superimposed contours are from the HST F606W image (top row), the Spitzer  $8 \mu\text{m}$  map (second row), the 1.0 – 2.5 keV Chandra image (third row), and the 2.5 – 8.0 keV Chandra map (bottom row). The brightest source in Galaxy A at 4.86 GHz is coincident with the hard X-ray peak, the presumed



galactic nucleus (bottom left panel). An intriguing ridge-like/jet-like feature extends about  $4''$  to the northwest of this nucleus at both radio frequencies. This feature is discussed further below.

In the 1.49 GHz map, a larger but fainter filament of diffuse emission extends about  $8''$  to the northeast of this radio ridge/jet. This radio filament is offset from the disk of Galaxy A as seen in the optical (top right panel), and is slightly northwest of the star-forming region in the north of Galaxy A seen in the Spitzer map (right panel, second from top). This radio structure is roughly coincident with a dust feature seen in the optical map (top right panel).

Galaxy B has diffuse 1.49 GHz emission spread out over about  $10''$  along the galactic disk. The extent of this diffuse emission approximately matches that of the  $8\ \mu\text{m}$  emission. The brightest region in Galaxy B at both radio frequencies is not the apparent nucleus, but instead is close to X-ray source #6 in the north. Another radio knot is visible in the southwest of Galaxy B, approximately coincident with X-ray source #9 in the medium energy Chandra map. Sources #6 and #9 may be intense star-forming regions.

In Figure 6, we zoom in on the nuclear region of Galaxy A, and compare the two radio maps with maps at other wavelengths. In the 4.86 GHz map (top left panel), the brightest source in Galaxy A is a point source coincident with the apparent nucleus as seen in the X-ray, source #3 (bottom middle panel). Extending about  $3'' - 4''$  to the northwest of this nucleus in the radio maps is the ridge/jet, which has a maximum about  $2''$  away from the nucleus. This feature is approximately perpendicular to the galactic disk as seen in the HST data (top right panel). The peak brightness of this ridge lies about  $3''$  east of X-ray source #5 (bottom right panel). The radio ridge/jet is approximately aligned along the  $8\ \mu\text{m}$  bridge (bottom right panel). In the 1.49 GHz maps, the ridge is brighter than the nucleus, while in the 4.86 GHz map, the nucleus is brighter. This indicates different radio spectral indices for the nucleus and the ridge, as discussed below. With the exception of the nucleus itself, the radio ridge/jet is anti-coincident with the X-ray emission in the region (bottom left panel). In the 1.49 GHz map (top middle panel), fainter diffuse emission is seen extending about  $4''$  to the northeast of the radio ridge. At 4.86 GHz, the integrated flux for the ridge plus nucleus is  $5.3 \pm 0.2$  mJy (spread over 13.4 beams) and the point source at the nucleus is  $1.04 \pm 0.06$  mJy beam $^{-1}$ . At 1.49 GHz, the integrated flux of this region is  $19.9 \pm 0.6$  mJy (spread over 3.2 beams). Our approximate estimate for the nucleus at 1.49 GHz is  $3.4 \pm 0.3$  mJy beam $^{-1}$ , but this is uncertain because of blending with the extended emission from the ridge. At 1.49 GHz, the source is not centrally-peaked; there is enhanced flux near the nucleus but also at the end of the ridge. This morphology is what is expected if there is an active AGN and a jet interaction with interstellar gas downstream. This possibility is discussed further in Section 5.2.

We also constructed a radio spectral index map (Figure 7). The 4.86 GHz image was convolved with the beam of the 1991 1.49 GHz image. Next, using the CASA task `regrid`, we re-gridded the 1.49 GHz image to match the 4.86 GHz image. Each image is then masked to their respective  $3\sigma$  thresholds and, finally, we created a two-point spectral image map. We define the radio spectral  $\alpha$  by flux density  $S_\nu \propto \nu^\alpha$ . In Figure 7, we compare the spectral index (middle panel) with the HST F606W image (left panel), and a map of the uncertainty in  $\alpha$  (right panel).

The nuclear region of Galaxy A has a spectral index of about  $-0.6$ , with  $\alpha$  decreasing (steepening) along the ridge/jet to a minimum of around  $-1.1$  near the NW tip. The northern part of Galaxy B has a spectral index of approximately  $-0.6$ ; this increases (flattens) to  $\alpha = -0.1$  to  $-0.2$  in the southern part of Galaxy B. In the middle panel of Figure 7, a striking offset is seen in the southern part of Galaxy B between the radio continuum and the optical, with the sources seen in the optical shifted to the north of the radio emission. This offset is seen more clearly in Figure 8, a zoomed-in picture of the southern portion of Galaxy B.

### 3. ANALYSIS

#### 3.1. UV/Optical/IR Photometry

We extracted fluxes in the GALEX, SDSS, DES, HST, 2MASS, and Spitzer bands in three large rectangular regions enclosing Galaxy A, Galaxy B, and Galaxy C (see Figure 9). For sky determination, we selected large regions off the galaxies away from foreground stars. For all of the available filters plus the four WISE bands, we also extracted fluxes for the full IC 2431 system within a  $24''$  radius aperture, and for the combined A+B system within a  $12''$  radius system. The photometry was corrected for Galactic absorption as in Schlafly and Finkbeiner (2011) and Yuan et al. (2013). The final fluxes for each region are given in Appendix A, along with the central coordinates of the region, the major and minor axes of the rectangular region, and its position angle on the sky.

As shown in Figure 9, we sub-divided the Galaxy A and Galaxy B rectangles into four and three slices, respectively. These regions are large enough for reliable photometry of extended sources with GALEX. Photometry for these smaller rectangular regions are also given in Appendix A.

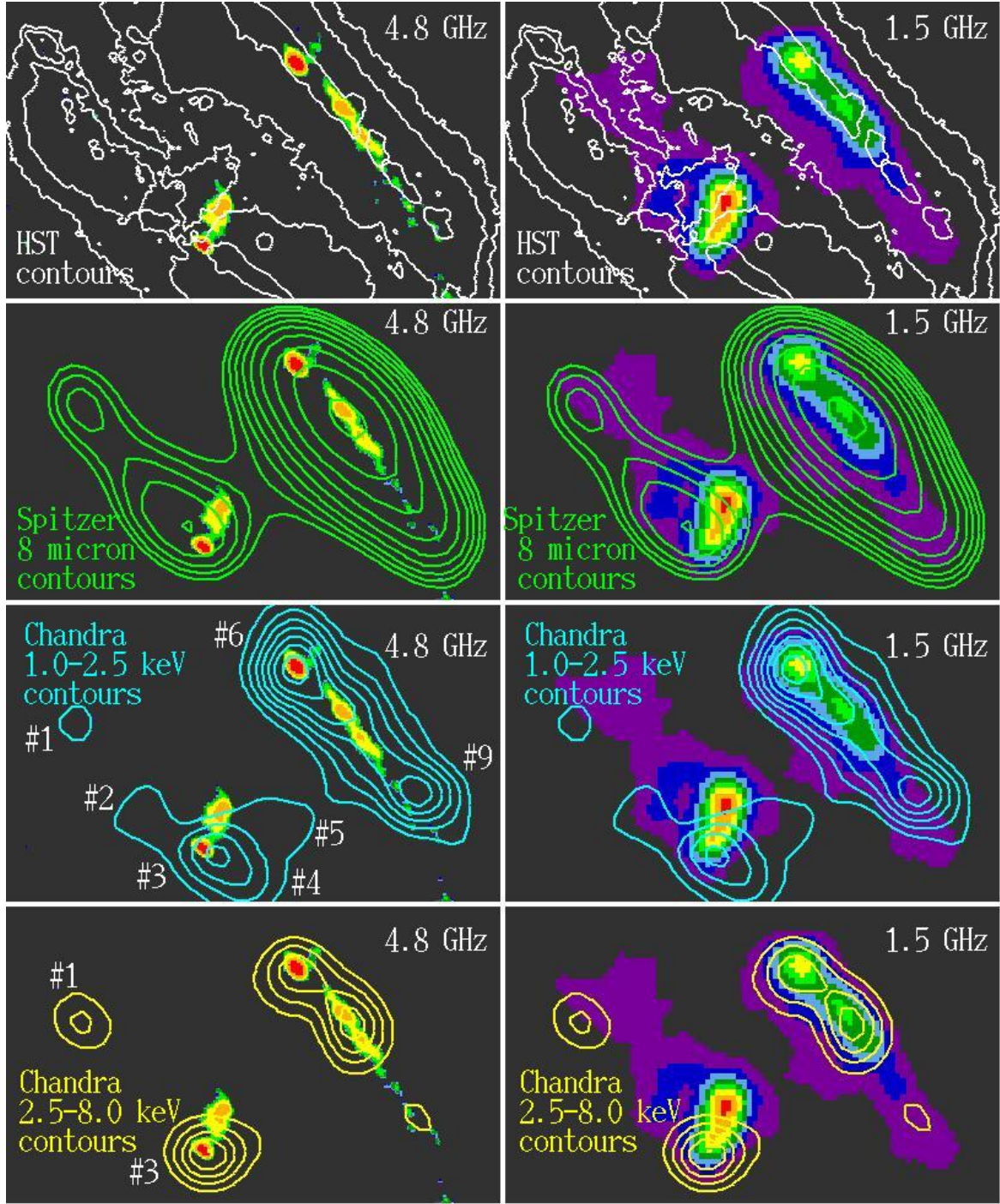


**Figure 5.** Comparison of the radio continuum maps with data at other wavelengths. Left panels: the 4.86 GHz map. Right panels: the 1.49 GHz map. The contours in the first row are from the HST F606W map, selected to delineate the dust feature crossing Galaxy A. The contours in the second row are from the Spitzer 8  $\mu$ m map, chosen to emphasize the mid-infrared bridge and the star-forming regions in Galaxy A. The contours in the third row are from the Chandra 1.0 – 2.5 keV map, selected to outline some of the X-ray sources mentioned in the text. Sources #1, #2, #3, #4, #5, #6, and #9 are labeled in the left panel of the third row. The contours in the fourth row are from the Chandra 2.5 – 8.0 keV map. X-ray sources #1 and #3 are labeled in the left panel. The spatial resolution for the 1.49 GHz map is  $2''.19 \times 1''.40$ , and for the 4.86 GHz map is  $0''.61 \times 0''.41$ . The field of view is  $22''.2 \times 13''.3$ , with north up and east to the left.

In Sections 3.2 and 3.4, we use these fluxes to derive SFRs, stellar masses, and extinctions.



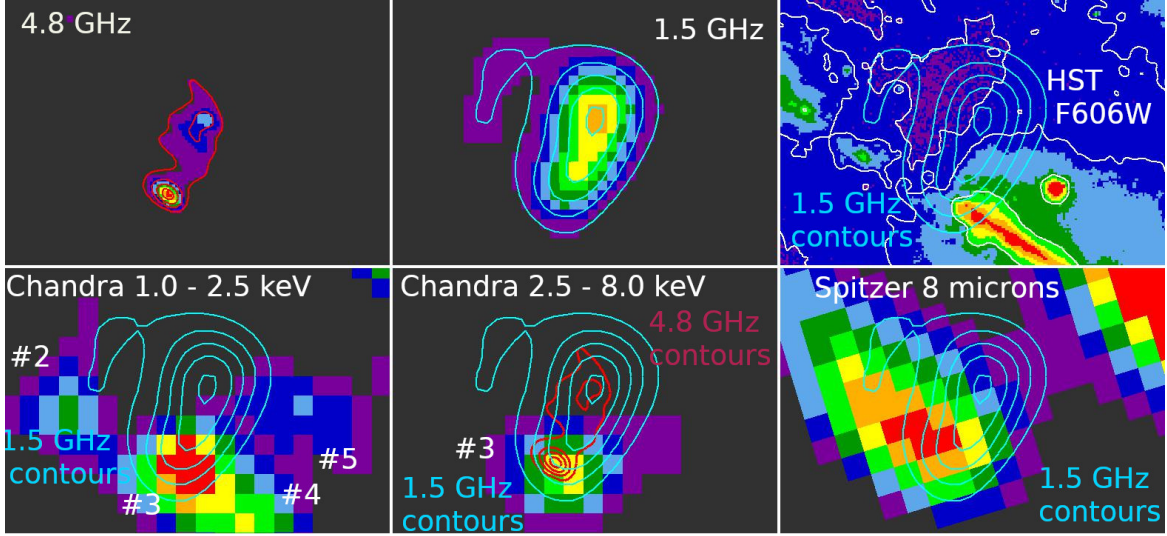


**Figure 6.** A multi-wavelength comparison of the region around the nucleus of Galaxy A. Top left: the 4.86 GHz map. Top middle: the 1.49 GHz map. Top right: the HST F606W image, with 1.49 GHz contours (cyan), and contours from the HST image itself (white contours). The contours on the HST image are selected to outline dust features; the dust lane is visible in the upper middle of this picture, color-coded in purple. Bottom left: the medium-energy Chandra map, with 1.49 GHz contours. X-ray sources #2, #3, #4, and #5 are marked. Bottom middle: the high-energy Chandra map, with contours from both 1.49 GHz (cyan) and 4.86 GHz (red). X-ray source #3 is marked. Bottom right: The Spitzer 8  $\mu$ m image, with contours from the 1.49 GHz map. The field of view is  $9''.5 \times 6''.6$ , with north up and east to the left.

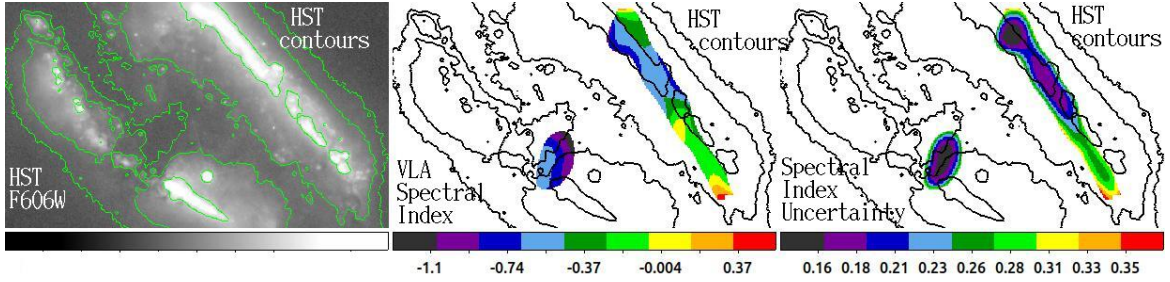


**Figure 7.** Left: the HST F606W map. Middle: the VLA spectral index map, defined by flux density  $S_\nu \propto \nu^\alpha$ . Right: the uncertainty in the radio spectral index. Contours from the HST map are overlaid on all of the images. The field of view is  $22''.2 \times 13''.3$  with north up and east to the left.

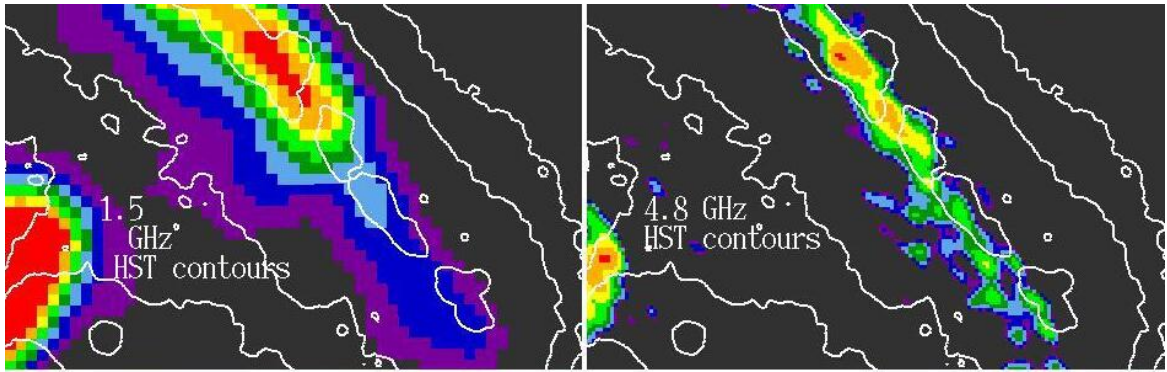


**Figure 8.** The southern portion of Galaxy B. Left: The VLA 1.49 GHz map, with HST contours superimposed. Right: The VLA 4.86 GHz map, with HST contours superimposed. The field of view is about  $18'' \times 8''$ , with north up and east to the left.



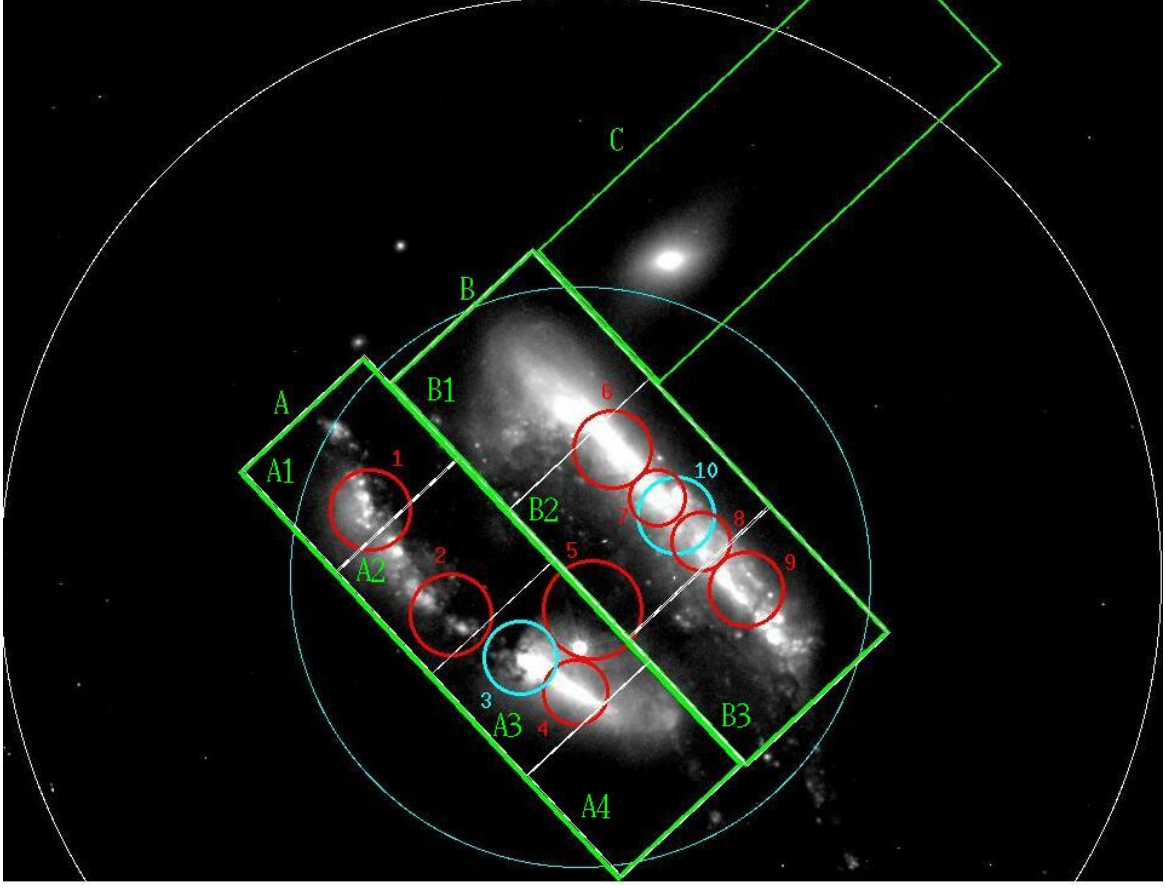


**Figure 9.** The HST F606W image with various regions overlaid. The large rectangular regions in green are the regions in which the fluxes for Galaxies A, B, and C were extracted. The regions for Galaxy A and B are divided into smaller rectangular regions as shown by the white lines (four regions for Galaxy A and three for Galaxy B). These smaller regions are labeled A1, A2, A3, A4, B1, B2, and B3. The 12'' radius circle that includes most of the Chandra X-ray flux is shown in cyan. A larger circle with a 24'' radius (in white) includes most of the tidal tails as seen in the optical. The ten smaller regions marking the X-ray sources are shown in red or (for the galactic nuclei) in cyan. The field of view is approximately  $47'' \times 36''$ , with north up and east to the left.

### 3.2. Star Formation Rates and Dust Absorption from UV and IR Fluxes, vs. Radio Continuum Fluxes

From our  $22\ \mu\text{m}$  and FUV fluxes in the  $24''$  radius aperture, we derive a total SFR for IC 2431 of  $37\ \text{M}_{\odot}\ \text{yr}^{-1}$  using the Hao et al. (2011) formula assuming a Kroupa initial mass function (IMF; Kroupa & Weidner 2003). We also derive an FUV extinction  $A_{\text{FUV}} = 2.3$  from the Hao et al. (2011) relation. This implies  $A_V = 0.92$ , using the Calzetti et al. (2000) extinction law, and  $E(B-V) = 0.30$ , using  $A_V/E(B-V) = 3.1$ . From this, we infer a hydrogen column density of  $N_{\text{H}} = 1.7 \times 10^{21}\ \text{cm}^{-2}$  using the Bohlin et al. (1978) relation of  $N_{\text{H}}/E(B-V) = 5.8 \times 10^{21}\ \text{cm}^{-2}\ \text{mag}^{-1}$ .

The individual galaxies that make up IC 2431 are not resolved in the WISE  $22\ \mu\text{m}$  image, so we cannot derive SFRs for the three galaxies separately using WISE data. However, the galaxies are resolved in the Spitzer  $8\ \mu\text{m}$  image. The  $8\ \mu\text{m}$  luminosity of star-forming galaxies is also correlated with SFR (Wu et al. 2005; Zhu et al. 2008), so can be used as a rough measure of SFR, however, there are some complications. First, one needs to correct for contributions from the underlying stellar continuum in the Spitzer  $8\ \mu\text{m}$  band (Helou et al. 2004). Second, in low metallicity systems such as dwarf galaxies, the polycyclic aromatic hydrocarbon (PAH) features which dominate the broadband Spitzer  $8\ \mu\text{m}$  filter tend to be weaker for the same SFR (Madden 2000; Engelbracht et al. 2005, 2008; Wu et al. 2006, 2007). This should not be a problem for IC 2431, however, since the stellar masses of the two main galaxies are relatively high (see below), and therefore they are not dwarf galaxies. Third, PAH features can be destroyed in star forming regions with intense UV radiation fields (Dale et al. 1999; Binder & Povich 2018; Belfiore et al. 2023). A fourth issue is that, in regions with strong interstellar shocks, the mid-infrared  $\text{H}_2$  S(5) and S(4) emission lines at  $6.91\ \mu\text{m}$  and  $8.03\ \mu\text{m}$

$\mu\text{m}$ , respectively, may contribute to the broadband Spitzer flux in the  $8\ \mu\text{m}$  filter (Cluver et al. 2010). A fifth issue is that the  $7.7\ \mu\text{m}$  PAH feature shifts with redshift relative to the broadband Spitzer  $8.0\ \mu\text{m}$  bandpass, thus ideally a K-correction should be applied to the data to account for this shift. The latter three issues are discussed further in Section 4.2.

To estimate the SFR from the Spitzer  $8\ \mu\text{m}$  luminosity,  $\text{SFR}_{8\ \mu\text{m}}$ , we use the relation from Zhu et al. (2008) after converting to a Kroupa IMF:  $\text{SFR}_{8\ \mu\text{m}} = 1.04 \times 10^{-43} L_{8\ \mu\text{m}}$ , where the SFR is in  $\text{M}_{\odot}\ \text{yr}^{-1}$ ,  $L_{8\ \mu\text{m}} = \nu L_{\nu}$  in  $\text{erg s}^{-1}$ ,  $\nu$  is the frequency in Hertz, and  $L_{\nu}$  is the monochromatic luminosity per frequency in units of  $\text{erg s}^{-1}\ \text{Hz}^{-1}$  after correction for the stellar continuum. We assume that the flux density of the stellar continuum contribution to the  $8\ \mu\text{m}$  band,  $F_{8\ \mu\text{m}}(\text{stars})$ , is equal to  $0.232 F_{3.6\ \mu\text{m}}$  (Helou et al. 2004), where  $F_{3.6\ \mu\text{m}}$  is the flux density in the Spitzer  $3.6\ \mu\text{m}$  filter. We combine  $\text{SFR}_{8\ \mu\text{m}}$  with the unobscured SFR seen in the GALEX FUV band,  $\text{SFR}_{\text{FUV}}$ , defined as  $\text{SFR}_{\text{FUV}} = 4.47 \times 10^{-44} L_{\text{FUV}}$  (Murphy et al. 2011; Hao et al. 2011), where  $L_{\text{FUV}}$  is  $\nu L_{\nu}$  in the FUV. The total composite SFR formula from the FUV and  $8\ \mu\text{m}$  together is thus  $\text{SFR}_{\text{total}} = 4.47 \times 10^{-44} (L_{\text{FUV}} + 2.33 L_{8\ \mu\text{m}})$ . We use these formulae to calculate  $\text{SFR}_{\text{total}}$ , as well as the implied extinction  $E(B-V)$  and estimates of  $N_{\text{H}}$ . The total SFRs and absorption estimates for the individual galaxies as well as the smaller rectangular areas in IC 2431 are given in columns 2 – 4 of Table 2. In Section 3.4 we compare the above estimates of  $N_{\text{H}}$  with values obtained from population synthesis modeling.

For all of our targeted regions in IC 2431,  $\text{SFR}_{8\ \mu\text{m}}$  is considerably larger than  $\text{SFR}_{\text{FUV}}$ , implying relatively high absorption. The lowest absorption is seen towards Galaxy C, while the three slices in the northern part of Galaxy A (regions A1, A2, and A3) have the highest inferred absorption,  $N_{\text{H}} = 2.4 - 3.1 \times 10^{21}\ \text{cm}^{-2}$ . According to these calculations, the SFR of Galaxy A is about 38% of that of Galaxy B. The total SFR for the full  $24''$  radius region of  $39\ \text{M}_{\odot}\ \text{yr}^{-1}$  obtained from the  $8\ \mu\text{m} + \text{FUV}$  measurements agrees well with that derived from  $22\ \mu\text{m} + \text{FUV}$ . This agreement argues that the  $8\ \mu\text{m}$  is a reasonably good measure of the SFR in this system.

Rowan-Robinson et al. (1991) report  $60\ \mu\text{m}$  and  $100\ \mu\text{m}$  flux densities for IC 2431 from the Infrared Astronomical Satellite (IRAS) of 4.43 Jy and 7.63 Jy, respectively, extracted from the IRAS Point Source Catalog (Helou & Walker 1988). Refining these values using the xscanpi software<sup>11</sup>, we obtain fluxes of 4.4 Jy and 5.43 Jy at  $60\ \mu\text{m}$  and  $100\ \mu\text{m}$ , respectively. This implies a far-infrared luminosity ( $42.5 - 112.5\ \mu\text{m}$ ) of  $2.8 \times 10^{11}\ L_{\odot}$ , using the Helou et al. (1985) relation. Converting to total infrared ( $3 - 1000\ \mu\text{m}$ ) luminosity using the method of Dale & Helou (2002) gives  $L(\text{IR})$  of  $5.3 \times 10^{11}\ L_{\odot}$ . Converting this to a SFR using the relation of Murphy et al. (2011) yields a SFR of  $80\ \text{M}_{\odot}\ \text{yr}^{-1}$ . This is 2.2 times larger than our global estimate of the SFR from the UV plus mid-IR.

Stine (1992) compared the radio and far-infrared luminosities of 30 starburst galaxies, including IC 2431. Of these 30 galaxies, IC 2431 has the lowest far-infrared to radio ratio, a factor of  $\sim 5$  times less at both 6 cm and 20 cm than the mean for the other galaxies. Compared to a sample of other luminous infrared galaxies, Crawford et al. (1996) find a FIR to 20 cm ratio for IC 2431 that is low by about a factor of five. This apparent radio excess from IC 2431 is especially intriguing given that the radio continuum from this system is resolved; for both Galaxy A and Galaxy B, the integrated light at 6 cm is about twice that of the peak emission (Crawford et al. 1996). A majority of the excess radio emission from IC 2431 is apparently coming from Galaxy A. Comparing with our SFRs for the two galaxies obtained from the UV plus  $8\ \mu\text{m}$  fluxes, the radio to SFR ratios for Galaxy A are about twice that of Galaxy B. This supports the idea that Galaxy A hosts a radio AGN, or some other process has enhanced the radio continuum emission relative to that expected from star formation alone.

### 3.3. UV/Optical/IR Spectral Energy Distributions

In the left panel of Figure 10, we provide spectral energy distribution (SED) plots for the three galaxies in IC 2431. The SEDs of Galaxy A and Galaxy B differ dramatically; Galaxy B has significantly more UV and blue light than Galaxy A, although the near-IR fluxes of the two galaxies are similar. Galaxy B is also much brighter in the mid-IR than Galaxy A. The SED of Galaxy C suggests a quiescent but relatively unobscured stellar population, with proportionally little mid-infrared and UV compared to the visible.

The middle panel of Figure 10 gives SED plots for the four rectangular regions in Galaxy A. Region A3, which contains the nuclear region, is by far the brightest of the four Galaxy A regions in the optical and near-infrared, and is proportionally fainter in the UV and mid-IR. This implies a large older stellar population and proportionally fewer

<sup>11</sup> <https://irsa.ipac.caltech.edu/applications/Scanpi/>

**Table 2.** Star Formation Rates and Absorption in Various Regions in IC 2431

Region	From FUV plus 8 $\mu\text{m}$			From CIGALE								
	SFR ( $\text{M}_{\odot}/\text{yr}$ )	E(B-V)	N(H) ( $\times 10^{22}$ $\text{cm}^{-2}$ )	SFR ( $\text{M}_{\odot}/\text{yr}$ )	log M* ( $\text{M}_{\odot}$ )	log sSFR ( $\text{yr}^{-1}$ )	E(B-V) (stars)	E(B-V) (lines)	N(H) ( $\times 10^{22}$ $\text{cm}^{-2}$ )	N(H) ( $\times 10^{22}$ $\text{cm}^{-2}$ )	Age (Myrs)	$r_{\text{SFR}}$
12'' circle	34.8 $\pm$ 0.01	0.31 $\pm$ 0.01	0.18 $\pm$ 0.01									
24'' circle	38.76 $\pm$ 0.02	0.3 $\pm$ 0.01	0.18 $\pm$ 0.01									
Galaxy A	8.97 $\pm$ 0.01	0.45 $\pm$ 0.01	0.26 $\pm$ 0.01	8.5 $\pm$ 2.06	10.75 $\pm$ 0.04	-9.81 $\pm$ 0.11	0.28 $\pm$ 0.04	0.81 $\pm$ 0.28	0.16 $\pm$ 0.02	0.47 $\pm$ 0.16	34 $\pm$ 35	1.3 $\pm$ 1.16
Galaxy B	23.76 $\pm$ 0.01	0.28 $\pm$ 0.01	0.16 $\pm$ 0.01	18.32 $\pm$ 9.37	10.74 $\pm$ 0.07	-9.47 $\pm$ 0.23	0.19 $\pm$ 0.04	0.62 $\pm$ 0.25	0.11 $\pm$ 0.02	0.36 $\pm$ 0.15	44 $\pm$ 38	5.3 $\pm$ 2.54
Galaxy C	0.5 $\pm$ 0.01	0.18 $\pm$ 0.02	0.11 $\pm$ 0.01	1.04 $\pm$ 0.45	10.18 $\pm$ 0.07	-10.15 $\pm$ 0.2	0.12 $\pm$ 0.04	0.35 $\pm$ 0.22	0.07 $\pm$ 0.02	0.2 $\pm$ 0.13	48 $\pm$ 34	0.49 $\pm$ 0.46
Region A1	2.2 $\pm$ 0.01	0.42 $\pm$ 0.01	0.24 $\pm$ 0.01	1.82 $\pm$ 0.85	9.56 $\pm$ 0.08	-9.29 $\pm$ 0.22	0.25 $\pm$ 0.04	0.64 $\pm$ 0.24	0.15 $\pm$ 0.02	0.37 $\pm$ 0.14	53 $\pm$ 37	6.32 $\pm$ 2.42
Region A2	3.35 $\pm$ 0.01	0.53 $\pm$ 0.02	0.31 $\pm$ 0.01	2.12 $\pm$ 1.28	10.24 $\pm$ 0.06	-9.91 $\pm$ 0.27	0.39 $\pm$ 0.03	0.91 $\pm$ 0.33	0.22 $\pm$ 0.01	0.53 $\pm$ 0.19	30 $\pm$ 29	8.07 $\pm$ 2.68
Region A3	2.89 $\pm$ 0.01	0.48 $\pm$ 0.02	0.28 $\pm$ 0.01	2.25 $\pm$ 1.23	10.56 $\pm$ 0.05	-10.2 $\pm$ 0.24	0.23 $\pm$ 0.05	0.73 $\pm$ 0.27	0.14 $\pm$ 0.03	0.42 $\pm$ 0.16	62 $\pm$ 33	0.28 $\pm$ 0.24
Region A4	0.53 $\pm$ 0.01	0.26 $\pm$ 0.02	0.15 $\pm$ 0.01	0.61 $\pm$ 0.11	9.68 $\pm$ 0.03	-9.89 $\pm$ 0.09	0.12 $\pm$ 0.02	0.33 $\pm$ 0.17	0.07 $\pm$ 0.01	0.19 $\pm$ 0.1	39 $\pm$ 35	0.6 $\pm$ 0.39
Region B1	2.7 $\pm$ 0.01	0.17 $\pm$ 0.01	0.1 $\pm$ 0.01	2.61 $\pm$ 0.39	10.2 $\pm$ 0.03	-9.77 $\pm$ 0.07	0.07 $\pm$ 0.02	0.13 $\pm$ 0.07	0.04 $\pm$ 0.01	0.07 $\pm$ 0.04	28 $\pm$ 34	1.22 $\pm$ 0.94
Region B2	13.58 $\pm$ 0.01	0.32 $\pm$ 0.01	0.19 $\pm$ 0.01	8.76 $\pm$ 3.86	10.47 $\pm$ 0.08	-9.52 $\pm$ 0.21	0.23 $\pm$ 0.03	0.82 $\pm$ 0.19	0.14 $\pm$ 0.01	0.48 $\pm$ 0.11	39 $\pm$ 34	6.18 $\pm$ 2.45
Region B3	7.49 $\pm$ 0.01	0.29 $\pm$ 0.01	0.17 $\pm$ 0.01	5.8 $\pm$ 2.66	10.02 $\pm$ 0.09	-9.25 $\pm$ 0.22	0.22 $\pm$ 0.03	0.69 $\pm$ 0.24	0.13 $\pm$ 0.02	0.4 $\pm$ 0.14	48 $\pm$ 34	8.84 $\pm$ 2.18



young stars. In contrast, the most northern region, region A1, is the brightest of the four regions in the UV and is the bluest in the optical, and is also quite bright at  $8\ \mu\text{m}$ , but is faint in the near-IR. This suggests very recent star formation, but not a large underlying older stellar population. Region A2 (which contains part of the dust lane) is quite bright in the near-IR and mid-IR, but fainter in the UV and short-wavelength optical, implying a lot of dust extinction. Region A4, the most southern region, has a SED that peaks in the optical, but has proportionally far less mid-IR than the other regions. This indicates that Region A4 is more quiescent.

The right panel of Figure 10 compares the SEDs for the three rectangular regions in Galaxy B. The northern region B1 is brightest in the optical, drops with increasing wavelength to  $4.5\ \mu\text{m}$ , then increases somewhat at  $8\ \mu\text{m}$ . The SEDs of both the middle region B2 and the southern region B3 peak at  $8\ \mu\text{m}$  and are faintest at  $4.5\ \mu\text{m}$ , but B2 is much brighter in the 2MASS bands. This suggests that B2 includes the galactic bulge, and B3 has a younger stellar population than B1. The northern part of Galaxy B is more quiescent than the south. These differences are discussed further below.

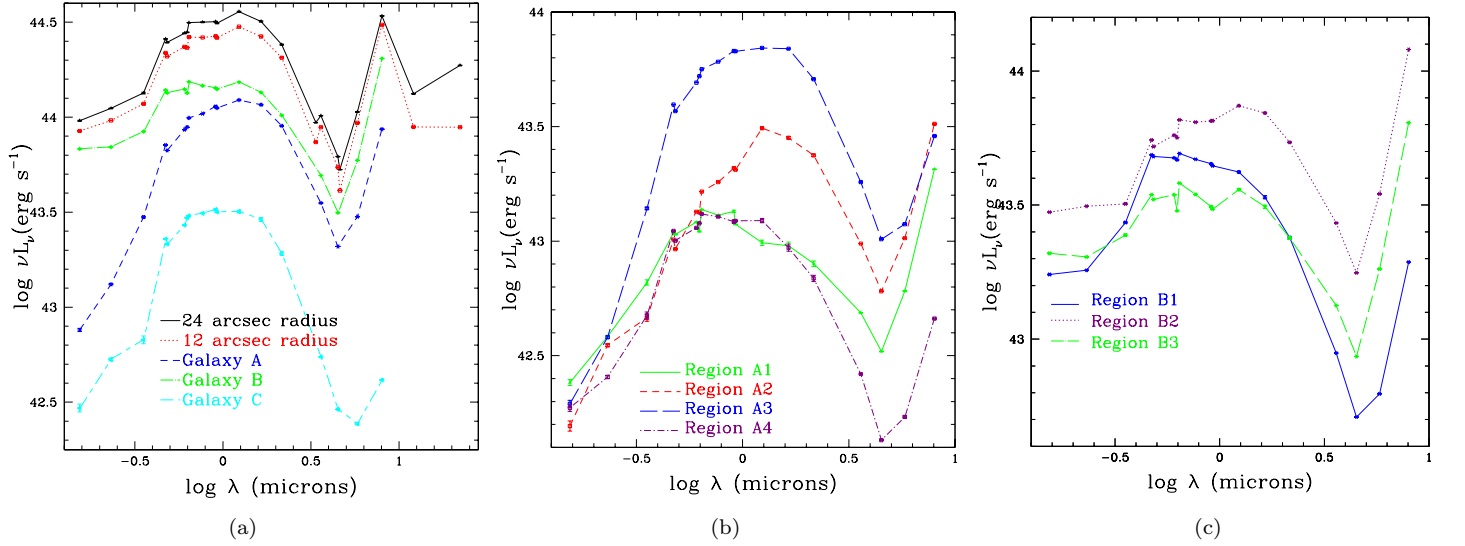


**Figure 10.** Left: Spectral energy distributions for the full IC 2431 system, compared to the SEDs of the individual galaxies (see Table 6). Middle: Spectral energy distributions of the four rectangular regions within Galaxy A, as identified in the caption. From north to south in the galaxy, they are regions A1, A2, A3, and A4. Right: Spectral energy distributions of regions B1, B2, and B3 in IC 2431 (see the Appendix for the photometry).

### 3.4. Population Synthesis Modeling

We fit the SEDs for the various regions in IC 2431 to population synthesis models using the Code Investigating GALaxy Emission (CIGALE) software (Boquien et al. 2019). The framework we use to establish these parameters follows that of Dale et al. (2023). We used single stellar populations from Bruzual & Charlot (2003), dust emission models from Draine et al. (2014), and the Calzetti et al. (2000) modified dust law with the UV bump amplitude set to zero. We assumed solar metallicity. We used the Chabrier (2003) IMF, which produces almost identical SFRs as the Kroupa IMF (Chomiuk & Povich 2011; Kennicutt & Evans 2012). For the star formation history, we used the ‘delayed star formation history with a late burst’ module in CIGALE, which can include either a recent burst or a recent quenching episode.

CIGALE calculates a Bayesian-like estimate of various parameters and their uncertainties based on a likelihood-weighting scheme involving the  $\chi^2$  value for each grid point. Since the nominal statistical uncertainties in our photometry are likely underestimates of the actual uncertainties, we use CIGALE’s default across-the-board flux uncertainty of 10%, which is combined in quadrature with the listed uncertainties. In columns 5 – 13 of Table 2, we provide the CIGALE fits for several parameters, including the SFR, the stellar mass, the age of the late burst/quench, the ratio of the SFR after vs. before the burst ( $r_{\text{SFR}}$ , a measure of the relative intensity of the starburst), the  $B - V$  color excess  $E(B - V)$  for the stars and, separately,  $E(B - V)$  for the emission lines. We use the GALEX, SDSS, 2MASS, and Spitzer

photometry in these fits. The SFRs obtained from CIGALE are averaged over the last 100 Myrs, thus, as expected, they agree fairly well with the SFRs derived from the FUV plus  $8\ \mu\text{m}$  fluxes, which average over similar timescales. More details on the CIGALE fitting and additional parameters are provided in Appendix B.

Galaxy B has the highest sSFR of the galaxies in the group, and Galaxy C the lowest. Among the smaller rectangular regions measured, the southernmost region in Galaxy B, region B3, has the highest sSFR, followed closely by A1 in the north of Galaxy A. Region A3, which includes the galactic bulge of Galaxy A, has the lowest sSFR of all the smaller regions measured. Region A3 also has the lowest pre/post-starburst SFR ratio of all of the regions measured,  $r_{\text{SFR}} = 0.28 \pm 0.24$ , implying recent quenching rather than a starburst. In contrast, regions A1, A2, B2, and B3 all have high  $r_{\text{SFR}}$  of  $6 - 8 \pm 2$ , indicating a starburst, with region B3 having the highest ratio. The northern region in Galaxy B, B1, and the southern region in Galaxy A, A4, have  $r_{\text{SFR}} \sim 1$ , meaning little change in the SFR over the last 100 Myrs. All of the regions identified as starbursts (A1, A2, B2, and B3) have similar burst ages of  $30 - 55 \pm 35$  Myrs, with A2 being the youngest and A1 the oldest.

In Table 2, we convert the CIGALE  $E(B-V)$  values to  $N_{\text{H}}$  using the Bohlin et al. (1978) relation. The extinctions found by CIGALE are reasonably consistent with those implied by the  $8\ \mu\text{m}$  to FUV flux ratios. CIGALE found the lowest dust absorption for the northern region of Galaxy B, region B1, and the highest extinction for region A2, which covers part of the dust lane. In Section 3.5, we compare these estimates of  $N_{\text{H}}$  to the X-ray absorptions inferred from the Chandra spectra.

### 3.5. Chandra X-Ray Spectral Analysis

#### 3.5.1. Global Galaxy Fits

We used the CIAO routine `specextract` to extract and combine the Chandra X-ray spectra within various regions in IC 2431. Figure 11 displays the Chandra spectrum for the full system within a  $12''$  radius region (left panel), the rectangular region around Galaxy A (middle panel), and the rectangular region enclosing Galaxy B (right panel). We used the `xspec` software to fit these spectra to two components, a power law and a thermal APEC (Astrophysical Plasma Emission Code) function. In these fits, we fixed the redshift to 0.0497, the metallicity to solar, and the Galactic absorption to  $4 \times 10^{20}\ \text{cm}^{-2}$  (Dickey and Lockman 1990)<sup>12</sup>. We used the Wilms et al. (2000) abundance table. We limited the fit to the energy range  $0.5 - 7\ \text{keV}$ . In these fits, we fit for a single value of the internal absorption, the photon index  $\Gamma$  of the power law component, and the temperature of the thermal gas.

Results of the fitting are given in Table 3. Because of the relatively low number of counts from this system, we report Cash statistics (C-statistics; Cash 1979) for these fits, along with the degrees of freedom (DOF). Our best-fit models are overlaid on the data in Figure 11, along with the best-fit thermal and power law components. The total observed Chandra flux in the  $12''$  radius region is  $9.9 \pm 0.1 \times 10^{-14}\ \text{erg s}^{-1}\ \text{cm}^{-2}$ . In the global spectrum and the spectrum for Galaxy B, the Si XIII 1.87 keV feature is seen, as is the Mg XI 1.343/1.352 keV feature. The 0.8 keV Fe L complex is also visible. In the global spectrum and in Galaxy B, the thermal component dominates at energies below 2.5 keV, while the power law component dominates at higher energies. In Galaxy A, the power law component dominates down to about 1.5 keV.

For the system as a whole, the best-fit temperature of the APEC component,  $kT = 0.92 \pm 0.13_{0.58}^{\text{keV}}$ , is relatively well-constrained, but the photon index  $\Gamma$  of the power law component is not ( $1.06 \pm 0.78_{0.91}$ ). The best-fit model for the system as a whole gives a high internal  $N_{\text{H}}$  of  $7.6 \pm 2.1_{2.6} \times 10^{21}\ \text{cm}^{-2}$ . For Galaxy A alone, the best-fit  $N_{\text{H}} = 5.8 \pm 3.6_{4.6} \times 10^{21}\ \text{cm}^{-2}$  agrees well with the CIGALE results for line emission of  $N_{\text{H}} = 4.7 \pm 0.16 \times 10^{21}\ \text{cm}^{-2}$ . The best-fit temperature for Galaxy A,  $0.85 \pm 0.16_{0.48}^{\text{keV}}$ , is moderately-well constrained, though  $\Gamma = 1.05 \pm 0.64_{0.85}$  is not. This  $\Gamma$ , and the  $\Gamma$  for the system as a whole, are significantly smaller than typical for AGNs and HMXBs. AGNs usually have  $\Gamma$  in the range  $1.6 - 2.0$  (Nandra & Pounds 1994; George et al. 2000; Piconcelli et al. 2003; Tozzi et al. 2006), while luminous HMXBs typically have  $\Gamma = 1.8 \pm 0.1$  (Kong et al. 2002; Swartz et al. 2004; Lehmer et al. 2022). Variations in absorption and X-ray spectral shape across Galaxy A may be responsible for these unusually low values of  $\Gamma$ .

For Galaxy B alone, the best-fit  $N_{\text{H}}$  of  $9.0 \pm 3.8_{5.0} \times 10^{21}\ \text{cm}^{-2}$  is  $2.3 \times$  the value from CIGALE for line emission. This suggests that the sources of X-ray emission are more deeply embedded on average than typical star-forming regions dominating the UV/optical/IR emission. The temperature for Galaxy B,  $0.58 \pm 0.35_{0.21}^{\text{keV}}$ , is moderately-well

<sup>12</sup> from COLDEN at <https://cxc.harvard.edu/toolkit/colden.jsp>

**Table 3.** Chandra Spectral Results for Galaxy A, Galaxy B, and IC 2431 as a Whole

ID	$N_H$ ( $\times 10^{22}$ $\text{cm}^{-2}$ )	kT (keV)	$\Gamma$	C-stat/DOF	APEC Log $L_X$ ( $\text{erg s}^{-1}$ ) 0.3-8 keV	Power Law Log $L_X$ ( $\text{erg s}^{-1}$ ) 0.3-8 keV
A	$0.58 \pm {}^{0.36}_{0.46}$	$0.85 \pm {}^{0.18}_{0.48}$	$1.05 \pm {}^{0.64}_{0.85}$	121.27/178	$41.51 \pm {}^{0.25}_{0.25}$	$41.16 \pm {}^{0.18}_{0.14}$
B	$0.90 \pm {}^{0.38}_{0.5}$	$0.58 \pm {}^{0.35}_{0.21}$	$1.80 \pm {}^{0.71}_{0.6}$	183.60/184	$41.99 \pm {}^{0.3}_{0.51}$	$41.34 \pm {}^{0.31}_{0.3}$
12'' radius	$0.76 \pm {}^{0.21}_{0.26}$	$0.92 \pm {}^{0.13}_{0.58}$	$1.06 \pm {}^{0.78}_{0.91}$	282.91/274	$42.06 \pm {}^{0.14}_{0.21}$	$41.41 \pm {}^{0.37}_{0.13}$

Quoted uncertainties are 90% confidence. The luminosities are unabsorbed.

constrained, and is lower than for Galaxy A. The best-fit  $\Gamma$  for Galaxy B,  $\Gamma = 1.80 \pm {}^{0.71}_{0.60}$ , is consistent with values expected for HMXBs and AGN.

For each of these fits, we provide the unabsorbed thermal and power law 0.3 – 8 keV luminosities in Table 3. In the best fit model for the total spectrum, the APEC component dominates the X-ray luminosity, with  $L_X(0.3 - 8 \text{ keV})$  for the APEC component being about  $4.6 \times$  that from the power law component. For Galaxy A, the intrinsic luminosity for the APEC component is  $2.3 \times$  that of the power law component. For Galaxy B, the absorption-corrected  $L_X(0.3 - 8 \text{ keV})$  for the APEC component is about  $4.6 \times$  larger than that of the power law component.

### 3.5.2. X-ray Spectra of the Smaller X-ray Sources

We also investigated the X-ray spectra of the ten sources identified in the X-ray maps. Table 4 provides coordinates and estimated radii for these sources. For each region, we fit for both an APEC-only model and a power-law-only model, and compared the two fits to determine which model is most appropriate. In Table 4, we provide our fits, including the C-statistic and DOF. Table 4 also gives the unabsorbed luminosity of the APEC or power law spectrum. The fit listed first for each source (in boldface) is our favored fit. The spectra and the best-fit model are displayed in Figures 12, 13, 14, and 15.

For five sources (#1, #2, #4, #5, and #9), we favor the APEC model, because the power-law model gives a photon index larger than typical for AGN or HMXB (i.e.,  $\Gamma > 2.1$ ). For these APEC fits, the temperatures range between kT =  $0.96 \pm {}^{2.72}_{0.38}$  keV for source #2 to  $1.95 \pm {}^{5.85}_{0.77}$  keV for source #1. Source #5 has a relatively large C-stat/DOF ratio and may be variable (see Section 2.4) thus it may have a power law contribution as well. The best-fit values for  $N_H$  for the APEC fits for regions #1, #2, and #9 are significantly larger than the values found from the global fits, and are very poorly constrained. The APEC  $N_H$  values are a factor of 2 – 4 times larger than estimates for their surrounding regions (regions A1, A2, and B3, respectively) from CIGALE. These sources may be highly obscured star-forming regions.

For sources #3 and #8, we prefer the power law model since  $\Gamma < 2$  and the APEC model gives a temperature higher than typical for interstellar gas associated with star formation (i.e., best-fit kT > 5 keV). Source #3 shows some evidence for variability (Figure 4), supporting this interpretation. Sources #6 and #7 have best-fit values of  $\Gamma$  higher than expected for HMXBs or AGN, and the temperatures obtained with an APEC fit are also high. We suggest that the spectra of sources #6 and #7 have contributions from both hot gas and HMXBs. Source #6 shows evidence of variability (Figure 4), consistent with this idea.

For source #10, the apparent nucleus of Galaxy B, a power law model gives a reasonable  $\Gamma$  but a large C-stat/DOF, suggesting a second component. We therefore experimented with more complex models involving two components with different absorptions. We select as our best model one with two APEC components, both with high absorption. A model with a single APEC component gives an unexpectedly large temperature, while an APEC+power law model produces an unphysically-large  $\Gamma$ . The nature of source #10 is discussed further in Section 5.3.

Adding up the APEC luminosities of the best-fit models for the sources in Galaxy A, sources #1, #2, and #4 and half of the luminosity from the bridge source #5, we find  $L_X(\text{gas}) = 1.8 \times 10^{41} \text{ erg s}^{-1}$ , about 54% of the APEC



**Table 4.** Chandra Spectral Results for the X-Ray Sources within IC 2431

X-Ray Source ID	RA (deg)	DEC (deg)	Radius (")	N <sub>H</sub> ( $\times 10^{22}$ cm <sup>-2</sup> )	kT (keV)	$\Gamma$	C-stat/DOF	APEC Log L <sub>X</sub> (erg s <sup>-1</sup> )	Power Law Log L <sub>X</sub> (erg s <sup>-1</sup> )
								0.3-8 keV	0.3-8 keV
#1	136.14752	14.59499	1.7	$1.78 \pm^{2.39}_{1.75}$	$1.95 \pm^{5.85}_{0.77}$	....	28.90/25	$40.69 \pm^{0.49}_{0.32}$	....
#1				$1.09 \pm^{3.45}_{1.09}$	....	$2.29 \pm^{1.78}_{1.13}$	31.48/25	....	$40.7 \pm^{1.32}_{0.38}$
#2	136.14657	14.59378	1.7	$1.82 \pm^{1.47}_{1.82}$	$0.96 \pm^{2.72}_{0.38}$	....	6.39/20	$40.93 \pm^{0.58}_{0.78}$	....
#2				$1.13 \pm^{2.88}_{1.13}$	....	$3.48 \pm^{2.62}_{1.58}$	7.32/20	....	$41.08 \pm^{1.61}_{0.84}$
#3	136.14574	14.59329	1.5	$0.29 \pm^{1.50}_{0.29}$	....	$1.39 \pm^{0.91}_{0.56}$	42.86/50	....	$40.72 \pm^{0.3}_{0.13}$
#3				$0.85 \pm^{1.29}_{0.85}$	$5.11 \pm^{999}_{2.74}$	....	42.41/50	$40.77 \pm^{0.19}_{0.18}$	....
#4	136.14509	14.59290	1.3	$0.0 \pm^{1.27}_0$	$1.64 \pm^{1.56}_{0.77}$	....	6.33/12	$40.1 \pm^{0.58}_{0.21}$	....
#4				$0.035 \pm^{1.63}_{0.035}$	....	$3.06 \pm^{2.40}_{0.99}$	7.85/12	....	$40.46 \pm^{1.61}_{0.37}$
#5	136.14488	14.59385	2.0	$0.79 \pm^{0.84}_{0.79}$	$1.17 \pm^{0.79}_{0.38}$	....	54.21/24	$40.76 \pm^{0.44}_{0.4}$	....
#5				$0.0 \pm^{0.95}_0$	....	$2.76 \pm^{1.24}_{0.65}$	60.42/24	....	$40.7 \pm^{0.77}_{0.21}$
#6	136.14466	14.59569	1.6	$0.0 \pm^{0.22}_0$	....	$2.39 \pm^{0.44}_{0.41}$	45.83/60	....	$40.95 \pm^{0.18}_{0.12}$
#6				$0.0 \pm^{0.27}_0$	$2.80 \pm^{1.76}_{0.81}$	....	49.16/60	$40.8 \pm^{0.06}_{0.09}$	....
#7	136.14412	14.59513	1.2	$0.61 \pm^{1.64}_{0.61}$	....	$2.42 \pm^{1.25}_{0.87}$	44.13/34	....	$40.81 \pm^{0.81}_{0.32}$
#7				$0.013 \pm^{1.35}_{0.013}$	$5.11 \pm^{23.6}_{3.34}$	....	45.78/34	$40.55 \pm^{0.25}_{0.13}$	....
#8	136.14361	14.59463	1.2	$0.0 \pm^{1.81}_0$	....	$1.80 \pm^{1.42}_{0.7}$	19.56/21	....	$40.35 \pm^{0.7}_{0.16}$
#8				$0.0 \pm^{1.06}_0$	$8.68 \pm^{999}_{6.37}$	....	20.24/21	$40.31 \pm^{0.18}_{0.16}$	....
#9	136.14307	14.59408	1.5	$1.24 \pm^{0.74}_{1.24}$	$1.08 \pm^{0.96}_{0.31}$	....	30.20/33	$41.05 \pm^{0.37}_{0.49}$	....
#9				$1.14 \pm^{1.63}_{1.14}$	....	$4.14 \pm^{1.80}_{1.4}$	29.18/33	....	$40.38 \pm^{0.44}_{0.14}$
#10	136.14390	14.59509	1.2	$4.08 \pm^{3.46}_{2.18}/51.1 \pm^{56.3}_{24.9}$	$0.23 \pm^{0.36}_{0.09}/0.73 \pm^{0.55}_{0.37}$	....	47.24/36	$43.08 \pm^{1.41}_{1.53}$	$43.54 \pm^{0.84}_{1.67}$
#10				$0.17 \pm^{1.33}_{0.17}$	....	$1.68 \pm^{0.95}_{0.75}$	62.91/39	....	$40.67 \pm^{0.38}_{0.13}$
#10				$0.0 \pm^{0.82}_{0.0}$	$18.24 \pm^{99.9}_{14.52}$	....	63.4/39	$40.62 \pm^{0.13}_{0.11}$	....
#10				$4.10 \pm^{3.46}_{2.17}/60.35 \pm^{27.85}_{34.4}$	$0.23 \pm^{0.30}_{0.09}$	$8.37 \pm^{99.9}_{5.17}$	48.2/36	$43.1 \pm^{2.09}_{1.57}$	$99.9 \pm^{99.9}_{99.9}$

Quoted uncertainties are 90% confidence. The luminosities are unabsorbed. Source #3 is the presumed nucleus of Galaxy A, while Source #10 is assumed to be the nucleus of Galaxy B.

luminosity we derived for Galaxy A as a whole. Summing the APEC luminosities of the sources in Galaxy B, sources #6, #7, and #9, assuming source #6 and #7 are 50% APEC, 50% power law, and adding half of  $L_X(\text{gas})$  from source #5 gives  $L_X(\text{gas}) = 1.9 \times 10^{41}$  erg s<sup>-1</sup>, about 19% of the APEC luminosity we found for Galaxy B as a whole. Since the region for source #10 overlaps with those of sources #7 and #8, we don't include source #10 in this calculation. The difference between the global values and the sum of the individual regions may be due to diffuse emission outside of our small circular apertures. Summing over all individual sources excluding source #10, we find a total  $L_X(\text{gas}) = 3.7 \times 10^{41}$  erg s<sup>-1</sup>, about 32% of the APEC luminosity within the 12'' radius. In the following analysis, when we compare with other galaxies (Section 4) we will use the global estimates of  $L_X(\text{gas})$  and  $L_{\text{power law}}$  as more representative of the system as a whole.

We estimate the amount of hot gas in each region in IC 2431 using the procedure outlined in [Smith et al. \(2019\)](#) and the cooling functions of [McKee & Cowie \(1977\)](#) and [McCray \(1987\)](#). In Table 5, we provide estimated radii of the concentrations of hot gas and their implied volumes, assuming spherical distributions. We combined these volumes with the absorption-corrected  $L_X(\text{gas})$  and the gas temperature from Table 4 to calculate  $n_e \sqrt{f}$  for each region, where  $n_e$  is the electron density and  $f$  the filling factor. We then use these electron densities and volumes to calculate the mass of the hot X-ray-emitting gas in the region, along with the inferred cooling time (Table 5). Over the entire

system, the total mass of hot gas is about  $5 \times 10^7 M_\odot$ , approximately 1% the mass of neutral hydrogen gas. This excludes possible thermal contributions from regions #6 and #7.

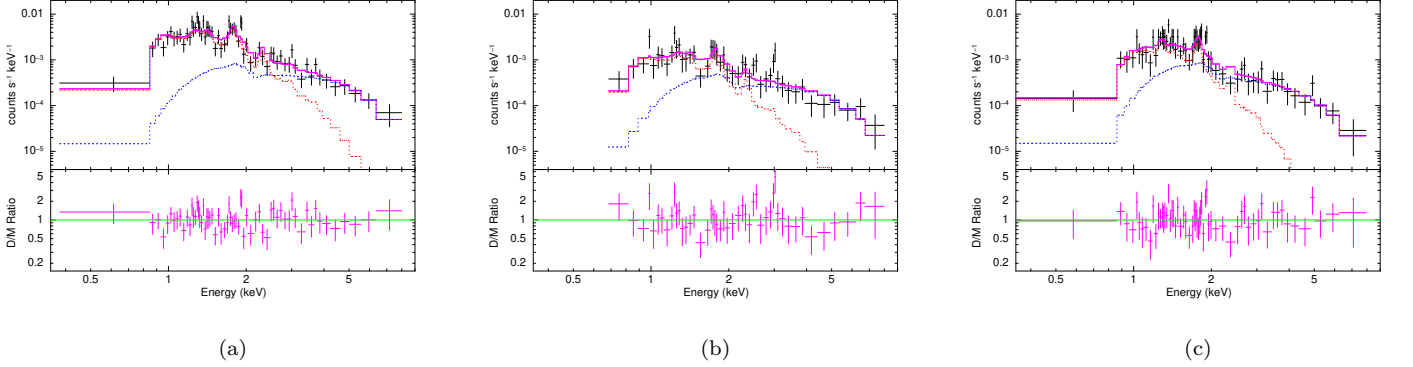


**Figure 11.** Top panels: The Chandra spectra for the diffuse X-ray emission in the IC 2431 group within a 12'' radius (left), Galaxy A (middle) and Galaxy B (right). The best-fit 2-component model is overlaid as a solid magenta curve. The red dotted component dominating at lower energies is the APEC component; the blue dotted dashed component dominating at high energies is the power law component. Bottom panels: the data/model ratio. For plotting purposes only, the spectra for Galaxy A and Galaxy B are rebinned to a minimum of  $S/N = 2$  per bin, and the spectrum for the 12'' radius is rebinned to  $>2.7$  per bin.

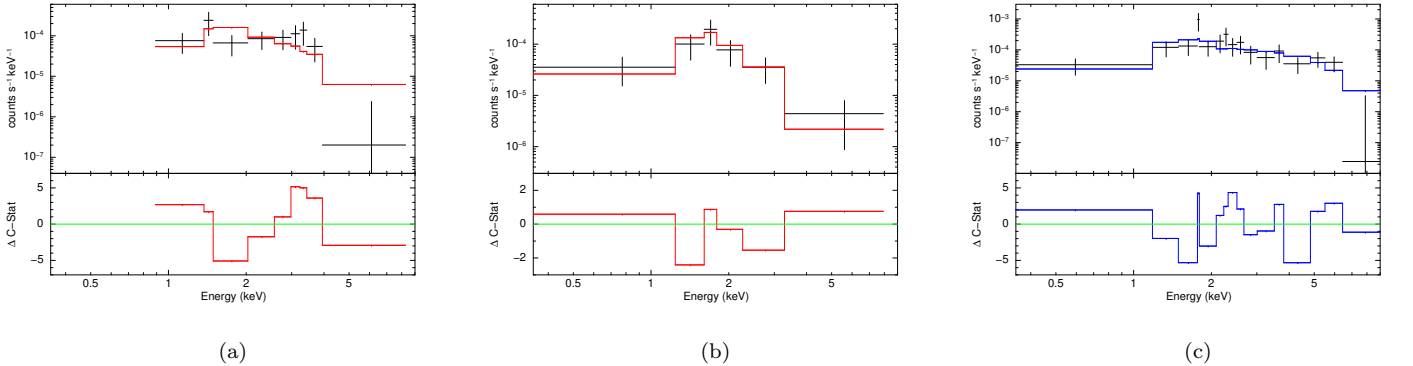


**Figure 12.** Top panels: the Chandra spectra for the diffuse X-ray emission in X-ray source #1 (left), #2 (middle), and #3 (right). The best-fit model is overlaid. The model is plotted in blue when the best-fit model is a power law; the model is in red when the best model is an APEC model. The bottom panel provides  $\Delta C\text{-stat}$ . The data were fitted with C-stat, but were binned to a  $S/N > 1.7$  for plotting purposes.

## 4. COMPARISON WITH OTHER SYSTEMS

### 4.1. Comparison Samples and Available Data

In this section, we compare the Spitzer colors, X-ray properties, star formation rate, stellar mass, morphological types, and atomic gas content of the IC 2431 group to those of other galaxy systems. Our comparison systems include the compact groups studied by Desjardins et al. (2013, 2014), which includes Stephan's Quintet, and the radio-loud group HCG 62, which hosts a radio galaxy (Gitti et al. 2010; O'Sullivan et al. 2011). We also compare to a set of 49 equal-mass merging pairs of galaxies in various merger stages (Smith et al. 2018, 2019), and the Spitzer Infrared Nearby Galaxies Survey (SINGS) (Kennicutt et al. 2003) sample of nearby spirals, irregulars, and ellipticals. In addition, we

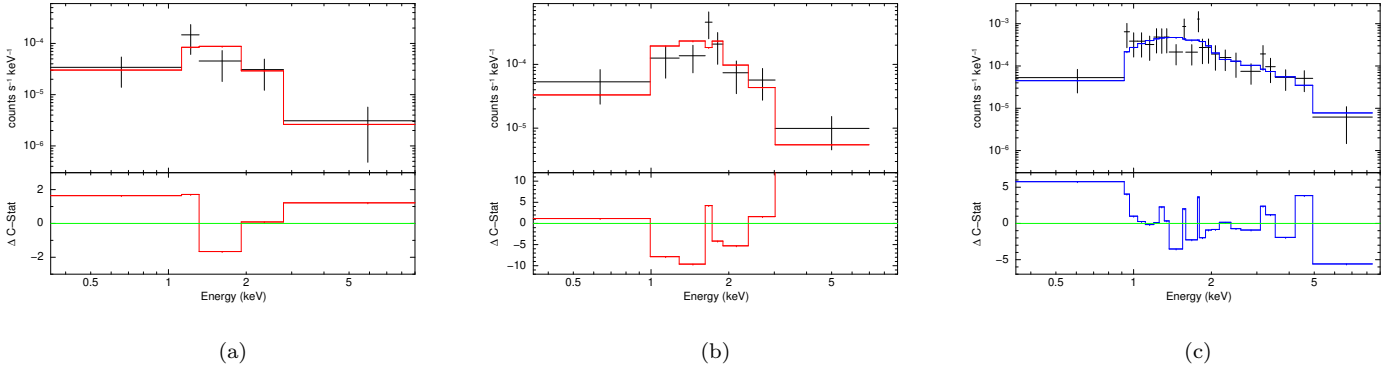


**Figure 13.** Top panels: The Chandra spectra for the diffuse X-ray emission in X-ray source #4 (left), #5 (middle), and #6 (right). The best-fit model is overlaid. The model is plotted in blue when the best-fit model is a power law; the model is in red when the best model is an APEC model. The bottom panel provides  $\Delta$  C-stat. The data were fitted with C-stat, but were binned to a  $S/N > 1.7$  for plotting purposes.

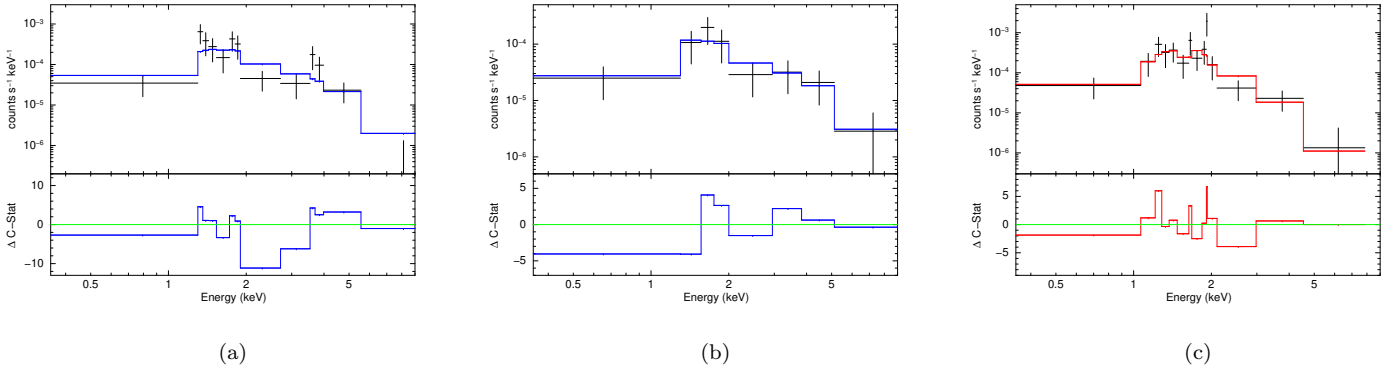


**Figure 14.** Top panels: The Chandra spectra for the diffuse X-ray emission in X-ray source #7 (left), #8 (middle), and #9 (right). The best-fit model is overlaid. The model is plotted in blue when the best-fit model is a power law; the model is in red when the best model is an APEC model. The bottom panel provides  $\Delta$  C-stat. The data were fitted with C-stat, but were binned to a  $S/N > 1.7$  for plotting purposes.

compare with the Taffy galaxy pair, the radio-loud galaxy group NGC 4410, the Cartwheel collisional ring galaxy, and the Taffy-like system HCG 57.

For the compact groups, we utilize hot gas luminosities from Desjardins et al. (2013, 2014), after converting to the 0.3 – 8 keV energy range using the PIMMS software<sup>13</sup>. We use the summed 0.5 – 8 keV luminosities of the point sources in these groups, from Tzanavaris et al. (2016). We use UV/IR-based SFRs for the compact groups from Lenkić et al. (2016), after adjusting to a Kroupa IMF as in Kennicutt & Evans (2012). For the compact groups, we use stellar masses from Lenkić et al. (2016), atomic hydrogen masses from Desjardins et al. (2013, 2014), and Spitzer IR colors from Cluver et al. (2013). For the galaxies in Stephan’s Quintet and for two intergalactic regions in SQ with strong shock emission, we measured Spitzer IRAC fluxes from archival data. Morphological types for the compact group galaxies are available from Desjardins et al. (2013) and Jones et al. (2023). Two of these groups host known X-ray AGN (Tzanavaris et al. 2016).

For the mergers, we use the Smith et al. (2018) absorption-corrected  $L_X(\text{gas})$  and  $L_X(\text{power law})$  values, obtained using spectral decomposition after point-source subtraction. We use version 2.1 of the Chandra Source Catalog (CSC)

<sup>13</sup> Portable, Interactive Multi-Mission Simulator; <https://cxc.harvard.edu/toolkit/pimms.jsp>



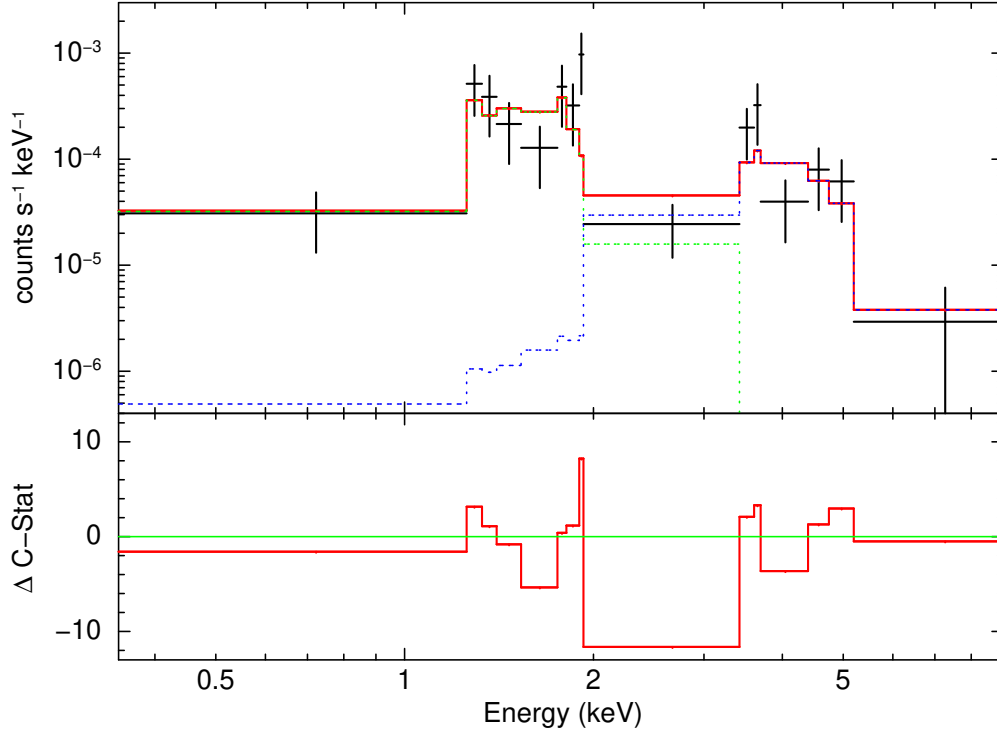


**Figure 15.** Top panel: The Chandra spectra for the diffuse X-ray emission in X-ray source #10. The best-fit model, a model with two APEC components, is overlaid. The two APEC components are shown dotted in blue and green. The bottom panel provides  $\Delta$  C-stat. The data were fitted with C-stat, but were binned to a  $S/N > 1.7$  for plotting purposes.

**Table 5.** Derived Properties of the Hot Gas in IC 2431

X-Ray	Assumed	Volume	$n_e \sqrt{f}$	Log	Cooling
Source	Radius	(kpc <sup>3</sup> )	(cm <sup>-3</sup> )	Hot	Time
ID	( $''$ )			Gas	(Myrs)
				Mass	
				( $M_\odot$ )	
#1	0.7	1.44	0.22	6.88	29.4
#2	0.7	1.44	0.25	6.93	9.4
#4	0.75	1.77	0.1	6.62	51.4
#5	1.25	8.18	0.09	7.25	34.7
#9	0.7	1.44	0.29	7	9.6
Total		14.27		7.68	

(Evans et al. 2024) to make a list of all of the X-ray point sources within the D25 radius of the mergers, and sum

their X-ray luminosities. We use UV/IR-based SFRs for the mergers from [Smith et al. \(2018\)](#), HI and H<sub>2</sub> masses as compiled by [Smith et al. \(2019\)](#), and Spitzer infrared fluxes extracted as in [Smith et al. \(2018\)](#). We derived sSFRs for the mergers using stellar masses calculated from the Spitzer 3.6  $\mu\text{m}$  and 4.5  $\mu\text{m}$  fluxes using the method of [Watkins et al. \(2022\)](#). Ten of these mergers have a known Seyfert nucleus, according to classifications compiled by [Smith et al. \(2018\)](#). Note that the merger sample was specifically selected to exclude radio AGN ([Smith et al. 2018](#)).

For the SINGS galaxies, we use the X-ray measurements of [Lehmer et al. \(2019\)](#) and the Spitzer fluxes of [Dale et al. \(2017\)](#). For the Taffy pair, we use the X-ray properties, SFR, and stellar mass from [Appleton et al. \(2015\)](#), the HI mass from [Condon et al. \(1993\)](#), and Spitzer fluxes extracted from archival images. For NGC 4410, we use the Chandra results of [Smith et al. \(2003\)](#), the HI data from [Smith \(2000\)](#), the star formation rate from [Donahue et al. \(2002\)](#), the morphological types tabulated in [Smith \(2000\)](#), and derive stellar masses from the WISE data using the relation from [Watkins et al. \(2022\)](#). For the Cartwheel galaxy, we use the SFR from [Mayya et al. \(2005\)](#), the stellar mass from [Zaragoza-Cardiel et al. \(2022\)](#), the HI mass from [Higdon \(1996\)](#), L<sub>X</sub>(gas) from [Wolter & Trinchieri \(2004\)](#) and [Crivellari et al. \(2009\)](#), and L<sub>X</sub> from the point sources plus the diffuse power law component from [Wolter & Trinchieri \(2004\)](#). For the compact group HCG 57, we obtain morphological types and Chandra L<sub>X</sub>(gas) measurements from [O’Sullivan et al. \(2025\)](#), and the HI mass from [Verdes-Montenegro et al. \(2001\)](#).

#### 4.2. Spitzer IR Colors

In Figure 16, we plot  $\log(F_{8.0}/F_{4.5})$  vs.  $\log(F_{5.8}/F_{3.6})$  for the various regions in IC 2431 and the comparison samples, where  $F_{3.6}$ ,  $F_{4.5}$ ,  $F_{5.8}$ , and  $F_{8.0}$  are the Spitzer flux densities at 3.6, 4.5, 5.8, and 8.0  $\mu\text{m}$ , respectively. These flux densities have been K-corrected to account for the shifting of PAH features relative to the Spitzer broadband filters. The K-corrections were calculated using the [Blanton & Roweis \(2007\)](#) `kcorrect`<sup>14</sup> software using a large set of infrared galaxy templates from [Pai et al. \(2024\)](#). At the redshift of IC 2431 with a starburst spectrum, the K-correction in the 8  $\mu\text{m}$  filter is small, so our 8  $\mu\text{m}$ -based SFR calculations are not strongly affected; the largest K-correction is in the 5.8  $\mu\text{m}$  filter, causing a shift of about 0.45 dex to the right in Figure 16.

Galaxies in the upper right of Figure 16 tend to be star-forming, while galaxies in the lower left are quiescent ([Sajina et al. 2005](#)). In Figure 16, we have marked in red the region in which powerful AGN are expected to fall, according to [Lacy et al. \(2004\)](#). The galaxies in our sample known to host optical AGNs (marked with black diamonds) lie in or near this region. The dotted box marks the ‘gap’ region, as defined by [Cluver et al. \(2013\)](#), which hosts relatively few compact group galaxies. The ‘gap’ region is thought to be a transition region; galaxies in compact groups apparently evolve quickly through this part of the Spitzer color-color plot ([Walker et al. 2010](#)). Galaxies above the ‘gap’ region are actively forming stars, while galaxies below the ‘gap’ are quenched.

In IC 2431, Galaxy B as a whole is particularly red in these Spitzer colors, as are the two southern regions in Galaxy B (regions B2 and B3), and the two northern regions in Galaxy A (regions A1 and A2). These regions are therefore very strongly star-forming. However, the other regions in Galaxy A and Galaxy B (regions A3, A4, and B3) also lie in the star-forming zone in this plot, as does Galaxy A as a whole. In contrast, Galaxy C sits on the upper boundary of the gap region.

In Figure 16, we have identified the compact group galaxies classified by [Cluver et al. \(2013\)](#) as ‘Molecular Hydrogen Emission-Line Galaxies’ (MOHEG), based on the strength of the mid-IR H<sub>2</sub> lines relative to the PAH features. For these galaxies, the H<sub>2</sub> lines appear excited above that expected by UV heating ([Cluver et al. 2013](#)). As noted by [Cluver et al. \(2013\)](#), the MOHEG galaxies tend to lie in or near the ‘gap’. In Figure 16, we have marked locations of shocked IGM in Stephan’s Quintet; these regions lie at the top of the dotted box, while the SQ galaxies themselves lie at the bottom of the dotted box or below, in the quenched region. The galaxies in the radio-loud group HCG 62 also sit near the bottom left of the plot. In contrast, the two Taffy galaxies have Spitzer IRAC colors similar to those of the galaxies in IC 2431, thus are star-forming.

#### 4.3. Absorbing Column Density

The large values of L<sub>X</sub>(thermal) that we derive for Galaxy A and Galaxy B are a consequence of the relatively high absorbing columns ( $6 \times 10^{21} \text{ cm}^{-2}$  and  $9 \times 10^{21} \text{ cm}^{-2}$ , respectively) implied by the X-ray spectrum. For the galaxies in the merger comparison sample, the highest N<sub>H</sub> values inferred from the UV/IR ratios and obtained from fitting Chandra X-ray spectra are  $4 - 7 \times 10^{21} \text{ cm}^{-2}$  ([Smith et al. 2018](#)). For the SINGS galaxies, the median inferred

<sup>14</sup> <https://kcorrect.readthedocs.io/>

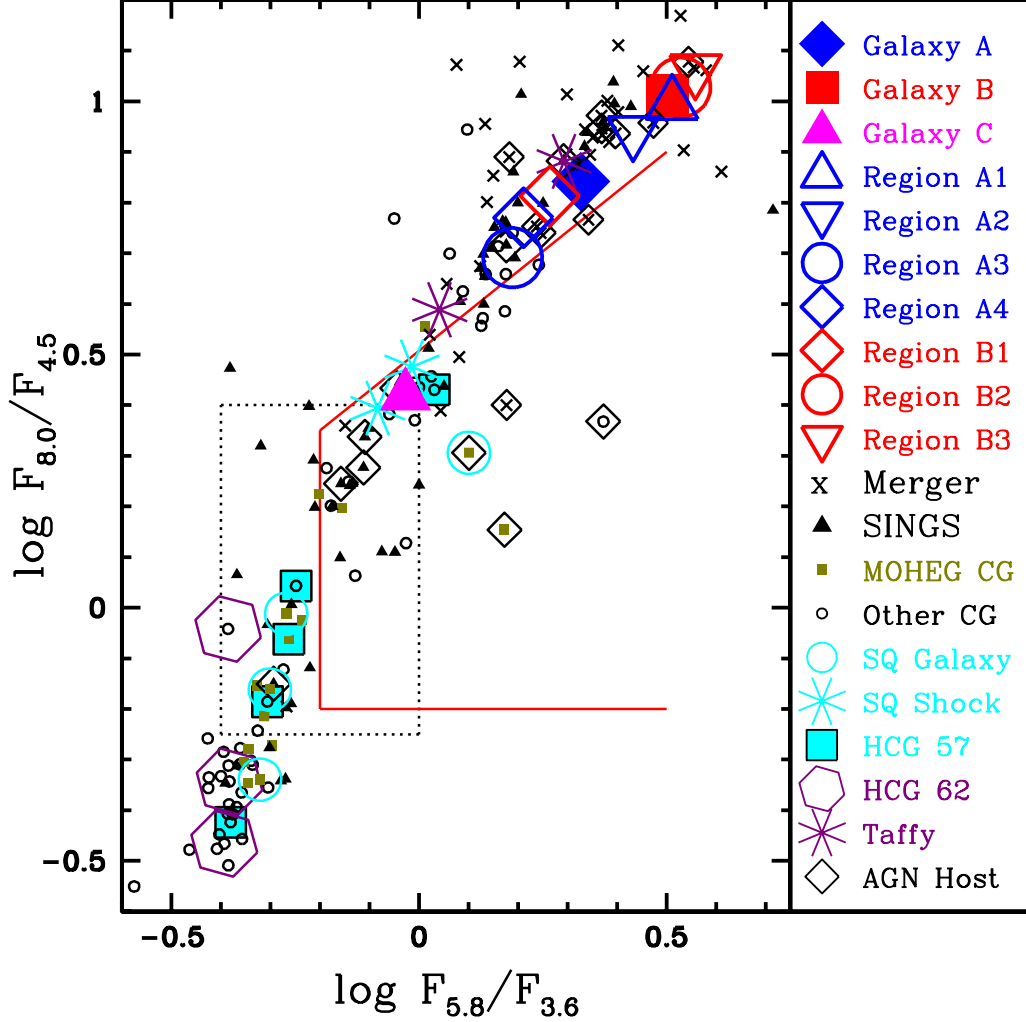


**Figure 16.**  $\log (F_{8.0}/F_{4.5})$  vs.  $\log (F_{5.8}/F_{3.6})$  for the regions in IC 2431, and the comparison galaxies. The colors have been K-corrected as described in the text. As indicated by the legend on the right, Galaxy A is a filled blue diamond, Galaxy B a filled red square, and Galaxy C a filled magenta triangle. Subregions within each galaxy are plotted as open symbols with the same color as the galaxy as a whole. Merging pairs are plotted as black crosses and SINGS galaxies as black filled triangles. The small olive squares are compact group galaxies classified as MOHEG, while black open circles are other compact groups. Galaxies in Stephan’s Quintet (HCG 92) are marked with cyan circles, and two locations in the intergalactic shock in SQ are marked by cyan asterisks. Galaxies in the Taffy-like system HCG 57 are marked by filled cyan squares outlined in black. The large open purple hexagons mark galaxies in the compact group HCG 62, which hosts a radio galaxy. The purple asterisks show the two galaxies in the Taffy pair, using archival data (UGC 12915 is the redder galaxy). Galaxies known to host an optical AGN are marked with open black diamonds. The region marked in red is where AGNs are expected to lie, according to [Lacy et al. \(2004\)](#); the known optical AGNs are mostly in or near this region. The dotted box shows the ‘gap’ region defined by [Cluver et al. \(2013\)](#) (see text for details).

$N_{\text{H}}(\text{internal})$  from Chandra data is  $2 \times 10^{21} \text{ cm}^{-2}$ , with a 75th percentile of  $6 \times 10^{21} \text{ cm}^{-2}$  [Lehmer et al. \(2019\)](#). Thus the absorbing columns for IC 2431 are quite high compared to most other galaxies.

#### 4.4. Hot Gas vs. Star Formation Rate in IC 2431 vs. Other Galaxies

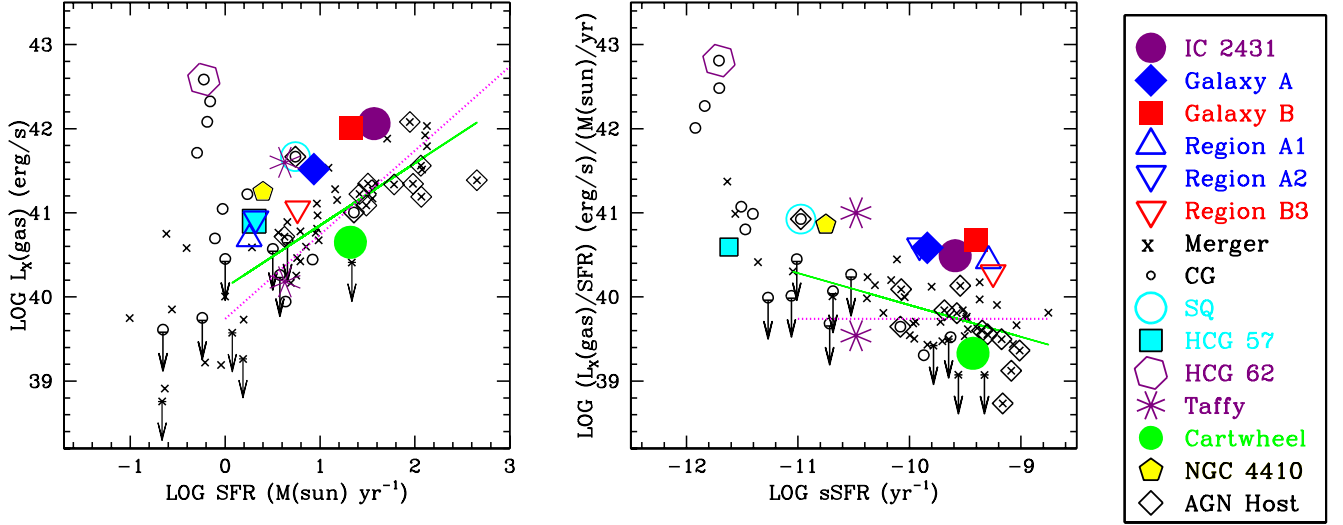


**Figure 17.** Left: The X-ray luminosity from hot gas plotted against the SFR. Right: The ratio  $L_{\text{X}}(\text{gas})/\text{SFR}$  vs. sSFR. The purple filled circle marks the location of IC 2431 as a whole. The blue filled diamond is Galaxy A, and the red filled square is Galaxy B. The three APEC-dominated sub-regions in IC 2431 are open symbols as given in the legend on the right. The black crosses are the merging pairs. The black open circles are the compact groups. Stephan’s Quintet (HCG 92) is marked as an open cyan circle, and the possible Taffy system HCG 57 is identified by a filled cyan square outlined in black. The purple open hexagon is HCG 62, which hosts a radio galaxy. The purple asterisks show limiting cases for the Taffy pair as a whole, using data from [Appleton et al. \(2015\)](#); the lower value was obtained using a X-ray spectral model with both a power law and thermal component, with no internal absorption, while the upper value comes from a model with only an absorbed thermal component. The green filled circle marks the Cartwheel galaxy. The yellow pentagon outlined in black is NGC 4410. Systems hosting a known optical AGN are marked with open black diamonds. The dotted magenta line marks the median value of  $L_{\text{X}}(\text{gas})/\text{SFR} = 5.5 \times 10^{39} \text{ (erg s}^{-1})/(\text{M}_{\odot} \text{ yr}^{-1})$  for the mergers with  $\text{SFR} \geq 1 \text{ M}_{\odot} \text{ yr}^{-1}$ . The green solid line is the best-fit line for the mergers with  $\text{SFR} \geq 1 \text{ M}_{\odot} \text{ yr}^{-1}$ .

In the left panel of Figure 17, we plot  $L_{\text{X}}(\text{gas})$  vs SFR for our comparison samples, and IC 2431 as a whole and Galaxy A and B separately. The right panel of Figure 17 shows  $L_{\text{X}}(\text{gas})/\text{SFR}$  vs. sSFR. In Figure 17, we also mark the three sub-regions in IC 2431 whose X-ray spectra are dominated by APEC emission: region A1 (X-ray source #1), region A2 (X-ray source #2), and region B3 (X-ray source #9). On these plots, we overlay two lines, one marking the median value of  $L_{\text{X}}(\text{gas})/\text{SFR}$  for the mergers, and the other showing the best-fit relation for the mergers. For these lines, only mergers with  $\text{SFR} \geq 1 \text{ M}_{\odot} \text{ yr}^{-1}$  are included. IC 2431 as a whole lies above these lines, as do Galaxy A and Galaxy B individually, particularly Galaxy B. For the  $\text{SFR} > 1 \text{ M}_{\odot} \text{ yr}^{-1}$  mergers, the median absorption-corrected  $L_{\text{X}}(\text{gas})/\text{SFR}$  is  $5.5 \times 10^{39} \text{ (erg s}^{-1})/(\text{M}_{\odot} \text{ yr}^{-1})$  ([Smith et al. 2018](#)). The observed  $L_{\text{X}}(\text{gas})/\text{SFR}$  for IC 2431 as a whole from Chandra is approximately  $2 \times 10^{40} \text{ (erg s}^{-1})/(\text{M}_{\odot} \text{ yr}^{-1})$ , about four times higher than the median value for the merging galaxies. The scatter for the mergers is large, however (about a factor of 2.3 in  $L_{\text{X}}(\text{gas})/\text{SFR}$ ), so IC 2431 as a whole does not stand out in Figure 17. Galaxy B individually, however, is exceptional in its amount of hot gas. Depending upon whether the CIGALE or FUV+ $8\mu\text{m}$  SFR is used, the  $L_{\text{X}}(\text{gas})/\text{SFR}$  for Galaxy B is  $4 - 5 \times 10^{40} \text{ (erg s}^{-1})/(\text{M}_{\odot} \text{ yr}^{-1})$ , a factor of 9 times larger than the median value of the mergers. The three sub-regions in IC 2431 whose X-ray spectra are well-fit by a APEC function (A1, A2, and B3) all lie above the best-fit line for the mergers, particularly region A2, which is associated with the dust lane.



In the  $L_X(\text{gas})$  vs. SFR plot, the IC 2431 group as a whole lies close to Arp 236 (VV 114; IC 1623), a pair of disk galaxies in close contact. James Webb Space Telescope (JWST) observations of Arp 236 reveal a very dust-enshrouded core,  $\text{H}_2$  and  $[\text{Fe II}]$  shock lines, but no high ionization lines indicative of an AGN (Donnan et al. 2023). Four other merging systems lie  $\sim 0.5$  dex to the right of IC 2431 with similar  $L_X(\text{gas})$  values but SFRs three times higher. In order from highest  $L_X$ , these four galaxies are NGC 6240, IRAS 17208-0014, AM 2055-425 (IRAS 20551-4250), and AM 2312-591 (IRAS 23128-5919). Of these four systems, only NGC 6240 has a known Seyfert nucleus, although star formation appears to dominate its infrared luminosity (Armus et al. 2006). All of these four galaxies except AM 2312-591 have strong mid-IR  $\text{H}_2$  lines (Petric et al. 2018).

The optically-identified AGNs among the mergers tend to have high SFRs, and lower  $L_X(\text{gas})$  for their SFRs, compared to mergers not identified as AGN (see Figure 17). One possible explanation for the lower  $L_X(\text{gas})/\text{SFR}$  for the AGNs is that the SFRs in these galaxies may be over-estimated because of contributions to the UV and IR from the AGN (Smith et al. 2018). In any case, the optical AGNs are not over-luminous in hot gas, and, except for NGC 6240, do not lie close to IC 2431 in Figure 17.

In Figure 17, we also compare with the Desjardins et al. (2013, 2014) compact groups. For SFRs  $\geq 1 \text{ M}_\odot \text{ yr}^{-1}$ , the compact groups agree reasonably well with the mergers. At SFRs  $< 1 \text{ M}_\odot \text{ yr}^{-1}$ , some of the compact groups show large excesses relative to the  $L_X(\text{gas})/\text{SFR}$  ratio for the high SFR mergers. The group with the highest  $L_X(\text{gas})$  is HCG 62, which hosts a radio galaxy (Gitti et al. 2010; O’Sullivan et al. 2011). Stephan’s Quintet (HCG 92) and NGC 4410 also show elevated  $L_X(\text{gas})/\text{SFR}$  ratios compared to mergers with similar SFRs. Figure 17 includes two limiting cases for the Taffy galaxies, using data from Appleton et al. (2015). In the extreme case of an absorbed thermal spectrum with no power law component, the Taffy lies close to Stephan’s Quintet in Figure 17. At the other extreme (a composite power law plus thermal spectrum with no internal absorption), the Taffy system has a modest  $L_X(\text{gas})$  for its SFR, near the bottom of the range for its SFR compared to the mergers.

For both the compact groups and the mergers,  $L_X(\text{gas})/\text{SFR}$  is anti-correlated with sSFR (right panel, Figure 17). Systems with high  $L_X(\text{gas})/\text{SFR}$  tend to have low sSFR. The compact groups tend to follow the same trend as the mergers, but extend to lower sSFRs and higher  $L_X(\text{gas})/\text{SFR}$ s. As the galaxies in a group or merging pair quench and the sSFR drops, the amount of hot gas relative to the SFR increases. This trend is visible even for strongly star-forming galaxies ( $\log \text{sSFR} > -11$ ). Relative to this trend, IC 2431 stands out as having a high  $L_X/\text{SFR}$ , particularly Galaxy B, which is about 1 dex above the trend. Galaxy A and sub-regions A1, A2, and B3 are also enhanced in hot gas, lying 0.8 dex above the best-fit relation for the mergers.

Stephan’s Quintet and NGC 4410, which have lower sSFRs than IC 2431, have hot gas excesses of about 0.6 dex relative to this trend. HCG 62, a group with a radio AGN, has the highest  $L_X(\text{gas})/\text{SFR}$ s in the sample. It is notable that the three systems in this sample with apparent radio AGNs (IC 2431, NGC 4410, and HCG 62) all show excess hot gas relative to their SFRs. We note, however, that the excess hot gas in IC 2431 is not only in the vicinity of the radio jet, but also in the far north of Galaxy A and within Galaxy B.

#### 4.5. Morphology and HI Content

Another tracer of the evolutionary stage of a compact group is the fraction of non-dwarf galaxies which are elliptical or S0. This is plotted against sSFR in the left panel of Figure 18 for the compact groups and IC 2431. In making this plot, we assumed that all three of the galaxies in IC 2431 are spirals. The compact groups show an anti-correlation; groups with high fractions of E/S0 galaxies have low sSFRs. IC 2431 is in the bottom right of the plot, consistent with the trend seen in the other compact groups, but with a higher sSFR. The radio-loud group HCG 62 is at the other extreme, with very low sSFR and all E/S0 galaxies. Stephan’s Quintet is not unusual in this plot; it lies in the middle of the range for the compact groups, with about half of the galaxies identified as E/S0, and a moderate sSFR.

In the right panel of Figure 18, we plot  $L_X(\text{gas})/\text{SFR}$  for the compact groups and IC 2431 against the fraction of galaxies that are E/S0. As the fraction of early-type galaxies in a compact group increases, the  $L_X(\text{gas})/\text{SFR}$  of the group tends to increase. HCG 62 is at the upper right of the plot, with large  $L_X(\text{gas})/\text{SFR}$  and all E/S0 morphologies. IC 2431 has a relatively high  $L_X(\text{gas})/\text{SFR}$  ratio, compared to other compact groups containing no E or S0 galaxies. One possibility is that Galaxy A in the process of transforming from a spiral to an S0 galaxy via ram pressure stripping. The lack of star formation south of the nucleus of Galaxy A may support this idea. It is also possible that Galaxy C, which is more quenched than the other two galaxies, is an S0 rather than spiral galaxy.

Another proxy of the evolutionary stage of a compact group is the fraction of the baryons that are in the form of atomic interstellar hydrogen gas,  $f_{\text{b,HI}}$ , defined by Desjardins et al. (2014) to be the ratio of the HI mass to the sum

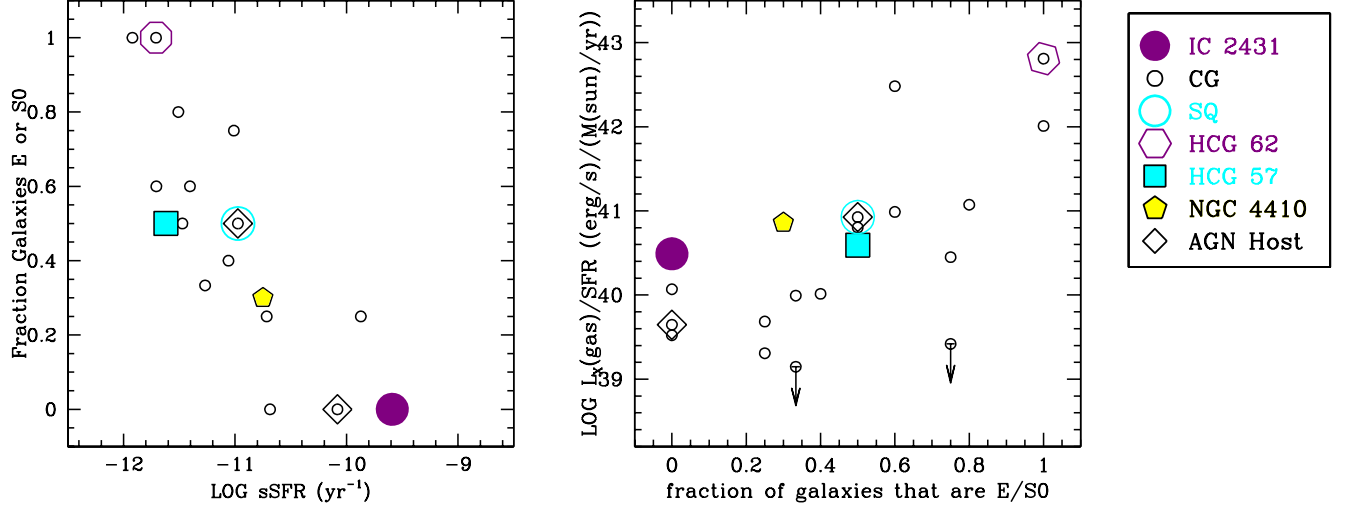


**Figure 18.** Left: The fraction of non-dwarf galaxies that are elliptical or S0, plotted against the sSFR. Right: The  $L_X(\text{gas})/\text{SFR}$  ratio plotted against the fraction of non-dwarf galaxies that are elliptical or S0. The purple filled circle marks the location of IC 2431. The black open circles are the compact groups. Stephan’s Quintet (HCG 92) is marked by a cyan circle. The large open purple hexagon marks HCG 62, which hosts a radio galaxy. The Taffy-like system HCG 57 is marked by a filled cyan square outlined in black. The yellow pentagon outlined in black is NGC 4410. Known optical AGN are identified by black open diamonds.

of the stellar mass plus the HI mass (ignoring molecular gas). This quantity is plotted with sSFR in the left panel of Figure 19. This plot includes the mergers as well as the compact groups and IC 2431. A strong correlation is seen for the compact groups, in that galaxies with proportionally more HI gas have higher sSFRs. The radio loud system HCG 62 is at the lower left in this plot, with low sSFR and low HI content. Stephan’s Quintet is in the middle of the range for the compact groups and is consistent with the trend seen in the other compact groups. The Taffy galaxies and NGC 4410 also follow the same relation as the compact groups.

Most of the mergers follow this same trend of increasing  $f_{b,\text{HI}}$  with increasing sSFR, however, there are some with high sSFRs but only moderate values of  $f_{b,\text{HI}}$ . We have confirmed that these discrepant mergers tend to have large quantities of interstellar molecular gas. In Figure 19, we identify mergers with  $\text{H}_2$  masses greater than the HI mass, using published 2.6 mm CO observations compiled by Smith et al. (2019). IC 2431 lies above the trend for the compact groups, but is not as discrepant as some of the mergers. IC 2431 has proportionally much more HI than Stephan’s Quintet as well as a much higher sSFR. The location of IC 2431 on this plot suggests that, like some of the mergers, it may be rich in molecular gas. It has not yet been observed in CO.

In the right panel of Figure 19,  $L_X(\text{gas})/\text{SFR}$  is plotted with the fraction of baryons in HI, including both the compact groups and the mergers. As the fraction of the baryons in atomic hydrogen gas decreases, the  $L_X(\text{gas})/\text{SFR}$  ratio tends to increase. The IC 2431 group has a  $L_X(\text{gas})/\text{SFR}$  ratio and a sSFR comparable to mergers and other compact groups with similar fractional amounts of atomic gas.

Based on its high HI mass relative to its stellar mass, its high sSFR, and its low fraction of E/S0 galaxies, the IC 2431 group would be classified as being in an early stage of evolution. According to Desjardins et al. (2013), as the fraction of E/S0 galaxies in a compact group increases and both the HI content and star formation rate decrease, more of the hot gas is found outside of the main bodies of the galaxies. In IC 2431, with the exception of the bridge gas we find little extended diffuse X-ray emission outside of the disks of the galaxies. This is consistent with the status of IC 2431 as a relatively early-stage group merger.

#### 4.6. The Power Law Component of the X-Ray Spectrum

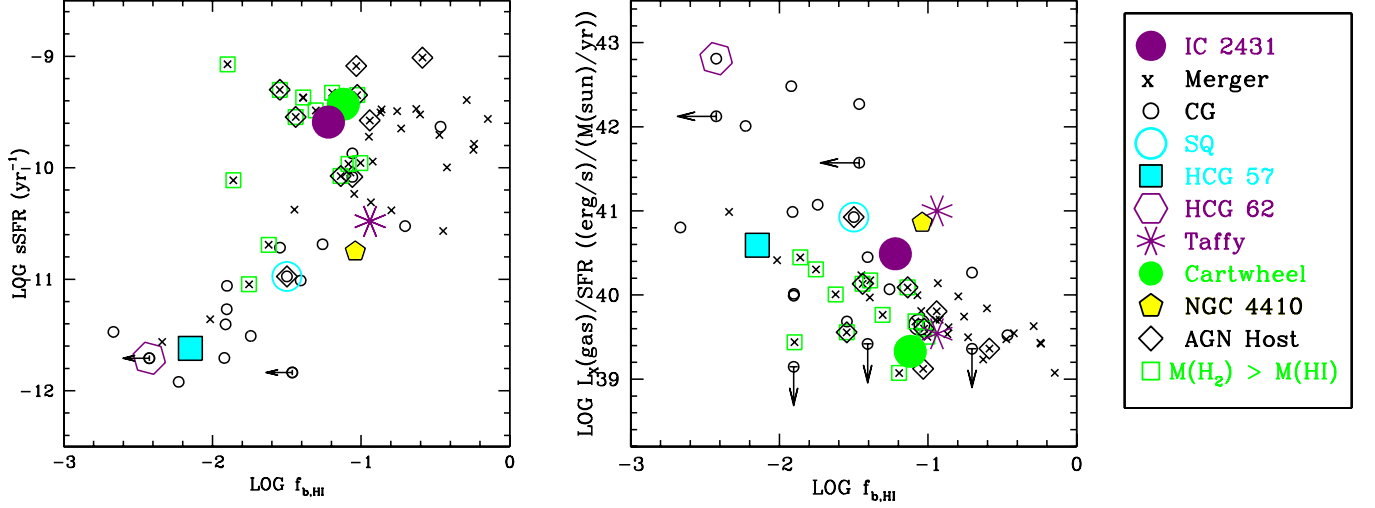


**Figure 19.** Left: The sSFR plotted against  $f_{b,HI}$ , the fraction of baryons that are HI, defined as the ratio of the HI mass to the sum of the mass of stars plus HI gas (ignoring molecular gas). Right:  $L_X(\text{gas})/\text{SFR}$  vs.  $\log f_{b,HI}$ . Symbols are defined in the legend on the right. The purple filled circle marks the location of IC 2431. The black crosses are the merging pairs. The black open circles are the compact groups. Stephan’s Quintet (HCG 92) is marked as an open cyan circle. HCG 57 is marked by a filled cyan square outlined in black. The open purple hexagon marks HCG 62, which hosts a radio galaxy. The purple asterisks give the limiting cases for the Taffy galaxies. The green filled circle marks the Cartwheel galaxy. The yellow pentagon outlined in black is NGC 4410. Known optical AGNs are identified by black open diamonds. Open green squares mark mergers with  $M(H_2) > M(HI)$ .

From spectral analysis of the Chandra data we find an absorption-corrected  $L_X(\text{power law}) = 3 \times 10^{41} \text{ erg s}^{-1}$  for the IC 2431 group as a whole. Outside of the galactic nuclei, most of this radiation likely originates from an unresolved population of HMXBs associated with the starburst. In non-AGN star forming galaxies, HMXB emission dominates the power law component in the X-ray (Grimm et al. 2003; Mineo et al. 2012b).

In the left panel of Figure 20, we plot  $L_X(\text{power law})$  vs. the SFR for IC 2431 and the comparison samples. The right panel of Figure 20 shows  $L_X(\text{power law})/\text{SFR}$  vs. sSFR. For the mergers, we have included both the unresolved power law component as seen by Chandra (Smith et al. 2018), as well as the sum of the luminosities of the X-ray point sources in the CSC, added to the unresolved power law component. For the compact groups and the SINGS galaxies, we only plot the sum of the luminosities of the X-ray point sources as tallied by Tzanavaris et al. (2016) and Lehmer et al. (2019), respectively.

For the full set of galaxies, a clear anti-correlation is seen between  $L_X(\text{power law})/\text{SFR}$  and sSFR. Galaxies with low sSFR have higher  $L_X(\text{power law})/\text{SFR}$ , probably because of contributions from LMXBs to the power law emission. High sSFR mergers tend to have low  $L_X(\text{power law})/\text{SFR}$  ratios, compared to galaxies with moderate sSFRs, although in both cases HMXBs likely dominate the power law emission. Three factors may contribute to the low ratios in the high sSFR mergers: 1) obscured AGN may contribute to the UV/IR fluxes, causing the SFRs to be over-estimated, 2) the extinction has been under-estimated. or 3) these systems may have young stellar ages, thus there may not have been enough time for a large population of HMXBs to form.

In contrast to the extreme starbursts in the merger sample, IC 2431 as a whole and Galaxy B individually have  $L_X(\text{power law})/\text{SFR}$  ratios close to the best-fit value for the HMXB component for the SINGS galaxies and to the relation for the mergers. The power-law emission from Galaxy A is enhanced by about a factor of four relative to the SINGS median value, but is only slightly high (a factor of about 1.6) relative to the best-fit relation for the mergers. This excess may be due to contributions from an AGN, although most of the mergers in Figure 20 known to have AGNs don’t show excesses in their power-law X-ray emission.

In contrast to IC 2431, Stephan’s Quintet stands out in Figure 20 as having a high  $L_X(\text{power law})/\text{SFR}$  for its sSFR. The vast majority of this excess emission is from the Seyfert 2 galaxy NGC 7319; without that galaxy, the  $L_X(\text{power law})$  for Stephan’s Quintet would be only  $10^{41}$  erg s $^{-1}$ , closer to the other systems in Figure 20 with similar SFRs. The radio galaxy HCG 62 does not show a strong excess in power law emission, when compared to its SFR.

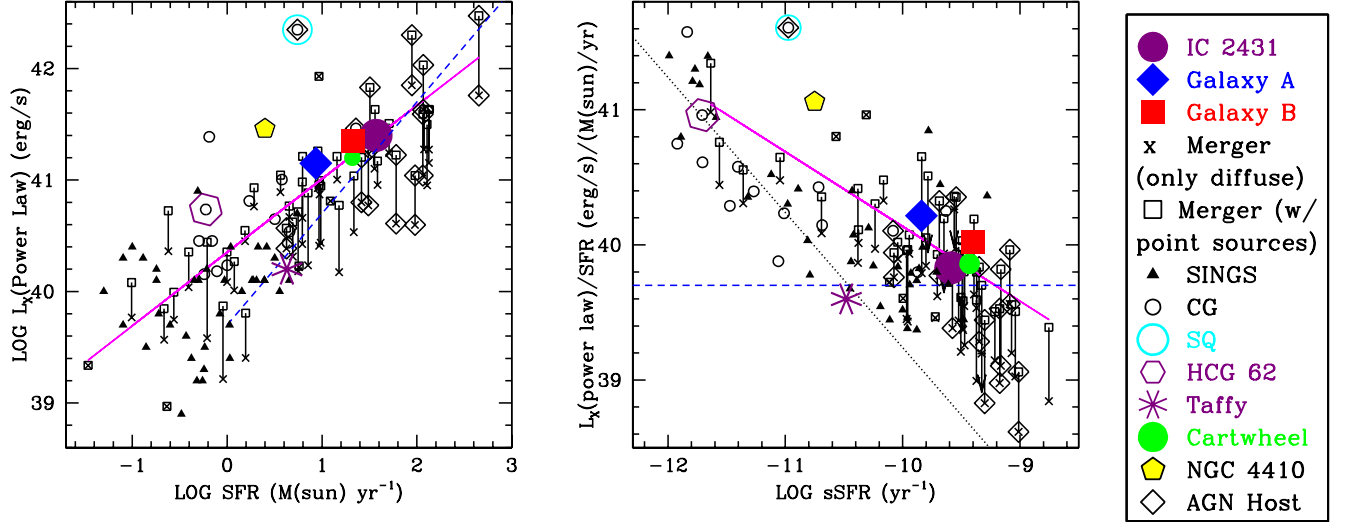


**Figure 20.** Left: The power law component of the X-ray luminosity plotted against the SFR. Right: The ratio  $L_X(\text{power law})/\text{SFR}$  vs. sSFR. The symbols are explained in the legend on the right. The purple filled circle marks the location of IC 2431 as a whole. The filled blue diamond is Galaxy A and the filled red square is Galaxy B. Each pair in the merging galaxy sample is marked by two datapoints: the black crosses give the power law component of only the diffuse emission for the mergers, while the black open squares give the diffuse power law component added to the sum of the resolved point sources. The black filled triangles mark the sum of the X-ray luminosities of the point sources in the SINGS galaxies. The black open circles are the compact groups. Stephan’s Quintet is marked as a cyan circle. HCG 62 is plotted as an open magenta hexagon. The Taffy pair is marked by a purple asterisk. The green filled circle marks the Cartwheel galaxy. The yellow pentagon outlined in black is NGC 4410. The black open diamonds mark known optical AGN. The magenta solid line is the best-fit line for the mergers after adding the resolved point sources to the power law component of the diffuse emission:  $\log(L_X(\text{PL})/\text{SFR}) = (-0.55 \pm 0.07) \log \text{sSFR} + (34.6 \pm 0.7)$ . The blue dashed line marks the [Lehmer et al. \(2019\)](#) best-fit value for the HMXB component in SINGS galaxies of  $L_X(\text{PL})/\text{SFR} = 5.0 \times 10^{39}$  erg s $^{-1}$ . In the right panel, the black dashed line is the [Lehmer et al. \(2022\)](#) best-fit value for LMXBs in the SINGS galaxies,  $\log L_X(\text{LMXB})/M^* = 29.25$ .

## 5. DISCUSSION

### 5.1. Overview

IC 2431 is a triple galaxy system, with two galaxies of approximately equal stellar mass of  $\sim 5 \times 10^{10} M_\odot$ , and a third galaxy with a lower stellar mass of  $\sim 1.5 \times 10^{10} M_\odot$ . IC 2431 is undergoing a powerful starburst, with an overall SFR of about  $37 M_\odot \text{ yr}^{-1}$ . About 65% of this star formation is associated with Galaxy B, 30% with Galaxy A, and 5% with Galaxy C. Galaxy C has a moderate SFR of  $0.5 - 1 M_\odot \text{ yr}^{-1}$  (Table 2), which places it near the star-forming main sequence (e.g., [Saintonge et al. 2016](#); [Trussler et al. 2020](#)), thus it has a typical star formation rate for its stellar mass compared to normal star-forming galaxies, similar to that of normal spiral galaxies with similar stellar mass ([Smith et al. 2022, 2024](#)). In contrast, Galaxies A and B have SFRs that are enhanced relative to the main sequence by factors of about 6 and 15, respectively.

The IC 2431 system is tidally disturbed, with at least five tidal tails visible in optical images. IC 2431 has several other morphological peculiarities, including a prominent dust lane crossing Galaxy A, an apparent mid-infrared bridge between the two main galaxies, a radio ridge/jet extending perpendicularly out of the disk of Galaxy A, and spatial



offsets between the optical, infrared, and radio in the outskirts of the two larger galaxies. IC 2431 may also have an excess of hot gas relative to its SFR, compared to other star-forming systems.

All three galaxies in IC 2431 have possible AGNs. Galaxy C is listed as an optical AGN by Lee et al. (2017), although it is not detected in either the radio or X-ray maps. The putative AGNs in Galaxy A and Galaxy B are discussed in detail in Sections 5.2 and 5.3, respectively.

The interaction history of IC 2431 is uncertain; a direct head-on collision between two of the galaxies may have happened in the recent past, as in the Taffy galaxy pair; alternatively, a grazing tidal encounter may have occurred. These possibilities are discussed below.

### 5.2. A Possible Radio AGN in Galaxy A

Galaxy A has a radio continuum excess relative to its SFR, and the X-ray spectrum of the apparent nucleus is best-fit by a power law model. This nucleus may be variable in both the radio and the X-ray. A radio jet/ridge extends about  $4''$  (4 kpc projected size) from this nucleus. This feature is anti-coincident with the hot gas as seen in the 1.0 – 2.5 keV X-ray map, but approximately aligned with the mid-infrared bridge, and parallel to, but offset from, the dust lane seen in the optical images. Its apparent connection to the nucleus is strong evidence that this structure is indeed a radio jet, although it does not meet the formal definition of a jet given by Bridle & Perley (1984): at least four times as long as it is wide. The core power of Galaxy A in IC 2431 at 4.86 GHz is about  $6 \times 10^{21}$  W Hz $^{-1}$ , placing it near the bottom of the range for the radio galaxies with jets in the Bridle & Perley (1984) sample. The total 1.49 GHz power for Galaxy A is  $2 \times 10^{23}$  W Hz $^{-1}$  (Stine 1992). Although this luminosity is below the luminosity cutoff of  $10^{24}$  W Hz $^{-1}$  used by Tadhunter (2016) to define a radio AGN, IC 2431 has a high radio/FIR ratio relative to that expected from star formation alone (Stine 1992; Crawford et al. 1996).

The jet/ridge in Galaxy A has a steeper radio spectral index ( $\alpha = -0.7$  to  $-1.1$ ;  $S_\nu \propto \nu^\alpha$ ) than the nucleus ( $\alpha \sim -0.6$ ), with  $\alpha$  steepening with increasing distance from the nucleus. The Centaurus A radio jet has  $\alpha$  ranging from  $-0.39$  to  $-0.72$ , also decreasing along the length of the jet (Burns et al. 1983). Such a variation along a jet suggests aging of relativistic electrons (Burns et al. 1983). Such steepening of the spectral index along radio lobes is seen in other galaxies as well (Myers & Spangler 1985). Only one apparent jet is visible in IC 2431. One-sided jets are common in radio galaxies (Kellermann & Owen 1988; Bridle & Perley 1984). Relativistic beaming and Doppler-boosting (Blandford & Königl 1979) may contribute to one-sidedness in radio jets.

In IC 2431, the radio jet may have been disturbed by the on-going interaction between the galaxies. Its morphology, with enhanced flux at the end of the ridge/jet, is consistent with an interaction with the surrounding interstellar medium. The diffuse 1.49 GHz emission to the northeast of the jet/ridge may be a consequence of an interaction of the jet with interstellar matter during a close encounter between galaxies. Jets within groups or clusters can be distorted by ram pressure due to motion of a galaxy through a cluster/group intracluster/intragroup medium (Burns & Owen 1980; Blanton et al. 2001; Freeland & Wilcots 2011; Silverstein et al. 2018). In colliding galaxies, ram pressure due to the interstellar matter in a companion galaxy may also distort a jet (van Breugel et al. 1986; Stocke & Burns 1987; Borne & Colina 1993; Sakelliou et al. 1996). For example, the very asymmetric radio jets/lobes in NGC 4410 may have been caused by interactions in a group (Stocke & Burns 1987; Smith 2000).

The Hubble type of Galaxy A in IC 2431 is uncertain, but it may be a disk galaxy. Most radio galaxies have elliptical morphologies (Wilson & Colbert 1995; Antonucci 1993; Comerford et al. 2020), but spiral galaxies have also been known to host active nuclei with radio jets (Stocke & Burns 1987; Wilson & Ulvestad 1983; Venturi et al. 2021; Peralta de Arriba et al. 2023) and/or large radio lobes (Ledlow et al. 1998; Hota et al. 2011; Singh et al. 2015; Mao et al. 2015; Gao et al. 2023).

The anti-coincidence of the radio jet/ridge in IC 2431 with the medium-energy X-ray emission is suggestive of an interaction of a jet with the surrounding medium. In some compact groups with radio jets/lobes, X-ray cavities are observed to surround the radio features (Birzan et al. 2004; Rafferty et al. 2013; Randall et al. 2015; Kolokythas et al. 2020). In IC 2431, the X-ray source that lies between the two galaxies, source #5, is adjacent to the radio structure and has a thermal spectrum, thus may be shocked gas associated with jet impact. This source does not have strong mid-IR emission associated with it, unlike sources #1 and #2, thus it may not be a dusty star-forming region.

AGN feedback may be responsible for the apparent excess of hot X-ray emitting gas in IC 2431 relative to the SFR, compared to the other galaxy systems in our comparison set (Figure 17). According to Croston et al. (2005), groups that host radio AGNs have hotter intragroup gas than radio-quiet groups. AGN feedback is a popular explanation for the hot gas seen in elliptical galaxies (Fabian 2012; Choi et al. 2014, 2015) and in galaxy groups (Choi et al. 2015;

Kolokythas et al. 2020). In numerical simulations of elliptical formation via major mergers, AGN feedback contributes significantly to heating the interstellar gas (Cox et al. 2006; Choi et al. 2015). It is suggestive that the two groups in our comparison sample that host radio galaxies, HCG 62 and NGC 4410, also show excess hot gas relative to their SFR and sSFR, compared to other star-forming galaxies. However, the hot gas excess in IC 2431 is associated with both Galaxy A and Galaxy B, not Galaxy A alone, so this explanation is uncertain.

Although a jet/interstellar medium interaction can account for many of the observed properties of IC 2431, the spectacular dust lane crossing Galaxy A that is visible in optical images cannot easily be explained with this scenario alone; it also requires a strong tidal effect or a collision between galaxies. The dust lane is likely either: a) a disturbed tidal arm/tail of either Galaxy B or Galaxy C projected in front of Galaxy A, or b) interstellar matter ram pressure-stripped from Galaxy B or Galaxy C during a head-on collision between two galaxies. If a radio AGN is present, the jet may impinge on stripped or tidal gas pulled out during an interaction/collision, so its morphology may be affected by the motions in the group.

There is, however, an alternative scenario that can account for both the radio jet/ridge and the dust lane simultaneously: the radio structure may have been caused by gas stripped from a galaxy during a head-on collision with another galaxy, as in the radio continuum bridge in the Taffy galaxies (Condon et al. 1993). Perhaps a similar process has happened in IC 2431. This possibility is discussed further in Section 5.4.

### 5.3. The Galactic Nucleus of Galaxy B: A Possible Obscured AGN?

The possible nucleus of Galaxy B, X-ray source #10, may be variable, and is best-fit by two APEC components, both highly obscured. Possible explanations include:

1) It may be a young supernova with a relatively high temperature, but still thermal and declining exponentially. However, the higher temperature APEC component of source #10 has an unabsorbed  $L_X \sim 10^{43}$  erg s $^{-1}$ . This is high for a supernova, which typically peak near or below  $0.3 - 1 \times 10^{42}$  erg s $^{-1}$  (Chandra et al. 2015; Dwarkadas et al. 2016; Nucita et al. 2017; Margutti et al. 2018; Quirola-Vázquez et al. 2019). Only very rare super-luminous supernovae sometimes reach higher X-ray luminosities (Levan et al. 2013; Margutti et al. 2018; Gal-Yam 2019).

2) It may be a super-Eddington stellar mass black hole, in which the X-ray spectrum typically has a sharp downturn above a few keV; the exact value of the downturn depends on viewing angle, outflow density, and accretion rate (Poutanen et al. 2007; Pinto et al. 2017). For example, it may be a ULX like NGC 247 X-1 (Feng et al. 2016; Pinto et al. 2021) or NGC 55 X-1 (Pinto et al. 2017; Barra et al. 2022), which have similar slope/temperature above 2 keV as our nuclear source.

3) It may be an IMBH, with a mass between  $10^3 - 10^5 M_\odot$ . Likely IMBH candidates have soft and variable X-ray counterparts with  $L_X \sim 10^{42} L_\odot$  (Farrell et al. 2009; Soria et al. 2017; Chang et al. 2025). IMBHs may exist in the nuclei of dwarf galaxies and late-type spiral galaxies, if the correlation between central black hole mass and the spheroidal component of the host galaxy holds to low masses (Chilingarian et al. 2018; Graham et al. 2021). Because the morphology of IC 2431 is peculiar, a disk/bulge decomposition for Galaxy B has not been done. However, given the relatively large stellar mass of  $5 \times 10^{10} M_\odot$  for Galaxy B, the nuclear black hole might be expected to be more massive than an IMBH.

4) It may be a thermal tidal disruption event (TDE), which happens when a star gets too close to a massive black hole and is destroyed by tidal forces (e.g., Rees 1988). Such events would produce a transient thermal X-ray spectrum (Bade et al. 1996; Saxton et al. 2020; Sacchi et al. 2023). Observationally, TDEs may appear as sources with very steep X-ray spectra ( $\Gamma > 3$ ) and high  $L_X > 10^{41}$  erg s $^{-1}$  (Sacchi et al. 2023). These events would be highly absorbed if inside a starburst nucleus, and therefore may be missed in the optical because of the extinction. TDEs are very rare, however, with rates of approximately  $1 - 2 \times 10^{-5}$  galaxy $^{-1}$  yr $^{-1}$  (Donley et al. 2002; Sazonov et al. 2021; Sacchi et al. 2023), thus the probability that one would occur in IC 2431 during our observation is small.

5) Alternatively, the nucleus of Galaxy B may be a changing-look AGN, which vary dramatically on short timescales ( $<1$  day to years) (Ricci & Trakhtenbrot 2023). These sometimes have soft X-ray spectra (Terashima et al. 2012; Sacchi et al. 2023). The variability in the X-ray may be caused in part by changes in obscuration with time, with  $N_H$  varying from  $<10^{22}$  cm $^{-2}$  to  $>2 \times 10^{24}$  cm $^{-2}$  (Risaliti et al. 2002; Markowitz et al. 2014; Rivers et al. 2015; Marchesi et al. 2022; Ricci & Trakhtenbrot 2023). For an intrinsic power law spectrum, the ratio of the flux in the 7 – 10 keV band vs. that in the 2 – 4 keV band (i.e., the observed hardness ratio  $F_{7-10\text{keV}}/F_{2-4\text{keV}}$ ) increases with  $N_H$  to  $N_H \sim 5 \times 10^{23}$  cm $^{-2}$ , then drops precipitously (Markowitz et al. 2014). When in a high absorption state, such sources

are expected to appear very soft. In our 2-component fits for the nucleus of Galaxy B, the harder component has an unabsorbed luminosity  $\sim 10^{43}$  erg s $^{-1}$ , consistent with a soft changing-look AGN.

#### 5.4. *A Head-On Collision Between Gas Rich Galaxies?*

There are some morphological signs that a head-on collision between two galaxies may have occurred in IC 2431 in the recent past. These include the dust lane visible in the optical, the dust bridge seen in the mid-infrared, the hot gas between the galaxies in the X-ray maps (i.e., X-ray source #5), and the mid-IR/optical offsets in Galaxy A. These features may have been produced by ram pressure stripping of interstellar matter during such a collision. Which of the three galaxies were involved in this collision is uncertain, however. Galaxy C is faint in the mid-IR, in spite of its flattened disk-like shape, and the dust lane crossing Galaxy A is aligned with the disk of Galaxy C. This suggests that Galaxy C might have traveled through Galaxy B and/or Galaxy A and got stripped in the process. Alternatively, Galaxy A and Galaxy B might have suffered a face-on collision, like the Taffy galaxy pair. This idea is supported by the observation that the southern portion of Galaxy A lacks mid-IR emission, and the mid-IR is offset from the optical in the north of Galaxy A.

The radio continuum ridge in Galaxy A is another peculiar feature that could be accounted for by a head-on collision. This structure may be similar to the radio continuum bridge in the Taffy galaxies (Condon et al. 1993), perhaps at an earlier stage. In the Taffy system, cosmic rays, magnetic fields, and HI gas were removed from the disk, and the radio continuum in the gas enhanced by synchrotron emission from relativistic electrons trapped in the bridge (Condon et al. 1993; Yeager & Struck 2020; Yeager et al. 2024). Such features are called ‘splash bridges’ (Yeager & Struck 2020; Yeager et al. 2024). In the Taffy radio continuum bridge, the radio spectral index  $\alpha = -1.4$  is considerably steeper than than the values of  $-0.7$  to  $-0.9$  in the galactic disks of the Taffy galaxies (Condon et al. 1993). The latter is similar to the median spectral index for spiral galaxies. According to Condon et al. (1993), the steep spectral index in the Taffy bridge is due to synchrotron and inverse Compton losses, with a time scale of  $\sim 2 \times 10^7$  yr $^{-1}$ . The  $\alpha$  for the Taffy bridge is steeper than the  $\alpha = -1.1$  at the tip of the IC 2431 radio ridge, however, given the uncertainty on  $\alpha$  of  $\sim 0.2$  for the IC 2431 feature, these spectral indices agree within  $1-2\sigma$ .

Our detection of high  $L_X(\text{gas})/\text{SFR}$  in IC 2431 compared to other star-forming galaxies is another observation that might be explained by a head-on encounter. The production of hot gas during a head-on collision of equal-mass galaxies was modeled by Cox et al. (2006), who found that  $L_X(\text{gas})$  can increase by more than an order of magnitude at the time of the first disk impact due to shock heating. In contrast to these models, however, in the Smith et al. (2018) study of  $L_X(\text{gas})/\text{SFR}$  ratios of 49 major mergers in different merger stages, no trend with stage is evident. The lack of an observed trend with merger stage may be due to variations in the interaction parameters from system to system, causing the timing and intensity of the X-ray enhancement from shocks to vary from system to system. Perhaps IC 2431 is viewed at an optimal time and has favorable orbital parameters for shock heating of the gas.

The Taffy galaxy pair is generally considered the prototype of this kind of collision, as it has a bridge of hot gas, a radio continuum bridge, and spectral signatures of strong interstellar shocks (Condon et al. 1993; Peterson et al. 2012; Appleton et al. 2015; Joshi et al. 2019). As discussed in Section 4.4, however, it is uncertain whether the Taffy system as a whole has a global excess of hot gas relative to the SFR.

We can estimate the amount of energy that would be available for gas heating from such a head-on collision. This energy would be approximately  $(f/2)Mv^2$ , where  $f$  is an efficiency factor,  $M$  the total gas mass, and  $v$  the relative velocity. This gives  $f \times 2.5 \times 10^{56}$  ergs of energy, assuming a total mass of hot gas of  $10^8 M_\odot$  and  $v = 500$  km s $^{-1}$ . If this is mostly radiated away in X-rays, the implied X-ray luminosity would be  $f \times 8 \times 10^{40}$  erg s $^{-1} \times (100 \text{ Myrs}/\tau)$ , where  $\tau$  is the cooling time for the hot gas in units of Myrs. Assuming an efficiency of close to 100% and a cooling time of  $\sim 30$  Myrs, this estimate is consistent with the observed excess X-ray luminosity relative to the SFR.

## 6. SUMMARY

We have conducted a multi-wavelength analysis of the compact galaxy group IC 2431, using new Chandra X-ray images and archival UV, optical, IR, and radio maps. IC 2431 has some very unusual morphological features indicative of a recent collision and/or strong gravitational interactions between the galaxies, and possible AGN activity. These peculiar structures include: a prominent dust lane visible in optical images, a mid-IR bridge connecting two galaxies in Spitzer images, a massive concentration ( $2 \times 10^7 M_\odot$ ) of X-ray-emitting hot gas between the galaxies, and a 4 kpc-long radio continuum jet/ridge extending from a galactic nucleus. The Chandra data show an excess of hot gas in the system, relative to the star formation rate, compared to other star-forming systems.

One possible explanation of these peculiarities is a recent head-on collision between two gas-rich disk galaxies. Ram pressure stripping of interstellar matter during such a collision may have pulled out gas and dust from the disks, creating a bridge between the galaxies. Shock heating during the impact may be responsible for the hot gas observed between the two disks, as well as the excess of hot gas relative to other star-forming galaxies. The radio continuum ridge may have been created by this process, powered by relativistic electrons trapped by interstellar magnetic fields.

Alternatively, the observed radio continuum ridge in IC 2431 may be a one-sided radio jet powered by an AGN. In this picture, the global excess of hot gas and the large concentration of hot gas between the galaxies may have been caused by this jet impinging on interstellar matter. In this second scenario, tidal interactions have perturbed the interstellar matter in these galaxies, which in turn has disturbed and distorted the radio jet. A third possibility is a combination of these two: a head-on collision causing ram pressure stripping, plus a radio jet disturbed by an interaction with interstellar gas.

More observations are needed to better understand this system, and to distinguish between these possibilities. For example, optical and/or infrared imaging spectroscopy could be used to search for signatures of shock heating, and to measure the kinematics of the system. Interferometric 21 cm radio and 2.6 mm millimeter maps of the cold interstellar gas and its kinematics would help constrain the evolutionary state of the system. More sensitive and/or higher resolution radio continuum maps would be useful to distinguish between a radio AGN and a splash bridge as the cause of the radio ridge/jet in Galaxy A.

This paper employs a list of Chandra datasets, obtained by the Chandra X-ray Observatory, contained in the Chandra Data Collection (CDC) 416 <https://doi.org/10.25574/cdc.416>. Support for this research was provided by the National Aeronautics and Space Administration through Chandra Award Number GO3-24108X issued by the Chandra X-ray Center, which is operated by the Smithsonian Astrophysical Observatory for and on behalf of the National Aeronautics Space Administration under contract NAS8-03060. RS acknowledges the INAF grant No. 1.05.23.04.04. We thank the anonymous referee for carefully reading the paper and providing helpful suggestions. We also thank Michael Blanton for his work in developing the *kcorrect* software, and for his help in using the code.

This work is also based [in part] on observations made with the Spitzer Space Telescope, which was operated by the Jet Propulsion Laboratory, California Institute of Technology under a contract with NASA. This research is also based in part on observations made with the NASA/ESA Hubble Space Telescope, and obtained from the Hubble Legacy Archive, which is a collaboration between the Space Telescope Science Institute (STScI/NASA), the Space Telescope European Coordinating Facility (ST-ECF/ESA) and the Canadian Astronomy Data Centre (CADC/NRC/CSA). This research also uses data from the Very Large Array, operated by the National Radio Astronomy Observatory. The National Radio Astronomy Observatory is a facility of the National Science Foundation operated under cooperative agreement by Associated Universities, Inc. This research used data from the Galaxy Evolution Explorer (GALEX), a NASA mission. This research has made use of the NASA/IPAC Extragalactic Database, which is funded by the National Aeronautics and Space Administration and operated by the California Institute of Technology.

This research also made use of data from the Legacy Surveys. The Legacy Surveys consist of three individual and complementary projects: the Dark Energy Camera Legacy Survey (DECaLS; Proposal ID #2014B-0404; PIs: David Schlegel and Arjun Dey), the Beijing-Arizona Sky Survey (BASS; NOAO Prop. ID #2015A-0801; PIs: Zhou Xu and Xiaohui Fan), and the Mayall z-band Legacy Survey (MzLS; Prop. ID #2016A-0453; PI: Arjun Dey). DECaLS, BASS and MzLS together include data obtained, respectively, at the Blanco telescope, Cerro Tololo Inter-American Observatory, NSF's NOIRLab; the Bok telescope, Steward Observatory, University of Arizona; and the Mayall telescope, Kitt Peak National Observatory, NOIRLab. Pipeline processing and analyses of the data were supported by NOIRLab and the Lawrence Berkeley National Laboratory (LBNL). The Legacy Surveys project is honored to be permitted to conduct astronomical research on Iolkam Du'ag (Kitt Peak), a mountain with particular significance to the Tohono O'odham Nation. NOIRLab is operated by the Association of Universities for Research in Astronomy (AURA) under a cooperative agreement with the National Science Foundation. LBNL is managed by the Regents of the University of California under contract to the U.S. Department of Energy. This project used data obtained with the Dark Energy Camera (DECam), which was constructed by the Dark Energy Survey (DES) collaboration. Funding for the DES Projects has been provided by the U.S. Department of Energy, the U.S. National Science Foundation, the Ministry of Science and Education of Spain, the Science and Technology Facilities Council of the United Kingdom, the Higher Education Funding Council for England, the National Center for Supercomputing Applications at the University of Illinois at Urbana-Champaign, the Kavli Institute of Cosmological Physics at the University of Chicago, Center for Cosmology and Astro-Particle Physics at the Ohio State University, the Mitchell Institute for Fundamental



Physics and Astronomy at Texas A&M University, Financiadora de Estudos e Projetos, Fundacao Carlos Chagas Filho de Amparo, Financiadora de Estudos e Projetos, Fundacao Carlos Chagas Filho de Amparo a Pesquisa do Estado do Rio de Janeiro, Conselho Nacional de Desenvolvimento Cientifico e Tecnologico and the Ministerio da Ciencia, Tecnologia e Inovacao, the Deutsche Forschungsgemeinschaft and the Collaborating Institutions in the Dark Energy Survey. The Collaborating Institutions are Argonne National Laboratory, the University of California at Santa Cruz, the University of Cambridge, Centro de Investigaciones Energeticas, Medioambientales y Tecnologicas-Madrid, the University of Chicago, University College London, the DES-Brazil Consortium, the University of Edinburgh, the Eidgenossische Technische Hochschule (ETH) Zurich, Fermi National Accelerator Laboratory, the University of Illinois at Urbana-Champaign, the Institut de Ciencies de l’Espai (IEEC/CSIC), the Institut de Fisica d’Altes Energies, Lawrence Berkeley National Laboratory, the Ludwig Maximilians Universitat Munchen and the associated Excellence Cluster Universe, the University of Michigan, NSF’s NOIRLab, the University of Nottingham, the Ohio State University, the University of Pennsylvania, the University of Portsmouth, SLAC National Accelerator Laboratory, Stanford University, the University of Sussex, and Texas A&M University. BASS is a key project of the Telescope Access Program (TAP), which has been funded by the National Astronomical Observatories of China, the Chinese Academy of Sciences (the Strategic Priority Research Program “The Emergence of Cosmological Structures” Grant # XDB09000000), and the Special Fund for Astronomy from the Ministry of Finance. The BASS is also supported by the External Cooperation Program of Chinese Academy of Sciences (Grant # 114A11KYSB20160057), and Chinese National Natural Science Foundation (Grant # 12120101003, # 11433005). The Legacy Surveys imaging of the DESI footprint is supported by the Director, Office of Science, Office of High Energy Physics of the U.S. Department of Energy under Contract No. DE-AC02-05CH1123, by the National Energy Research Scientific Computing Center, a DOE Office of Science User Facility under the same contract; and by the U.S. National Science Foundation, Division of Astronomical Sciences under Contract No. AST-0950945 to NOAO.

## APPENDIX

### A. PHOTOMETRY

In Table 6, we provide the UV/optical/IR fluxes for the three galaxies in IC 2431, plus the global values within 12'' and 24'' radii. In Table 7, we provide UV/optical/IR fluxes in 18 bands for the seven smaller rectangular regions in IC 2431: regions A1, A2, A3, A4, B1, B2, and B3 (see Figures 9 and 10).

### B. DETAILS OF THE POPULATION SYNTHESIS MODELING

In this section, we provide additional information about the method we used to model the stellar populations in IC 2431. In addition to the parameters mentioned in Section 3.4, CIGALE also requires a number of other parameters, including the e-folding time of the old stellar population, the onset age for the main stellar population, the ratio  $E(B-V)(\text{stars})/E(B-V)(\text{lines})$ , the slope of the power law of the Calzetti et al. (2000) attenuation curve, the Draine et al. (2014), dust emission parameter  $q_{\text{PAHs}}$  (the fraction of the dust mass in PAHs), the minimum UV radiation field  $U_{\text{min}}$ , the power law slope  $\alpha$  of the dust emission curve, as defined by  $dM_{\text{dust}}/dU \propto U^{-\alpha}$ , and the illumination fraction from  $U_{\text{min}}$  to  $U_{\text{max}}$ . In Table 8, we provide the choices we permitted for the parameters that were allowed to vary. The onset age for the main stellar population is fixed to 13 Gyrs. In modeling the nebular emission, we fixed the ionization parameter to  $\log U = -3.0$ , the electron density to  $100 \text{ cm}^{-2}$ , the Lyman continuum escape fraction to zero, the Lyman continuum dust absorption fraction to zero, and the emission line width to  $300 \text{ km s}^{-1}$ . When the best-fit value of an input parameter is an extremum of the set of input parameters listed in Table 8, we extended the input parameter range and reran CIGALE, repeating until no best-fit parameters are extrema. Many of the CIGALE output parameters were already presented in Table 2; the best-fit values of the remaining parameters are given Table 9 (for the galaxies as a whole), and Table 10 (for the seven smaller rectangular regions).

**Table 6.** Photometry of the Individual Galaxies in IC 2431<sup>a</sup>

Filter	24''	12''	Galaxy	Galaxy	Galaxy
	Radius	Radius	A	B	C
shape	circle	circle	rectangle	rectangle	rectangle
RA (2000)	136.145030	136.145030	136.146100	136.144340	136.142800
Dec (2000)	14.594220	14.594220	14.593750	14.595020	14.599040
Box			6.9'' × 22.9''	8'' × 21.5''	19.2'' × 7.4''
P.A.			43°	43°	43°
FUV	0.959 ± 0.005	0.847 ± 0.002	0.076 ± 0.001	0.681 ± 0.002	0.029 ± 0.001
NUV	1.676 ± 0.005	1.447 ± 0.002	0.199 ± 0.001	1.047 ± 0.001	0.08 ± 0.001
SDSS u	3.091 ± 0.027	2.711 ± 0.013	0.687 ± 0.008	1.936 ± 0.008	0.155 ± 0.007
SDSS g	7.761 ± 0.008	6.549 ± 0.004	2.095 ± 0.002	4.213 ± 0.002	0.674 ± 0.002
SDSS r	11.405 ± 0.013	9.451 ± 0.007	3.603 ± 0.004	5.448 ± 0.004	1.202 ± 0.004
SDSS i	15.773 ± 0.021	13.098 ± 0.01	5.208 ± 0.006	7.3 ± 0.006	1.555 ± 0.006
SDSS z	18.831 ± 0.068	15.769 ± 0.034	6.742 ± 0.02	8.427 ± 0.021	1.932 ± 0.019
HST	10.909 ± 0.003	9.236 ± 0.001	3.39 ± 0.001	5.523 ± 0.001	1.064 ± 0.001
DES g	7.938 ± 0.002	6.708 ± 0.001	2.194 ± 0.001	4.267 ± 0.001	0.704 ± 0.001
DES r	13.127 ± 0.003	11.017 ± 0.002	4.143 ± 0.001	6.403 ± 0.001	1.265 ± 0.001
DES z	18.787 ± 0.008	15.777 ± 0.004	6.725 ± 0.002	8.446 ± 0.002	1.908 ± 0.002
J	28.87 ± 0.146	24.022 ± 0.073	9.879 ± 0.043	12.27 ± 0.045	2.558 ± 0.041
H	34.164 ± 0.252	28.449 ± 0.126	12.442 ± 0.075	14.445 ± 0.078	3.098 ± 0.07
K	33.832 ± 0.212	28.875 ± 0.106	12.637 ± 0.063	14.345 ± 0.065	2.685 ± 0.059
W1	20.509 ± 0.006	16.178 ± 0.003			
W2	15.925 ± 0.005	12.345 ± 0.003			
W3	104.2 ± 0.036	69.815 ± 0.018			
W4	270.427 ± 0.083	127.739 ± 0.042			
IRAC ch1	23.837 ± 0.009	20.731 ± 0.004	8.271 ± 0.003	11.535 ± 0.003	1.28 ± 0.002
IRAC ch2	18.164 ± 0.011	15.935 ± 0.006	6.107 ± 0.003	9.183 ± 0.003	0.847 ± 0.003
IRAC ch3	40.187 ± 0.047	35.187 ± 0.024	11.288 ± 0.014	22.338 ± 0.015	0.919 ± 0.013
IRAC ch4	177.351 ± 0.051	159.378 ± 0.025	44.947 ± 0.015	105.91 ± 0.016	2.151 ± 0.014

<sup>a</sup>Units are mJy. The quoted uncertainties are statistical, and do not include uncertainties in the flux calibration.

*Facilities:* CXO

## REFERENCES

- Alatalo, K., Appleton, P. N., Lisenfeld, U., et al. 2015, *ApJ*, 812, 117, doi: [10.1088/0004-637X/812/2/117](https://doi.org/10.1088/0004-637X/812/2/117)
- Antonucci, R. 1993, *ARA&A*, 31, 473, doi: [10.1146/annurev.aa.31.090193.002353](https://doi.org/10.1146/annurev.aa.31.090193.002353)
- Appleton, P. N., Xu, K. C., Reach, W., et al. 2006, *ApJL*, 639, L51, doi: [10.1086/502646](https://doi.org/10.1086/502646)
- Appleton, P. N., Lanz, L., Bitsakis, T., et al. 2015, *ApJ*, 812, 118, doi: [10.1088/0004-637X/812/2/118](https://doi.org/10.1088/0004-637X/812/2/118)
- Appleton, P. N., Guillard, P., Togi, A., et al. 2017, *ApJ*, 836, 76, doi: [10.3847/1538-4357/836/1/76](https://doi.org/10.3847/1538-4357/836/1/76)
- Appleton, P. N., Emonts, B., Lisenfeld, U., et al. 2022, *ApJ*, 931, 121, doi: [10.3847/1538-4357/ac63b2](https://doi.org/10.3847/1538-4357/ac63b2)
- Armus, L., Bernard-Salas, J., Spoon, H. W. W., et al. 2006, *ApJ*, 640, 204, doi: [10.1086/500040](https://doi.org/10.1086/500040)
- Ashby, M. L. N., Mahajan, S., Smith, H. A., et al. 2011, *PASP*, 123, 1011, doi: [10.1086/661920](https://doi.org/10.1086/661920)

**Table 7.** Photometry of Smaller Rectangular Regions in IC 2431<sup>a</sup>

Filter	Galaxy A1	Galaxy A2	Galaxy A3	Galaxy A4	Galaxy B1	Galaxy B2	Galaxy B3
shape	rectangle	rectangle	rectangle	rectangle	rectangle	rectangle	rectangle
RA (2000)	136.147770	136.146630	136.145510	136.144380	136.145750	136.144340	136.142920
Dec (2000)	14.595530	14.594350	14.593190	14.592020	14.596480	14.595020	14.593560
Box	6.9" $\times$ 5.7"	6.9" $\times$ 5.7"	6.9" $\times$ 5.7"	6.9" $\times$ 5.7"	8" $\times$ 7.2"	8" $\times$ 7.2"	8" $\times$ 7.2"
P.A.	43°	43°	43°	43°	43°	43°	43°
FUV	0.024 $\pm$ 0.001	0.016 $\pm$ 0.001	0.02 $\pm$ 0.001	0.174 $\pm$ 0.001	0.298 $\pm$ 0.001	0.209 $\pm$ 0.001	0.037 $\pm$ 0.001
NUV	0.058 $\pm$ 0.001	0.053 $\pm$ 0.001	0.057 $\pm$ 0.001	0.272 $\pm$ 0.001	0.471 $\pm$ 0.001	0.305 $\pm$ 0.001	0.103 $\pm$ 0.001
SDSS u	0.152 $\pm$ 0.004	0.107 $\pm$ 0.004	0.32 $\pm$ 0.004	0.628 $\pm$ 0.005	0.737 $\pm$ 0.005	0.563 $\pm$ 0.005	0.256 $\pm$ 0.006
SDSS g	0.336 $\pm$ 0.001	0.289 $\pm$ 0.001	1.158 $\pm$ 0.001	1.506 $\pm$ 0.001	1.638 $\pm$ 0.001	1.04 $\pm$ 0.001	0.631 $\pm$ 0.002
SDSS r	0.448 $\pm$ 0.002	0.543 $\pm$ 0.002	2.135 $\pm$ 0.002	1.896 $\pm$ 0.002	2.296 $\pm$ 0.002	1.226 $\pm$ 0.002	1.037 $\pm$ 0.003
SDSS i	0.647 $\pm$ 0.003	0.903 $\pm$ 0.003	3.027 $\pm$ 0.003	2.336 $\pm$ 0.004	3.213 $\pm$ 0.004	1.728 $\pm$ 0.004	1.661 $\pm$ 0.004
SDSS z	0.797 $\pm$ 0.01	1.233 $\pm$ 0.01	3.997 $\pm$ 0.01	2.665 $\pm$ 0.012	3.852 $\pm$ 0.012	1.844 $\pm$ 0.012	2.277 $\pm$ 0.014
HST	0.476 $\pm$ 0.001	0.53 $\pm$ 0.001	1.937 $\pm$ 0.001	1.869 $\pm$ 0.001	2.269 $\pm$ 0.001	1.361 $\pm$ 0.001	1.021 $\pm$ 0.001
DES g	0.334 $\pm$ 0.001	0.312 $\pm$ 0.001	1.213 $\pm$ 0.001	1.496 $\pm$ 0.001	1.701 $\pm$ 0.001	1.063 $\pm$ 0.001	0.648 $\pm$ 0.001
DES r	0.574 $\pm$ 0.001	0.686 $\pm$ 0.001	2.348 $\pm$ 0.001	2.054 $\pm$ 0.001	2.745 $\pm$ 0.001	1.592 $\pm$ 0.001	1.316 $\pm$ 0.001
DES z	0.713 $\pm$ 0.001	1.233 $\pm$ 0.001	4.055 $\pm$ 0.001	2.667 $\pm$ 0.001	3.926 $\pm$ 0.001	1.835 $\pm$ 0.001	2.186 $\pm$ 0.002
J	0.79 $\pm$ 0.021	2.498 $\pm$ 0.022	5.594 $\pm$ 0.021	3.371 $\pm$ 0.026	5.953 $\pm$ 0.025	2.901 $\pm$ 0.027	3.786 $\pm$ 0.031
H	1.022 $\pm$ 0.037	3.022 $\pm$ 0.038	7.401 $\pm$ 0.037	3.616 $\pm$ 0.044	7.456 $\pm$ 0.044	3.335 $\pm$ 0.046	4.892 $\pm$ 0.053
K	1.12 $\pm$ 0.031	3.325 $\pm$ 0.032	7.149 $\pm$ 0.031	3.354 $\pm$ 0.037	7.605 $\pm$ 0.037	3.342 $\pm$ 0.039	5.315 $\pm$ 0.044
IRAC ch1	1.139 $\pm$ 0.001	2.283 $\pm$ 0.001	4.236 $\pm$ 0.001	2.076 $\pm$ 0.002	6.343 $\pm$ 0.002	3.123 $\pm$ 0.002	4.35 $\pm$ 0.002
IRAC ch2	0.965 $\pm$ 0.002	1.768 $\pm$ 0.002	2.983 $\pm$ 0.002	1.498 $\pm$ 0.002	5.17 $\pm$ 0.002	2.52 $\pm$ 0.002	3.439 $\pm$ 0.002
IRAC ch3	2.284 $\pm$ 0.007	3.883 $\pm$ 0.007	4.471 $\pm$ 0.007	2.355 $\pm$ 0.008	13.12 $\pm$ 0.008	6.877 $\pm$ 0.008	7.373 $\pm$ 0.01
IRAC ch4	10.712 $\pm$ 0.008	16.884 $\pm$ 0.007	14.941 $\pm$ 0.008	10.072 $\pm$ 0.009	62.523 $\pm$ 0.009	33.38 $\pm$ 0.009	31.799 $\pm$ 0.011

<sup>a</sup>Units are mJy. The quoted uncertainties are statistical, and do not include uncertainties in the flux calibration.

**Table 8.** CIGALE Input Parameters

Parameter	Choices
e-folding time of the old population ( $\tau_{\text{main}}$ )	1, 3, 5, 7.5, 10 Gyr
Age of the late burst/quench	2, 5, 10, 25, 50, 75, 100 Myrs
Ratio of the SFR after/before the burst ( $r_{\text{SFR}}$ )	0.2, 0.6, 1.0, 1.25, 2.5, 5.0, 10.0
E(B–V)(line emission)	0.1, 0.2, 0.5, 0.6, 0.7, 0.8, 0.9, 1.0, 1.2, 1.5
Reduction factor E(B–V)(stars)/E(B–V)(lines)	0.25, 0.50, 0.75
Slope of power law of attenuation curve	-1.5, -1.2, -1., -0.7, -0.5, -0.3, 0.0
PAH dust mass fraction ( $q_{\text{PAH}}$ )	1.12, 2.50, 5.26, 6.63
Minimum radiation field ( $U_{\text{min}}$ )	0.1, 0.25, 0.50, 1.0, 2.5, 5.0, 10.0, 25.0, 50.0
Power-law slope ( $\alpha$ , where $dM_{\text{dust}}/dU \propto U^{-\alpha}$ )	1.5, 2.0, 2.5
Illumination fraction from $U_{\text{min}}$ to $U_{\text{max}}$	0.001, 0.003, 0.01, 0.03, 0.1, 0.3

**Table 9.** Additional CIGALE Parameters for SED Fits for the Galaxies in IC 2431

Region	A	B	C
best $\tau_{\text{main}}$ (Gyrs)	10	10	5
best E(B–V) factor	0.5	0.25	0.25
best attenuation powerlaw slope	-0.5	-0.5	-1.0
best $q_{\text{pah}}$	2.5	2.5	2.5
best dust $U_{\text{mean}}$	11.75	0.66	0.25
best dust $U_{\text{min}}$	5.0	0.25	0.25

**Table 10.** Additional CIGALE Parameters for SED Fits for the Smaller Rectangular Regions

Region	A1	A2	A3	A4	B1	B2	B3
best $\tau_{\text{main}}$ (Gyrs)	10	3	5	10	10	10	7
best E(B–V) factor	0.5	0.5	0.25	0.5	0.5	0.25	0.5
best attenuation powerlaw slope	-0.7	-0.3	-0.7	-1.0	-1.5	-0.3	-0.3
best $q_{\text{pah}}$	2.5	2.5	6.63	6.63	6.63	2.5	2.5
best dust $U_{\text{mean}}$	13.15	66.81	40.79	48.45	5.54	0.62	33.92
best dust $U_{\text{min}}$	2.5	50.0	25.0	10.0	1.0	0.1	25.0



- Bachetti, M., Harrison, F. A., Walton, D. J., et al. 2014, *Nature*, 514, 202, doi: [10.1038/nature13791](https://doi.org/10.1038/nature13791)
- Bade, N., Komossa, S., & Dahlem, M. 1996, *A&A*, 309, L35
- Bahcall, N. A., Harris, D. E., & Rood, H. J. 1984, *ApJL*, 284, L29, doi: [10.1086/184346](https://doi.org/10.1086/184346)
- Barnes, J. E. 1989, *Nature*, 338, 123, doi: [10.1038/338123a0](https://doi.org/10.1038/338123a0)
- Barra, F., Pinto, C., Walton, D. J., et al. 2022, *MNRAS*, 516, 3972, doi: [10.1093/mnras/stac2453](https://doi.org/10.1093/mnras/stac2453)
- Belfiore, F., Leroy, A. K., Williams, T. G., et al. 2023, *A&A*, 678, A129, doi: [10.1051/0004-6361/202347175](https://doi.org/10.1051/0004-6361/202347175)
- Bigwood, L., Bourne, M. A., Irsic, V., Amon, A., & Sijacki, D. 2025, arXiv e-prints, arXiv:2501.16983, doi: [10.48550/arXiv.2501.16983](https://doi.org/10.48550/arXiv.2501.16983)
- Binder, B. A., & Povich, M. S. 2018, *ApJ*, 864, 136, doi: [10.3847/1538-4357/aad7b2](https://doi.org/10.3847/1538-4357/aad7b2)
- Birzan, L., Rafferty, D. A., McNamara, B. R., Wise, M. W., & Nulsen, P. E. J. 2004, *ApJ*, 607, 800, doi: [10.1086/383519](https://doi.org/10.1086/383519)
- Blandford, R. D., & Königl, A. 1979, *ApJ*, 232, 34, doi: [10.1086/157262](https://doi.org/10.1086/157262)
- Blanton, E. L., Gregg, M. D., Helfand, D. J., Becker, R. H., & Leighly, K. M. 2001, *AJ*, 121, 2915, doi: [10.1086/321074](https://doi.org/10.1086/321074)
- Blanton, M. R., & Roweis, S. 2007, *AJ*, 133, 734, doi: [10.1086/510127](https://doi.org/10.1086/510127)
- Bode, P. W., Cohn, H. N., & Lugger, P. M. 1993, *ApJ*, 416, 17, doi: [10.1086/173211](https://doi.org/10.1086/173211)
- Boehringer, H., Voges, W., Fabian, A. C., Edge, A. C., & Neumann, D. M. 1993, *MNRAS*, 264, L25, doi: [10.1093/mnras/264.1.L25](https://doi.org/10.1093/mnras/264.1.L25)
- Bohlin, R. C., Savage, B. D., & Drake, J. F. 1978, *ApJ*, 224, 132, doi: [10.1086/156357](https://doi.org/10.1086/156357)
- Boquien, M., Burgarella, D., Roehlly, Y., et al. 2019, *A&A*, 622, A103, doi: [10.1051/0004-6361/201834156](https://doi.org/10.1051/0004-6361/201834156)
- Borne, K. D., & Colina, L. 1993, *ApJ*, 416, 157, doi: [10.1086/173222](https://doi.org/10.1086/173222)
- Bower, R. G., Benson, A. J., Malbon, R., et al. 2006, *MNRAS*, 370, 645, doi: [10.1111/j.1365-2966.2006.10519.x](https://doi.org/10.1111/j.1365-2966.2006.10519.x)
- Bridle, A. H., & Perley, R. A. 1984, *ARA&A*, 22, 319, doi: [10.1146/annurev.aa.22.090184.001535](https://doi.org/10.1146/annurev.aa.22.090184.001535)
- Bruzual, G., & Charlot, S. 2003, *MNRAS*, 344, 1000, doi: [10.1046/j.1365-8711.2003.06897.x](https://doi.org/10.1046/j.1365-8711.2003.06897.x)
- Burns, J. O., Feigelson, E. D., & Schreier, E. J. 1983, *ApJ*, 273, 128, doi: [10.1086/161353](https://doi.org/10.1086/161353)
- Burns, J. O., & Owen, F. N. 1980, *AJ*, 85, 204, doi: [10.1086/112663](https://doi.org/10.1086/112663)
- Calzetti, D., Armus, L., Bohlin, R. C., et al. 2000, *ApJ*, 533, 682, doi: [10.1086/308692](https://doi.org/10.1086/308692)
- Cash, W. 1979, *ApJ*, 228, 939, doi: [10.1086/156922](https://doi.org/10.1086/156922)
- Chabrier, G. 2003, *ApJL*, 586, L133, doi: [10.1086/374879](https://doi.org/10.1086/374879)
- Chandra, P., Chevalier, R. A., Chugai, N., Fransson, C., & Soderberg, A. M. 2015, *ApJ*, 810, 32, doi: [10.1088/0004-637X/810/1/32](https://doi.org/10.1088/0004-637X/810/1/32)
- Chang, Y.-C., Soria, R., Kong, A. K. H., et al. 2025, arXiv e-prints, arXiv:2503.00904, doi: [10.48550/arXiv.2503.00904](https://doi.org/10.48550/arXiv.2503.00904)
- Chilingarian, I. V., Katkov, I. Y., Zolotukhin, I. Y., et al. 2018, *ApJ*, 863, 1, doi: [10.3847/1538-4357/aad184](https://doi.org/10.3847/1538-4357/aad184)
- Choi, E., Naab, T., Ostriker, J. P., Johansson, P. H., & Moster, B. P. 2014, *MNRAS*, 442, 440, doi: [10.1093/mnras/stu874](https://doi.org/10.1093/mnras/stu874)
- Choi, E., Ostriker, J. P., Naab, T., Oser, L., & Moster, B. P. 2015, *MNRAS*, 449, 4105, doi: [10.1093/mnras/stv575](https://doi.org/10.1093/mnras/stv575)
- Chomiuk, L., & Povich, M. S. 2011, *AJ*, 142, 197, doi: [10.1088/0004-6256/142/6/197](https://doi.org/10.1088/0004-6256/142/6/197)
- Cluver, M. E., Appleton, P. N., Boulanger, F., et al. 2010, *ApJ*, 710, 248, doi: [10.1088/0004-637X/710/1/248](https://doi.org/10.1088/0004-637X/710/1/248)
- Cluver, M. E., Appleton, P. N., Ogle, P., et al. 2013, *ApJ*, 765, 93, doi: [10.1088/0004-637X/765/2/93](https://doi.org/10.1088/0004-637X/765/2/93)
- Comerford, J. M., Negus, J., Müller-Sánchez, F., et al. 2020, *ApJ*, 901, 159, doi: [10.3847/1538-4357/abb2ae](https://doi.org/10.3847/1538-4357/abb2ae)
- Condon, J. J., Helou, G., Sanders, D. B., & Soifer, B. T. 1993, *AJ*, 105, 1730, doi: [10.1086/116549](https://doi.org/10.1086/116549)
- Cox, T. J., Di Matteo, T., Hernquist, L., et al. 2006, *ApJ*, 643, 692, doi: [10.1086/503284](https://doi.org/10.1086/503284)
- Coziol, R., & Plauchu-Frayn, I. 2007, *AJ*, 133, 2630, doi: [10.1086/513514](https://doi.org/10.1086/513514)
- Crawford, T., Marr, J., Partridge, B., & Strauss, M. A. 1996, *ApJ*, 460, 225, doi: [10.1086/176964](https://doi.org/10.1086/176964)
- Crivellari, E., Wolter, A., & Trinchieri, G. 2009, *A&A*, 501, 445, doi: [10.1051/0004-6361/200810707](https://doi.org/10.1051/0004-6361/200810707)
- Croston, J. H., Hardcastle, M. J., & Birkinshaw, M. 2005, *MNRAS*, 357, 279, doi: [10.1111/j.1365-2966.2005.08665.x](https://doi.org/10.1111/j.1365-2966.2005.08665.x)
- Croton, D. J., Springel, V., White, S. D. M., et al. 2006, *MNRAS*, 365, 11, doi: [10.1111/j.1365-2966.2005.09675.x](https://doi.org/10.1111/j.1365-2966.2005.09675.x)
- Dale, D. A., Boquien, M., Turner, J. A., et al. 2023, *AJ*, 165, 260, doi: [10.3847/1538-3881/acfffe](https://doi.org/10.3847/1538-3881/acfffe)
- Dale, D. A., & Helou, G. 2002, *ApJ*, 576, 159, doi: [10.1086/341632](https://doi.org/10.1086/341632)
- Dale, D. A., Helou, G., Silberman, N. A., et al. 1999, *AJ*, 118, 2055, doi: [10.1086/301110](https://doi.org/10.1086/301110)
- Dale, D. A., Cook, D. O., Roussel, H., et al. 2017, *ApJ*, 837, 90, doi: [10.3847/1538-4357/aa6032](https://doi.org/10.3847/1538-4357/aa6032)
- Desjardins, T. D., Gallagher, S. C., Tzanavaris, P., et al. 2013, *ApJ*, 763, 121, doi: [10.1088/0004-637X/763/2/121](https://doi.org/10.1088/0004-637X/763/2/121)
- Desjardins, T. D., Gallagher, S. C., Hornschemeier, A. E., et al. 2014, *ApJ*, 790, 132, doi: [10.1088/0004-637X/790/2/132](https://doi.org/10.1088/0004-637X/790/2/132)
- Dey, A., Schlegel, D. J., Lang, D., et al. 2019, *AJ*, 157, 168, doi: [10.3847/1538-3881/ab089d](https://doi.org/10.3847/1538-3881/ab089d)

- Donahue, M., Smith, B. J., & Stocke, J. T. 2002, *AJ*, 123, 1922, doi: [10.1086/339556](https://doi.org/10.1086/339556)
- Donley, J. L., Brandt, W. N., Eracleous, M., & Boller, T. 2002, *AJ*, 124, 1308, doi: [10.1086/342280](https://doi.org/10.1086/342280)
- Donnan, F. R., García-Bernete, I., Rigopoulou, D., et al. 2023, *MNRAS*, 519, 3691, doi: [10.1093/mnras/stac3729](https://doi.org/10.1093/mnras/stac3729)
- Draine, B. T., Aniano, G., Krause, O., et al. 2014, *ApJ*, 780, 172, doi: [10.1088/0004-637X/780/2/172](https://doi.org/10.1088/0004-637X/780/2/172)
- Drevet Mulard, M., Nesvadba, N. P. H., Meenakshi, M., et al. 2023, *A&A*, 676, A35, doi: [10.1051/0004-6361/202245173](https://doi.org/10.1051/0004-6361/202245173)
- Dubois, Y., Devriendt, J., Slyz, A., & Teyssier, R. 2010, *MNRAS*, 409, 985, doi: [10.1111/j.1365-2966.2010.17338.x](https://doi.org/10.1111/j.1365-2966.2010.17338.x)
- Dwarkadas, V. V., Romero-Cañizales, C., Reddy, R., & Bauer, F. E. 2016, *MNRAS*, 462, 1101, doi: [10.1093/mnras/stw1717](https://doi.org/10.1093/mnras/stw1717)
- Eckert, D., Gaspari, M., Gastaldello, F., Le Brun, A. M. C., & O'Sullivan, E. 2021, *Universe*, 7, 142, doi: [10.3390/universe7050142](https://doi.org/10.3390/universe7050142)
- Eckert, D., Gastaldello, F., O'Sullivan, E., Finoguenov, A., & Brienza, M. 2024, *Galaxies*, 12, 24, doi: [10.3390/galaxies12030024](https://doi.org/10.3390/galaxies12030024)
- Engelbracht, C. W., Gordon, K. D., Rieke, G. H., et al. 2005, *ApJL*, 628, L29, doi: [10.1086/432613](https://doi.org/10.1086/432613)
- Engelbracht, C. W., Rieke, G. H., Gordon, K. D., et al. 2008, *ApJ*, 678, 804, doi: [10.1086/529513](https://doi.org/10.1086/529513)
- Evans, I. N., Evans, J. D., Martínez-Galarza, J. R., et al. 2024, *arXiv e-prints*, arXiv:2407.10799, doi: [10.48550/arXiv.2407.10799](https://doi.org/10.48550/arXiv.2407.10799)
- Fabian, A. C. 2012, *ARA&A*, 50, 455, doi: [10.1146/annurev-astro-081811-125521](https://doi.org/10.1146/annurev-astro-081811-125521)
- Fabian, A. C., Sanders, J. S., Allen, S. W., et al. 2003, *MNRAS*, 344, L43, doi: [10.1046/j.1365-8711.2003.06902.x](https://doi.org/10.1046/j.1365-8711.2003.06902.x)
- Farrell, S. A., Webb, N. A., Barret, D., Godet, O., & Rodrigues, J. M. 2009, *Nature*, 460, 73, doi: [10.1038/nature08083](https://doi.org/10.1038/nature08083)
- Fazio, G. G., Hora, J. L., Allen, L. E., et al. 2004, *ApJS*, 154, 10, doi: [10.1086/422843](https://doi.org/10.1086/422843)
- Feng, H., Tao, L., Kaaret, P., & Grisé, F. 2016, *ApJ*, 831, 117, doi: [10.3847/0004-637X/831/2/117](https://doi.org/10.3847/0004-637X/831/2/117)
- Finoguenov, A., & Jones, C. 2001, *ApJL*, 547, L107, doi: [10.1086/318910](https://doi.org/10.1086/318910)
- Freeland, E., & Wilcots, E. 2011, *ApJ*, 738, 145, doi: [10.1088/0004-637X/738/2/145](https://doi.org/10.1088/0004-637X/738/2/145)
- Fuse, C., & Broming, E. 2013, *ApJ*, 764, 175, doi: [10.1088/0004-637X/764/2/175](https://doi.org/10.1088/0004-637X/764/2/175)
- Gaia Collaboration, Prusti, T., de Bruijne, J. H. J., et al. 2016, *A&A*, 595, A1, doi: [10.1051/0004-6361/201629272](https://doi.org/10.1051/0004-6361/201629272)
- Gal-Yam, A. 2019, *ARA&A*, 57, 305, doi: [10.1146/annurev-astro-081817-051819](https://doi.org/10.1146/annurev-astro-081817-051819)
- Gallagher, S. C., Johnson, K. E., Hornschemeier, A. E., Charlton, J. C., & Hibbard, J. E. 2008, *ApJ*, 673, 730, doi: [10.1086/524103](https://doi.org/10.1086/524103)
- Gallagher, S. C., Durrell, P. R., Elmegreen, D. M., et al. 2010, *AJ*, 139, 545, doi: [10.1088/0004-6256/139/2/545](https://doi.org/10.1088/0004-6256/139/2/545)
- Gao, X. Y., Yuan, Z. S., Han, J. L., Wen, Z. L., & Shan, S. S. 2023, *Research in Astronomy and Astrophysics*, 23, 035005, doi: [10.1088/1674-4527/acb251](https://doi.org/10.1088/1674-4527/acb251)
- Gehrels, N. 1986, *ApJ*, 303, 336, doi: [10.1086/164079](https://doi.org/10.1086/164079)
- George, I. M., Turner, T. J., Yaqoob, T., et al. 2000, *ApJ*, 531, 52, doi: [10.1086/308461](https://doi.org/10.1086/308461)
- Gitti, M., O'Sullivan, E., Giacintucci, S., et al. 2010, *ApJ*, 714, 758, doi: [10.1088/0004-637X/714/1/758](https://doi.org/10.1088/0004-637X/714/1/758)
- Graham, A. W., Soria, R., Davis, B. L., et al. 2021, *ApJ*, 923, 246, doi: [10.3847/1538-4357/ac34f4](https://doi.org/10.3847/1538-4357/ac34f4)
- Grimm, H. J., Gilfanov, M., & Sunyaev, R. 2003, *MNRAS*, 339, 793, doi: [10.1046/j.1365-8711.2003.06224.x](https://doi.org/10.1046/j.1365-8711.2003.06224.x)
- Hao, C.-N., Kennicutt, R. C., Johnson, B. D., et al. 2011, *ApJ*, 741, 124, doi: [10.1088/0004-637X/741/2/124](https://doi.org/10.1088/0004-637X/741/2/124)
- Haynes, M. P., Giovanelli, R., Kent, B. R., et al. 2018, *ApJ*, 861, 49, doi: [10.3847/1538-4357/aac956](https://doi.org/10.3847/1538-4357/aac956)
- Helou, G., Soifer, B. T., & Rowan-Robinson, M. 1985, *ApJL*, 298, L7, doi: [10.1086/184556](https://doi.org/10.1086/184556)
- Helou, G., & Walker, D. W., eds. 1988, *Infrared Astronomical Satellite (IRAS) Catalogs and Atlases. Volume 7: The Small Scale Structure Catalog.*, Vol. 7
- Helou, G., Roussel, H., Appleton, P., et al. 2004, *ApJS*, 154, 253, doi: [10.1086/422640](https://doi.org/10.1086/422640)
- Hess, K. M., Wilcots, E. M., & Hartwick, V. L. 2012, *AJ*, 144, 48, doi: [10.1088/0004-6256/144/2/48](https://doi.org/10.1088/0004-6256/144/2/48)
- Higdon, J. L. 1996, *ApJ*, 467, 241, doi: [10.1086/177599](https://doi.org/10.1086/177599)
- Hota, A., Sirothia, S. K., Ohya, Y., et al. 2011, *MNRAS*, 417, L36, doi: [10.1111/j.1745-3933.2011.01115.x](https://doi.org/10.1111/j.1745-3933.2011.01115.x)
- Hummel, E., Kotanyi, C. G., & van Gorkom, J. H. 1986, *A&A*, 155, 161
- Hwang, J.-S., Struck, C., Renaud, F., & Appleton, P. N. 2012, *MNRAS*, 419, 1780, doi: [10.1111/j.1365-2966.2011.19847.x](https://doi.org/10.1111/j.1365-2966.2011.19847.x)
- Javelle, S. 1908, *Annales de l'Observatoire de Nice*, 11, D.1
- Johnson, K. E., Hibbard, J. E., Gallagher, S. C., et al. 2007, *AJ*, 134, 1522, doi: [10.1086/520921](https://doi.org/10.1086/520921)
- Jones, L. R., Ponman, T. J., & Forbes, D. A. 2000, *MNRAS*, 312, 139, doi: [10.1046/j.1365-8711.2000.03118.x](https://doi.org/10.1046/j.1365-8711.2000.03118.x)
- Jones, L. R., Ponman, T. J., Horton, A., et al. 2003, *MNRAS*, 343, 627, doi: [10.1046/j.1365-8711.2003.06702.x](https://doi.org/10.1046/j.1365-8711.2003.06702.x)
- Jones, M. G., Verdes-Montenegro, L., Damas-Segovia, A., et al. 2019, *A&A*, 632, A78, doi: [10.1051/0004-6361/201936349](https://doi.org/10.1051/0004-6361/201936349)

- Jones, M. G., Verdes-Montenegro, L., Moldon, J., et al. 2023, *A&A*, 670, A21, doi: [10.1051/0004-6361/202244622](https://doi.org/10.1051/0004-6361/202244622)
- Joshi, B. A., Appleton, P. N., Blanc, G. A., et al. 2019, *ApJ*, 878, 161, doi: [10.3847/1538-4357/ab2124](https://doi.org/10.3847/1538-4357/ab2124)
- Kaaret, P., Feng, H., & Roberts, T. P. 2017, *ARA&A*, 55, 303, doi: [10.1146/annurev-astro-091916-055259](https://doi.org/10.1146/annurev-astro-091916-055259)
- Keel, W. C., Tate, J., Wong, O. I., et al. 2022, *AJ*, 163, 150, doi: [10.3847/1538-3881/ac517d](https://doi.org/10.3847/1538-3881/ac517d)
- Kellermann, K. I., & Owen, F. N. 1988, in *Galactic and Extragalactic Radio Astronomy*, ed. K. I. Kellermann & G. L. Verschuur, 563–602
- Kelm, B., Focardi, P., & Palumbo, G. G. C. 1998, *A&A*, 335, 912
- Kelm, B., Focardi, P., & Zitelli, V. 2004, *A&A*, 418, 25, doi: [10.1051/0004-6361:20034289](https://doi.org/10.1051/0004-6361:20034289)
- Kennicutt, Robert C., J., Armus, L., Bendo, G., et al. 2003, *PASP*, 115, 928, doi: [10.1086/376941](https://doi.org/10.1086/376941)
- Kennicutt, R. C., & Evans, N. J. 2012, *ARA&A*, 50, 531, doi: [10.1146/annurev-astro-081811-125610](https://doi.org/10.1146/annurev-astro-081811-125610)
- Kolokythas, K., O’Sullivan, E., Raychaudhury, S., et al. 2018, *Monthly Notices of the Royal Astronomical Society*, 481, 1550, doi: [10.1093/mnras/sty2030](https://doi.org/10.1093/mnras/sty2030)
- Kolokythas, K., O’Sullivan, E., Giacintucci, S., et al. 2020, *MNRAS*, 496, 1471, doi: [10.1093/mnras/staa1506](https://doi.org/10.1093/mnras/staa1506)
- Kong, A. K. H., Garcia, M. R., Primini, F. A., et al. 2002, *ApJ*, 577, 738, doi: [10.1086/342116](https://doi.org/10.1086/342116)
- Kouroumpatzakis, K., Zezas, A., Maragkoudakis, A., et al. 2021, *MNRAS*, 506, 3079, doi: [10.1093/mnras/stab1917](https://doi.org/10.1093/mnras/stab1917)
- Kraft, R. P., Vázquez, S. E., Forman, W. R., et al. 2003, *ApJ*, 592, 129, doi: [10.1086/375533](https://doi.org/10.1086/375533)
- Kroupa, P., & Weidner, C. 2003, *ApJ*, 598, 1076, doi: [10.1086/379105](https://doi.org/10.1086/379105)
- Lacy, M., Storrie-Lombardi, L. J., Sajina, A., et al. 2004, *ApJS*, 154, 166, doi: [10.1086/422816](https://doi.org/10.1086/422816)
- Ledlow, M. J., Owen, F. N., & Keel, W. C. 1998, *ApJ*, 495, 227, doi: [10.1086/305251](https://doi.org/10.1086/305251)
- Lee, G.-H., Hwang, H. S., Sohn, J., & Lee, M. G. 2017, *ApJ*, 835, 280, doi: [10.3847/1538-4357/835/2/280](https://doi.org/10.3847/1538-4357/835/2/280)
- Lehmer, B. D., Eufrasio, R. T., Basu-Zych, A., et al. 2022, *ApJ*, 930, 135, doi: [10.3847/1538-4357/ac63a7](https://doi.org/10.3847/1538-4357/ac63a7)
- Lehmer, B. D., Eufrasio, R. T., Tzanavaris, P., et al. 2019, *ApJS*, 243, 3, doi: [10.3847/1538-4365/ab22a8](https://doi.org/10.3847/1538-4365/ab22a8)
- Lenkić, L., Tzanavaris, P., Gallagher, S. C., et al. 2016, *MNRAS*, 459, 2948, doi: [10.1093/mnras/stw779](https://doi.org/10.1093/mnras/stw779)
- Levan, A. J., Read, A. M., Metzger, B. D., Wheatley, P. J., & Tanvir, N. R. 2013, *ApJ*, 771, 136, doi: [10.1088/0004-637X/771/2/136](https://doi.org/10.1088/0004-637X/771/2/136)
- Lisenfeld, U., Alatalo, K., Zucker, C., et al. 2017, *A&A*, 607, A110, doi: [10.1051/0004-6361/201730898](https://doi.org/10.1051/0004-6361/201730898)
- Madden, S. C. 2000, *NewAR*, 44, 249, doi: [10.1016/S1387-6473\(00\)00050-6](https://doi.org/10.1016/S1387-6473(00)00050-6)
- Mahajan, S., Ashby, M. L. N., Willner, S. P., et al. 2019, *MNRAS*, 482, 560, doi: [10.1093/mnras/sty2699](https://doi.org/10.1093/mnras/sty2699)
- Mao, M. Y., Owen, F., Duffin, R., et al. 2015, *MNRAS*, 446, 4176, doi: [10.1093/mnras/stu2302](https://doi.org/10.1093/mnras/stu2302)
- Marchesi, S., Zhao, X., Torres-Albà, N., et al. 2022, *ApJ*, 935, 114, doi: [10.3847/1538-4357/ac80be](https://doi.org/10.3847/1538-4357/ac80be)
- Margutti, R., Chornock, R., Metzger, B. D., et al. 2018, *ApJ*, 864, 45, doi: [10.3847/1538-4357/aad2df](https://doi.org/10.3847/1538-4357/aad2df)
- Markarian, B. E., Lipovetskii, V. A., & Stepanian, D. A. 1979, *Astrofizika*, 15, 201
- Markowitz, A. G., Krumpke, M., & Nikutta, R. 2014, *MNRAS*, 439, 1403, doi: [10.1093/mnras/stt2492](https://doi.org/10.1093/mnras/stt2492)
- Martin, D. C., Fanson, J., Schiminovich, D., et al. 2005, *ApJL*, 619, L1, doi: [10.1086/426387](https://doi.org/10.1086/426387)
- Mayya, Y. D., Bizyaev, D., Romano, R., Garcia-Barreto, J. A., & Vorobyov, E. I. 2005, *ApJL*, 620, L35, doi: [10.1086/428400](https://doi.org/10.1086/428400)
- Mazzarella, J. M., & Balzano, V. A. 1986, *ApJS*, 62, 751, doi: [10.1086/191155](https://doi.org/10.1086/191155)
- McCray, R. A. 1987, in *Spectroscopy of Astrophysical Plasmas*, ed. A. Dalgarno & D. Layzer, 255–278
- McKee, C. F., & Cowie, L. L. 1977, *ApJ*, 215, 213, doi: [10.1086/155350](https://doi.org/10.1086/155350)
- McMullin, J. P., Waters, B., Schiebel, D., Young, W., & Golap, K. 2007, in *Astronomical Society of the Pacific Conference Series*, Vol. 376, *Astronomical Data Analysis Software and Systems XVI*, ed. R. A. Shaw, F. Hill, & D. J. Bell, 127
- McNamara, B. R., & Nulsen, P. E. J. 2012, *New Journal of Physics*, 14, 055023, doi: [10.1088/1367-2630/14/5/055023](https://doi.org/10.1088/1367-2630/14/5/055023)
- McNamara, B. R., Wise, M., Nulsen, P. E. J., et al. 2000, *ApJL*, 534, L135, doi: [10.1086/312662](https://doi.org/10.1086/312662)
- Mendes de Oliveira, C., & Hickson, P. 1994, *ApJ*, 427, 684, doi: [10.1086/174175](https://doi.org/10.1086/174175)
- Mendes de Oliveira, C., Plana, H., Amram, P., Bolte, M., & Boulesteix, J. 1998, *ApJ*, 507, 691, doi: [10.1086/306365](https://doi.org/10.1086/306365)
- Mineo, S., Gilfanov, M., & Sunyaev, R. 2012a, *MNRAS*, 426, 1870, doi: [10.1111/j.1365-2966.2012.21831.x](https://doi.org/10.1111/j.1365-2966.2012.21831.x)
- . 2012b, *MNRAS*, 419, 2095, doi: [10.1111/j.1365-2966.2011.19862.x](https://doi.org/10.1111/j.1365-2966.2011.19862.x)
- Montaguth, G. P., Torres-Flores, S., Monachesi, A., et al. 2023, *MNRAS*, 524, 5340, doi: [10.1093/mnras/stad2235](https://doi.org/10.1093/mnras/stad2235)
- Mulchaey, J. S., & Zabludoff, A. I. 1998, *ApJ*, 496, 73, doi: [10.1086/305356](https://doi.org/10.1086/305356)
- Murphy, E. J., Condon, J. J., Schinnerer, E., et al. 2011, *ApJ*, 737, 67, doi: [10.1088/0004-637X/737/2/67](https://doi.org/10.1088/0004-637X/737/2/67)
- Myers, S. T., & Spangler, S. R. 1985, *ApJ*, 291, 52, doi: [10.1086/163040](https://doi.org/10.1086/163040)

- Nandra, K., & Pounds, K. A. 1994, *MNRAS*, 268, 405, doi: [10.1093/mnras/268.2.405](https://doi.org/10.1093/mnras/268.2.405)
- Nesvadba, N. P. H., Wagner, A. Y., Mukherjee, D., et al. 2021, *A&A*, 654, A8, doi: [10.1051/0004-6361/202140544](https://doi.org/10.1051/0004-6361/202140544)
- Nilson, P. 1973, Uppsala general catalogue of galaxies
- Nucita, A. A., De Paolis, F., Saxton, R., et al. 2017, *ApJ*, 850, 111, doi: [10.3847/1538-4357/aa9481](https://doi.org/10.3847/1538-4357/aa9481)
- Ogle, P. M., López, I. E., Reynaldi, V., et al. 2024, *ApJ*, 962, 196, doi: [10.3847/1538-4357/ad1242](https://doi.org/10.3847/1538-4357/ad1242)
- O’Sullivan, E., Appleton, P. N., Joshi, B. A., et al. 2025, *ApJ*, 979, 240, doi: [10.3847/1538-4357/ada14b](https://doi.org/10.3847/1538-4357/ada14b)
- O’Sullivan, E., Giacintucci, S., David, L. P., et al. 2011, *ApJ*, 735, 11, doi: [10.1088/0004-637X/735/1/11](https://doi.org/10.1088/0004-637X/735/1/11)
- O’Sullivan, E., Ponman, T. J., Kolokythas, K., et al. 2017, *MNRAS*, 472, 1482, doi: [10.1093/mnras/stx2078](https://doi.org/10.1093/mnras/stx2078)
- O’Sullivan, E., Combes, F., Salomé, P., et al. 2018, *A&A*, 618, A126, doi: [10.1051/0004-6361/201833580](https://doi.org/10.1051/0004-6361/201833580)
- Pai, A., Blanton, M. R., & Moustakas, J. 2024, *ApJ*, 977, 102, doi: [10.3847/1538-4357/ad89b8](https://doi.org/10.3847/1538-4357/ad89b8)
- Pasini, T., Brüggén, M., de Gasperin, F., et al. 2020, *MNRAS*, 497, 2163, doi: [10.1093/mnras/staa2049](https://doi.org/10.1093/mnras/staa2049)
- Peralta de Arriba, L., Alonso-Herrero, A., García-Burillo, S., et al. 2023, *A&A*, 675, A58, doi: [10.1051/0004-6361/202245408](https://doi.org/10.1051/0004-6361/202245408)
- Peterson, B. W., Appleton, P. N., Helou, G., et al. 2012, *ApJ*, 751, 11, doi: [10.1088/0004-637X/751/1/11](https://doi.org/10.1088/0004-637X/751/1/11)
- Petric, A. O., Armus, L., Flagey, N., et al. 2018, *AJ*, 156, 295, doi: [10.3847/1538-3881/aaca35](https://doi.org/10.3847/1538-3881/aaca35)
- Piconcelli, E., Cappi, M., Bassani, L., Di Cocco, G., & Dadina, M. 2003, *A&A*, 412, 689, doi: [10.1051/0004-6361:20031490](https://doi.org/10.1051/0004-6361:20031490)
- Pietsch, W., Trinchieri, G., Arp, H., & Sulentic, J. W. 1997, *A&A*, 322, 89
- Pinto, C., Alston, W., Soria, R., et al. 2017, *MNRAS*, 468, 2865, doi: [10.1093/mnras/stx641](https://doi.org/10.1093/mnras/stx641)
- Pinto, C., Soria, R., Walton, D. J., et al. 2021, *MNRAS*, 505, 5058, doi: [10.1093/mnras/stab1648](https://doi.org/10.1093/mnras/stab1648)
- Plauchu-Frayn, I., Del Olmo, A., Coziol, R., & Torres-Papaqui, J. P. 2012, *A&A*, 546, A48, doi: [10.1051/0004-6361/201219916](https://doi.org/10.1051/0004-6361/201219916)
- Plucinsky, P. P., Bogdan, A., & Marshall, H. L. 2022, in *Society of Photo-Optical Instrumentation Engineers (SPIE) Conference Series*, Vol. 12181, *Space Telescopes and Instrumentation 2022: Ultraviolet to Gamma Ray*, ed. J.-W. A. den Herder, S. Nikzad, & K. Nakazawa, 121816X, doi: [10.1117/12.2630193](https://doi.org/10.1117/12.2630193)
- Ponman, T. J., Allan, D. J., Jones, L. R., et al. 1994, *Nature*, 369, 462, doi: [10.1038/369462a0](https://doi.org/10.1038/369462a0)
- Poutanen, J., Lipunova, G., Fabrika, S., Butkevich, A. G., & Abolmasov, P. 2007, *MNRAS*, 377, 1187, doi: [10.1111/j.1365-2966.2007.11668.x](https://doi.org/10.1111/j.1365-2966.2007.11668.x)
- Quirola-Vásquez, J., Bauer, F. E., Dwarkadas, V. V., et al. 2019, *MNRAS*, 490, 4536, doi: [10.1093/mnras/stz2858](https://doi.org/10.1093/mnras/stz2858)
- Rafferty, D. A., Birzan, L., Nulsen, P. E. J., et al. 2013, *MNRAS*, 428, 58, doi: [10.1093/mnras/sts007](https://doi.org/10.1093/mnras/sts007)
- Randall, S. W., Nulsen, P. E. J., Jones, C., et al. 2015, *ApJ*, 805, 112, doi: [10.1088/0004-637X/805/2/112](https://doi.org/10.1088/0004-637X/805/2/112)
- Rees, M. J. 1988, *Nature*, 333, 523, doi: [10.1038/333523a0](https://doi.org/10.1038/333523a0)
- Renaud, F., Appleton, P. N., & Xu, C. K. 2010, *ApJ*, 724, 80, doi: [10.1088/0004-637X/724/1/80](https://doi.org/10.1088/0004-637X/724/1/80)
- Ricci, C., & Trakhtenbrot, B. 2023, *Nature Astronomy*, 7, 1282, doi: [10.1038/s41550-023-02108-4](https://doi.org/10.1038/s41550-023-02108-4)
- Risaliti, G., Elvis, M., & Nicastro, F. 2002, *ApJ*, 571, 234, doi: [10.1086/324146](https://doi.org/10.1086/324146)
- Rivers, E., Baloković, M., Arévalo, P., et al. 2015, *ApJ*, 815, 55, doi: [10.1088/0004-637X/815/1/55](https://doi.org/10.1088/0004-637X/815/1/55)
- Rowan-Robinson, M., Saunders, W., Lawrence, A., & Leech, K. 1991, *MNRAS*, 253, 485, doi: [10.1093/mnras/253.3.485](https://doi.org/10.1093/mnras/253.3.485)
- Sacchi, A., Risaliti, G., & Miniutti, G. 2023, *A&A*, 671, A33, doi: [10.1051/0004-6361/202244983](https://doi.org/10.1051/0004-6361/202244983)
- Saintonge, A., Catinella, B., Cortese, L., et al. 2016, *MNRAS*, 462, 1749, doi: [10.1093/mnras/stw1715](https://doi.org/10.1093/mnras/stw1715)
- Sajina, A., Lacy, M., & Scott, D. 2005, *ApJ*, 621, 256, doi: [10.1086/426536](https://doi.org/10.1086/426536)
- Sakelliou, I., Merrifield, M. R., & McHardy, I. M. 1996, *MNRAS*, 283, 673, doi: [10.1093/mnras/283.2.673](https://doi.org/10.1093/mnras/283.2.673)
- Saunders, W., Sutherland, W. J., Maddox, S. J., et al. 2000, *MNRAS*, 317, 55, doi: [10.1046/j.1365-8711.2000.03528.x](https://doi.org/10.1046/j.1365-8711.2000.03528.x)
- Saxton, R., Komossa, S., Auchettl, K., & Jonker, P. G. 2020, *SSRv*, 216, 85, doi: [10.1007/s11214-020-00708-4](https://doi.org/10.1007/s11214-020-00708-4)
- Sazonov, S., Gilfanov, M., Medvedev, P., et al. 2021, *MNRAS*, 508, 3820, doi: [10.1093/mnras/stab2843](https://doi.org/10.1093/mnras/stab2843)
- Silverstein, E. M., Anderson, M. E., & Bregman, J. N. 2018, *AJ*, 155, 14, doi: [10.3847/1538-3881/aa9d2e](https://doi.org/10.3847/1538-3881/aa9d2e)
- Singh, V., Ishwara-Chandra, C. H., Sievers, J., et al. 2015, *MNRAS*, 454, 1556, doi: [10.1093/mnras/stv2071](https://doi.org/10.1093/mnras/stv2071)
- Smith, B. J. 2000, *ApJ*, 541, 624, doi: [10.1086/309448](https://doi.org/10.1086/309448)
- Smith, B. J., Campbell, K., Struck, C., et al. 2018, *AJ*, 155, 81, doi: [10.3847/1538-3881/aaa1a6](https://doi.org/10.3847/1538-3881/aaa1a6)
- Smith, B. J., Giroux, M. L., & Struck, C. 2022, *AJ*, 164, 146, doi: [10.3847/1538-3881/ac88c5](https://doi.org/10.3847/1538-3881/ac88c5)
- Smith, B. J., Nowak, M., Donahue, M., & Stocke, J. 2003, *AJ*, 126, 1763, doi: [10.1086/378361](https://doi.org/10.1086/378361)
- Smith, B. J., Swartz, D. A., Miller, O., et al. 2012, *AJ*, 143, 144, doi: [10.1088/0004-6256/143/6/144](https://doi.org/10.1088/0004-6256/143/6/144)
- Smith, B. J., Wagstaff, P., Struck, C., et al. 2019, *AJ*, 158, 169, doi: [10.3847/1538-3881/ab3e72](https://doi.org/10.3847/1538-3881/ab3e72)



- Smith, B. J., Watson, M., Giroux, M. L., & Struck, C. 2024, *AJ*, 168, 12, doi: [10.3847/1538-3881/ad46fb](https://doi.org/10.3847/1538-3881/ad46fb)
- Smith, D. A., Herter, T., & Haynes, M. P. 1998, *ApJ*, 494, 150, doi: [10.1086/305175](https://doi.org/10.1086/305175)
- Smith, D. A., Herter, T., Haynes, M. P., Beichman, C. A., & Gautier, T. N., I. 1996, *ApJS*, 104, 217, doi: [10.1086/192299](https://doi.org/10.1086/192299)
- Sohn, J., Geller, M. J., Hwang, H. S., Zahid, H. J., & Lee, M. G. 2016, *ApJS*, 225, 23, doi: [10.3847/0067-0049/225/2/23](https://doi.org/10.3847/0067-0049/225/2/23)
- Sohn, J., Hwang, H. S., Lee, M. G., Lee, G.-H., & Lee, J. C. 2013, *ApJ*, 771, 106, doi: [10.1088/0004-637X/771/2/106](https://doi.org/10.1088/0004-637X/771/2/106)
- Soria, R., Musaeva, A., Wu, K., et al. 2017, *MNRAS*, 469, 886, doi: [10.1093/mnras/stx888](https://doi.org/10.1093/mnras/stx888)
- Stine, P. C. 1992, *ApJS*, 81, 49, doi: [10.1086/191686](https://doi.org/10.1086/191686)
- Stoeckle, J. T., & Burns, J. O. 1987, *ApJ*, 319, 671, doi: [10.1086/165487](https://doi.org/10.1086/165487)
- Strickland, D. K., Heckman, T. M., Colbert, E. J. M., Hoopes, C. G., & Weaver, K. A. 2004, *ApJS*, 151, 193, doi: [10.1086/382214](https://doi.org/10.1086/382214)
- Sulentic, J. W., Rosado, M., Dultzin-Hacyan, D., et al. 2001, *AJ*, 122, 2993, doi: [10.1086/324455](https://doi.org/10.1086/324455)
- Swartz, D. A., Ghosh, K. K., Tennant, A. F., & Wu, K. 2004, *ApJS*, 154, 519, doi: [10.1086/422842](https://doi.org/10.1086/422842)
- Swartz, D. A., Soria, R., Tennant, A. F., & Yukita, M. 2011, *ApJ*, 741, 49, doi: [10.1088/0004-637X/741/1/49](https://doi.org/10.1088/0004-637X/741/1/49)
- Tadhunter, C. 2016, *A&A Rv*, 24, 10, doi: [10.1007/s00159-016-0094-x](https://doi.org/10.1007/s00159-016-0094-x)
- Terashima, Y., Kamizasa, N., Awaki, H., Kubota, A., & Ueda, Y. 2012, *ApJ*, 752, 154, doi: [10.1088/0004-637X/752/2/154](https://doi.org/10.1088/0004-637X/752/2/154)
- Torres-Flores, S., Amram, P., Mendes de Oliveira, C., et al. 2014, *MNRAS*, 442, 2188, doi: [10.1093/mnras/stu1002](https://doi.org/10.1093/mnras/stu1002)
- Tozzi, P., Gilli, R., Mainieri, V., et al. 2006, *A&A*, 451, 457, doi: [10.1051/0004-6361:20042592](https://doi.org/10.1051/0004-6361:20042592)
- Trinchieri, G., Sulentic, J., Breitschwerdt, D., & Pietsch, W. 2003, *A&A*, 401, 173, doi: [10.1051/0004-6361:20030108](https://doi.org/10.1051/0004-6361:20030108)
- Trussler, J., Maiolino, R., Maraston, C., et al. 2020, *MNRAS*, 491, 5406, doi: [10.1093/mnras/stz3286](https://doi.org/10.1093/mnras/stz3286)
- Tzanavaris, P., Hornschemeier, A. E., Gallagher, S. C., et al. 2016, *ApJ*, 817, 95, doi: [10.3847/0004-637X/817/2/95](https://doi.org/10.3847/0004-637X/817/2/95)
- . 2010, *ApJ*, 716, 556, doi: [10.1088/0004-637X/716/1/556](https://doi.org/10.1088/0004-637X/716/1/556)
- Tzanavaris, P., Gallagher, S. C., Hornschemeier, A. E., et al. 2014, *ApJS*, 212, 9, doi: [10.1088/0067-0049/212/1/9](https://doi.org/10.1088/0067-0049/212/1/9)
- van Breugel, W. J. M., Heckman, T. M., Miley, G. K., & Filippenko, A. V. 1986, *ApJ*, 311, 58, doi: [10.1086/164754](https://doi.org/10.1086/164754)
- Venturi, G., Cresci, G., Marconi, A., et al. 2021, *A&A*, 648, A17, doi: [10.1051/0004-6361/202039869](https://doi.org/10.1051/0004-6361/202039869)
- Verdes-Montenegro, L., Yun, M. S., Williams, B. A., et al. 2001, *A&A*, 377, 812, doi: [10.1051/0004-6361:20011127](https://doi.org/10.1051/0004-6361:20011127)
- Vollmer, B., Braine, J., Mazzilli-Ciraulo, B., & Schneider, B. 2021, *A&A*, 647, A138, doi: [10.1051/0004-6361/202037887](https://doi.org/10.1051/0004-6361/202037887)
- Walker, L. M., Johnson, K. E., Gallagher, S. C., et al. 2010, *AJ*, 140, 1254, doi: [10.1088/0004-6256/140/5/1254](https://doi.org/10.1088/0004-6256/140/5/1254)
- . 2016, *AJ*, 151, 30, doi: [10.3847/0004-6256/151/2/30](https://doi.org/10.3847/0004-6256/151/2/30)
- Walton, D. J., Mackenzie, A. D. A., Gully, H., et al. 2022, *MNRAS*, 509, 1587, doi: [10.1093/mnras/stab3001](https://doi.org/10.1093/mnras/stab3001)
- Watkins, A. E., Salo, H., Laurikainen, E., et al. 2022, *A&A*, 660, A69, doi: [10.1051/0004-6361/202142627](https://doi.org/10.1051/0004-6361/202142627)
- Weinberger, R., Springel, V., Pakmor, R., et al. 2018, *MNRAS*, 479, 4056, doi: [10.1093/mnras/sty1733](https://doi.org/10.1093/mnras/sty1733)
- Werner, N., McNamara, B. R., Churazov, E., & Scannapieco, E. 2019, *SSRv*, 215, 5, doi: [10.1007/s11214-018-0571-9](https://doi.org/10.1007/s11214-018-0571-9)
- Willett, K. W., Lintott, C. J., Bamford, S. P., et al. 2013, *MNRAS*, 435, 2835, doi: [10.1093/mnras/stt1458](https://doi.org/10.1093/mnras/stt1458)
- Wilms, J., Allen, A., & McCray, R. 2000, *ApJ*, 542, 914, doi: [10.1086/317016](https://doi.org/10.1086/317016)
- Wilson, A. S., & Colbert, E. J. M. 1995, *ApJ*, 438, 62, doi: [10.1086/175054](https://doi.org/10.1086/175054)
- Wilson, A. S., & Ulvestad, J. S. 1983, *ApJ*, 275, 8, doi: [10.1086/161507](https://doi.org/10.1086/161507)
- Wolter, A., & Trinchieri, G. 2004, *A&A*, 426, 787, doi: [10.1051/0004-6361:20047110](https://doi.org/10.1051/0004-6361:20047110)
- Wu, H., Cao, C., Hao, C.-N., et al. 2005, *ApJL*, 632, L79, doi: [10.1086/497961](https://doi.org/10.1086/497961)
- Wu, H., Zhu, Y.-N., Cao, C., & Qin, B. 2007, *ApJ*, 668, 87, doi: [10.1086/521070](https://doi.org/10.1086/521070)
- Wu, Y., Charmandaris, V., Hao, L., et al. 2006, *ApJ*, 639, 157, doi: [10.1086/499226](https://doi.org/10.1086/499226)
- Yeager, T., Struck, C., & Appleton, P. 2024, arXiv e-prints, arXiv:2409.11707, doi: [10.48550/arXiv.2409.11707](https://doi.org/10.48550/arXiv.2409.11707)
- Yeager, T. R., & Struck, C. 2020, *MNRAS*, 492, 4892, doi: [10.1093/mnras/staa121](https://doi.org/10.1093/mnras/staa121)
- Zaragoza-Cardiel, J., Gómez-González, V. M. A., Mayya, D., & Ramos-Larios, G. 2022, *MNRAS*, 514, 1689, doi: [10.1093/mnras/stac1423](https://doi.org/10.1093/mnras/stac1423)
- Zhu, Y.-N., Wu, H., Cao, C., & Li, H.-N. 2008, *ApJ*, 686, 155, doi: [10.1086/591121](https://doi.org/10.1086/591121)